Light Scattering of Complex Particles: Application to the Time-Shift Technique

Li, Lingxi

(2020)

Light Scattering of Complex Particles: Application to the Time-Shift Technique

Am Fachbereich Maschinenbau
der Technischen Universität Darmstadt
zur
Erlangung des Grades eines Doktor-Ingenieurs (Dr.-Ing.)
genehmigte

Dissertation

vorgelegt von

Lingxi Li, M.Sc.

aus Yan'an, China

Berichterstatter:	Prof. Dr.-Ing. C. Tropea
1. Mitberichterstatter:	Prof. Dr. Xiaoshu. Cai
Tag der Einreichung:	11.08.2020
Tag der mündlichen Prüfung:	07.10.2020

Darmstadt 2020

D 17

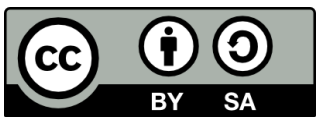

Abstract

Particles with complex shapes and compositions are omnipresent in industrial processes, such as encountered in the chemical, pharmaceutical, automobile and food industries. For instance colloidal drop, i.e. drop with solid particles dispersed in them, are inherent in the spray drying process used frequently in the food industry. Thus, in order to optimize such processes, there is a need to characterize these particles in terms of size, colloidal (solid particle) concentration, the size of the inclusions and possibly also velocity. The present study addresses this need for drop characterisation and concentrates on some particular examples of complex particles: drops with single embedded spheres; drops with single embedded platelets (e.g. aluminum flakes); and drops with multiple micro- or nanoparticle inclusions (colloidal suspension drops). The characterization of a homogeneous spheroidal particle has also been studied, serving as a validation and reference case.

This thesis focuses on the light scattering of complex particles and characterization of such particles with the time-shift measurement technique. Within the scope of this study, spheroidal drops, drops with single embedded flakes or spheres, and drops with multiple spherical inclusions have been studied. According to the shape, composition and the size parameter of the particle, corresponding simulation methods have been chosen to simulate the light scattering. The ray-tracing method has been used to investigate the light scattering properties of spheroidal drop by varying its aspect ratio, and drops with single embedded flakes or spheres by varying the position of the sphere and the orientation of the flake within the drop. For drops with multiple inclusions, the polarized Monte Carlo ray-tracing method as well as the discrete dipole approximation method are used to study its light scattering properties. In addition, the time-shift signals, which are generated when the particle falls through a highly focused Gaussian beam of the time-shift instrument, have been simulated for the drops mentioned before. The goal is to investigate if the time-shift technique is able to unequivocally detect whether a drop contains a spherical particle or not, or detect if the drop contains flake. The possibility to use the time-shift technique to estimate the volume concentration of the inclusions within the drop has been studied as well.

To validate the simulation results, corresponding experiments have been conducted to obtain the raw time-shift signals by using the time-shift instrument to measure pure water drops as well as the colloidal drops, which have multiple polystyrene latex nanoparticles embedded. During the measurement, the size and the volume concentration of the nanoparticles have been varied. Subsequently, comparison has been made between the measured and simulated time-shift signals to validate the simulation results. Through signal processing, the relative scattering strength from the inclusions has been evaluated from the measured time-shift signal to estimate the volume concentration of the inclusions. The size of the inclusions is estimated through evaluation the attenuation ratio of the time-shift signal.

Kurzfassung

Partikel mit komplexen Formen und Zusammensetzungen sind in industriellen Prozessen allgegenwärtig. Sie finden in der chemischen, pharmazeutischen, Automobil- und Lebensmittelindustrie Anwedungen. Beispielsweise sind kolloidale Tröpfchen, d. H. Tröpfchen mit darin dispergierten festen Partikeln, häufig in Sprühtrocknungsprozess in der Lebensmittelindustrie von Relevanz. Um die zugehörigen technischen Prozesse optimieren zu können, besteht die Notwendigkeit, diese Partikel hinsichtlich ihrer Größe, kolloidalen Konzentration (feste Partikel), Größe der Inklusionen und möglicherweise auch ihrer Geschwindigkeit zu charakterisieren. Die vorliegende Arbeit befasst sich mit der Tröpfchencharakterisierung unter den genannten Aspekten und konzentriert sich auf einige besondere Beispiele komplexer Partikel: Tröpfchen mit einzelnen eingebetteten Kugeln; Tröpfchen mit einzelnen eingebetteten Flocken (z. B. Aluminiumflocken) und Tröpfchen mit mehreren Mikro- oder Nanopartikelinklusionen (kolloidale Suspensionströpfchen). Die Charakterisierung eines homogenen ellipsenförmigen Partikels wird ebenfalls untersucht und dient als Validierungs- und Referenzfall.

Genauer befasst sich diese Arbeit mit der Lichtstreuung komplexer Partikel und der Charakterisierung solcher Partikel mit der Zeitverschiebungsmesstechnik. Hierbei werden kugelförmige Tröpfchen, Tröpfchen mit einzelnen eingebetteten Flocken oder Kugeln und Tröpfchen mit mehreren kugelförmigen Inklusionen betrachtet. Entsprechend der Form, Zusammensetzung und geometrischen Eigenschaften des Partikels werden entsprechende Simulationsmethoden ausgewählt, um die Lichtstreuung der Partikel zu simulieren. Das Raytracing-Verfahren wird verwendet um die Lichtstreuungseigenschaften von kugelförmigen Tröpfchen für unterschiedliche Seitenverhältnisses zu untersuchen. Bei Tröpfchen mit einzelnen eingebetteten Flocken oder Kugeln wird mittels des Verfahrens der Einfluss der Position der Kugel innerhalb des Tröpfchens und der Ausrichtung von Flocken innerhalb des Tröpfchens untersucht. Für Tröpfchen mit mehreren Inklusionen werden das polarisierte Monte-Carlo-Raytracing-Verfahren sowie die diskrete Dipole Approximation verwendet, um ihre Lichtstreuungseigenschaften zu untersuchen. Zudem werden die Zeitverschiebungssignale simuliert, welche entstehen, wenn Tröpfchen mit den zuvor genannten Eigenschaften durch einen stark fokussierten Gaußschen Strahl eines Zeitverschiebungsmessinstruments fallen. Ziel ist es zu untersuchen, ob die Zeitverschiebungsmesstechnik eindeutig erkennen kann, ob ein Tröpfchen ein kugelförmiges Teilchen oder Flocken enthält. Die Möglichkeit, die Volumenkonzentration der Inklusionen innerhalb des Tröpfchens mit der Zeitverschiebungstechnik abzuschätzen, wird ebenfalls untersucht.

Zur Validation der Simulationsergebnisse werden entsprechende Experimente durchgeführt. Hierbei werden Zeitverschiebungssignale eines reinen Wassertropfens sowie für kolloidalen Tröpfchen, in die mehrere Polystyrol-Latex-Nanopartikel eingebettet sind, unter Verwendung des Zeitverschiebungsinstruments ermitttelt. Für die Messungen werden die Größe und die Volumenkonzentration der Nanopartikel variiert. Die experimentell ermittelten Zeitverschiebungssignale werden mit denen aus Simulationen verglichen, um die Simulationsergebnisse zu validieren. Durch Signalverarbeitung wird hierbei die relative Streustärke durch Inklusionen aus dem gemessenen Zeitverschiebungssignalen bewertet, um die Volumenkonzentration der Inklusionen abzuschätzen. Die Größe der Inklusionen wird durch Auswertung des Dämpfungsverhältnisses des Zeitverschiebungssignals geschätzt.

Acknowledgement

First of all I would like to express my sincere gratitude to Prof. Dr.-Ing. Cameron Tropea for the opportunity to pursue my research at the Institute for Fluid Dynamics and Aerodynamics (SLA) at the TU Darmstadt and for his support during preparation of this thesis. His scientific intuition, encouragement, and dedicated guidance has contributed immensely to the outcome of my research. Gratitude is also owed to Prof. Dr. Xiaoshu Cai for refereeing my thesis. Working in research was my desire since my undergraduate studies, which is why a few sentences cannot acknowledge the gratitude I feel for the support I received over the last three years.

I would like to thank Prof. Dr.-Ing. Jeanette Hussong for supporting me with respect to my last experiment in Griesheim and the prospective scientific stay in Rouen.

The financial support from the Federal Ministry for Economic Affairs and Energy in Germany through the ZIM Project with contract ZF4415101LT7 and from the German Research Foundation through SFB-TRR 75 is grateful acknowledged. Their support gave me the opportunity to conduct my research and exchange with many inspiring people from all over the world. Stephanie Lath, Monika Medina-Espana and Birgit Neuthe supported me and my project administratively, which I really appreciate.

Deep gratitude is owed to Prof. Dr. rer. nat. Haitao Yu and Dr.-Ing. Patrick Stegmann for scientific guidance during the initial phase of my work, which allowed for an advanced scientific access to the topic and avoided detours. Many fruitful discussions and very useful suggestions regarding future work contributed significantly to the outcome of my project. Dr.-Ing. Patrick Stegmann improved this thesis with many essential remarks during proof-reading. I am also very grateful for the fruitful discussions with Prof. Dr. Feng Xu during the conferences in College Station and Hangzhou.

I would like to address special thanks to Dr.-Ing. Klaus Hufnagel and Dr.-Ing. Klaus Schiffmann for giving me the opportunity to write my Master thesis at SLA. Their guidance and the support from Alexander Beck allowed for a convincing Master thesis and the opportunity to continue with research at SLA.

Dr. rer. nat. Walter Schäfer and Dr.-Ing. Simon Rosenkranz contributed to this thesis with very fruitful discussions and support with respect to experimental aspects. Their rich experimental experience and constructive suggestions helped a lot. Furthermore, I would also like to thank my bachelor student Chuanchao Xu for his excellent numerical simulation.

Special thanks is owed to Prof. Dr. Wu Zhou, Guangwei Xiang, Can Li and Jiangsheng Wang. During their stay in Darmstadt we had wonderful weekend activities, which gave me a lot of energy. Especially with Can Li, we have also very fruitful discussion for the experiment. The pleasant working atmosphere in Griesheim has contributed a lot to my research. The colleagues in Griesheim were always ready to help, which is why I would like to address special thanks to Dr.-Ing. Andreas Bauer, Johannes Kissing, Dr.-Ing. Patrick Seiler, Dr. Amandine Guissart, Niklas Apell, Benedikt Schmidt, Kilian Köbschall, Max Luh, Philipp Brockmann, Dr.-Ing. Johannes Feldmann, Dr.-Ing. Jan Breitenbach, Marija Gajevic Joksimovic and Dr.-Ing. Bernhard Simon. I also appreciate the support from Ilona Kaufhold and her team in the workshop for experimental realizations.

Finally, my deepest thanks are owed to my father Jianguo Li and my older brother Shuaishuai Li as well as my grandparents Wenhua Li and Yuqin Wang. Without their encouragement, it would have been impossible for me to overcome the challenges during my study and research abroad. If life is a journey, I am very grateful to have the opportunity to meet and work with all of you.

Thank you,

Lingxi Li

Contents

1 Introduction

This chapter provides first a motivation for the study of light scattering properties of complex particles. Then an overview of the thesis contents is given.

1.1 Complex particles and their industrial relevance

Particles with complex shapes and compositions are omnipresent in industrial processes, such as encountered in the chemical, pharmaceutical and food industries. For instance colloidal drops, i.e. drops with solid particles dispersed in them, are inherent in the spray drying process used frequently in the food industry. Thus, in order to optimize such processes, there is a need to characterize these particles in terms of size, colloidal (solid particle) concentration and possibly also velocity.

The present study addresses this need for drop characterisation and concentrates on some particular examples of complex particles: drops with single embedded spheres; drops with single embedded platelets (e.g. aluminum flakes); and drops with multiple micro- or nanoparticle inclusions (colloidal suspension drops). The characterization of a homogeneous spheroidal particle has also been studied, serving as a validation and reference case. These different types of complex drops are briefly introduced below, outlining their peculiarities and where they can typically be found in industrial applications.

Microparticles with a core-shell structure

Particles with a core-shell structure are widespread in the pharmaceutical industry. These particles are usually produced using a micro-encapsulation process, by which a drug core is embedded within a liquid shell, as pictured in Fig. 1.1 [34]. Coaxial electrohydrodynamic atomization is one of the micro-encapsulation methods which has been used to produce particles with a core-shell structure, as Fig. 1.2 illustrates. For this method, a coaxial nozzle is used to mix the drug with the shell liquid. During the production process, there is a need to determine whether or not the generated drop contains the drug particle.

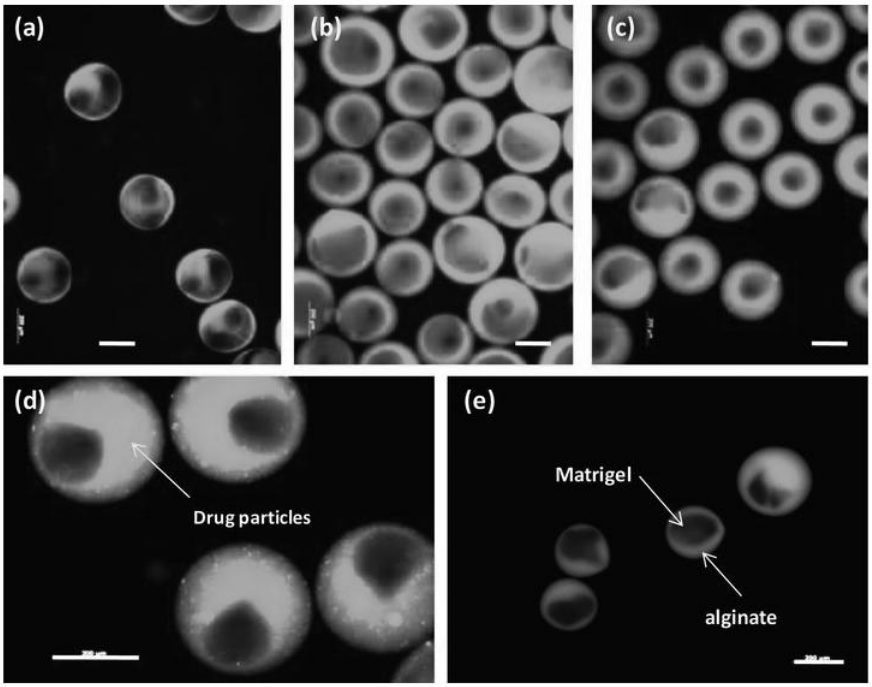

Figure 1.1: Particles with a core-shell structure, produced by the micro-encapsulation method. The material of the shell is alginate and the material of the core is matrigel. The particles within the sub-Figs. (a) - (e) are created by varying the flow speed of the inner phase and outer phase of the coaxial nozzle. The scale bars in all images are 200 microns. Permission granted from the publisher John Wiley & Sons, Inc.

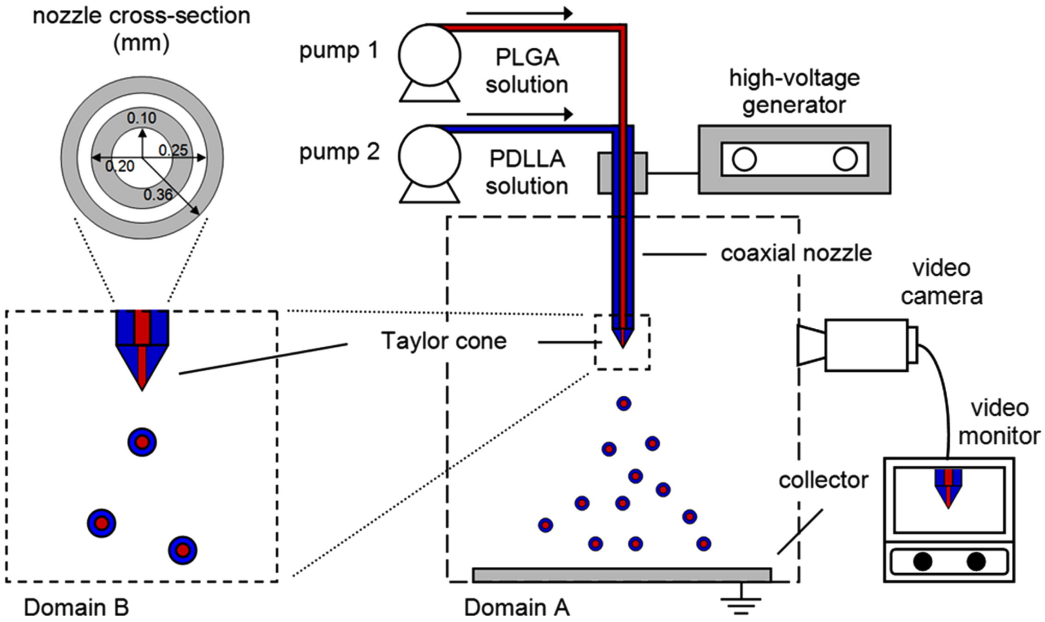

Figure 1.2: CEHDA process for producing uniform composite core–shell structured microspheres [65]. Permission granted from the publisher Elsevier Ltd.

Drop with embedded flakes

Spray painting is a commonly used industrial process to create a radiant surface and to protect the underlying substrate from erosion. For instance, the automotive industry faces sustained challenges to optimize its coating processes in terms of energy and resource minimization and environmental impact. It has been roughly evaluated that the overall transfer efficiency in the automotive industry is only between 50% and 60% [43]. Considering the huge production volume of automobiles, even minor improvements of the paint material usage could lead to a significant economic benefit and a reduction of pollutant discharge.

Figure 1.3: Spray coating in the automotive industry.

Many coatings in the automobile industry involve metallic paints, in which aluminum flakes are embedded in the drops impacting the surface. During the spray coating process, knowing whether the drops contain an aluminum flake or not is therefore of great importance, since it directly affects the quality and lustre of the coating. Moreover, knowing the portion of drops containing flakes could help reduce the overall volume of required paint. Presently, on the commercial market, there are several optical measurement techniques available to measure the distribution of the drop size, such as the time-shift measurement technique [51] and the phase Doppler measurement technique [1]. However, these techniques do not currently offer the possibility of flake detection in a drop. Nevertheless, the time-shift technique is a potential method to capture such information, and this is one ansatz explored in the present study [28], in particular in Chapter 4.

Colloidal suspension drops

Colloidal suspension drops are widely encountered in industrial processes for transporting powders drug as suspensions in liquid before spraying them, for instance fuels with dispersed, metallic nanoparticles, colloidal suspension drops(e.g. ink-jet printing), or encapsulation of particles, in which a liquid layer covers the particle, typical for pharmaceutical applications. A spray drying process for the production of the composite powders is illustrated in figure 1.4 [71]. It is of interest to characterize such drops not only according to the drop size, but also using the colloidal concentration. For instance, in spray drying of milk powder, the solubility of the final dried milk powder is associated with the initial concentration of the milk powder in the colloidal drop, thus, for controlling the solubility, it is necessary to measure the colloidal concentration of the milk drop. Or, as another

example, when cooling hot forge dies by using spray cooling, the drops used for spray cooling usually contain graphite for lubrication purpose, whereby the concentration of the graphite in each drop should be uniform [49].

Figure 1.4: Spray drying process used to produce composite powders. Copyright Reproduced with permission from the publisher Elsevier Ltd.

There exists also need to characterize the size of the inclusions or nanoparticle, as Fig. 1.5 shows. The size of inclusions could range from several tens of nanometer to several hundred micrometer. When the size of the particle under 100nm, it could be difficult to characterize its size with normal scanning electron microscope. With this study, a method is developed for characterization the size of nanoparticle with the time-shift measurement instrument, which will be described in section 5.3.1

Figure 1.5: Silicon nanoparticle powder

In summary, particles with complex shapes and compositions commonly appear in a multitude of industrial applications. Characterization of these particles is of great interest to improve the respective production processes; however, this characterization still remains a challenge. On the other hand, optical measurement techniques are the preferred choice for this task because of their non-intrusiveness [58]. A prerequisite for their development and application is however, understanding and predicting the light scattering properties of such particles.

1.2 Overview of the thesis

This thesis focuses on the light scattering of complex particles and characterization of such particles with the time-shift measurement technique. Within the scope of this study, spheroidal drops, drops with single embedded flakes or spheres, and particles with multiple spherical inclusions have been studied.

Chapter 2 provides a review of classical electromagnetic theory. According to the size, shape and composition of the matter, the corresponding theory for simulation of the light scattering of the matter is introduced, such as the Lorenz-Mie theory for the computation of the light scattering of spherical and homogeneous particles; the extended boundary method for simulation of light scattering from particles with arbitrary symmetry; the ray-tracing method for simulation of large particles with smooth surfaces; and the discrete dipole approximation method for the simulation of light scattering from particles with complex shape and composition.

Chapter 3 is about the simulation of the light scattering from complex particles. For simulation of the light scattering from drops with an embedded particle, the three-dimensional ray-tracing method was used in this study. For colloidal drops with a large size parameter, the polarized three-dimensional, Monte-Carlo ray-tracing method has been used for the simulation of the light scattering; and for colloidal drops with a small size parameter, the discrete dipole approximation method has been used. The simulation results have been validated by comparing to some reference cases with known solutions.

Chapter 4 is about the simulated time-shift signals generated from complex particles. An analytical solution of the time-shift signal generated from a pure drop is given at the beginning. Subsequently, the time-shift signals have been simulated for spheroidal drops by varying the aspect ratio, and drops with an embedded sphere or flake, in order to obtain the signal features to characterize these particles.

Chapters 5 introduces the experimental facilities and the experiments conducted for the validation of the simulation results. The signal from a time-shift device has been recorded when a colloidal suspension drop falls through the laser sheet of the time-shift measurement instrument. The obtained signals were analyzed and compared with the simulation results for the validation of the simulation method.

2 Simulation methods for the light scattering by particle

In this chapter, the author will briefly review some methods for the computation of light scattering from particles. Light is electromagnetic radiation whose wavelength ranges from 380nm to 740nm, therefore, the analytical and numerical formulation for describing the electromagnetic scattering properties of particles is built upon classical electromagnetic theory. The author will start from Maxwell's equations, a set of coupled partial differential equations that forms the foundation of classical electromagnetism. The light scattering problems of particles essentially focus on calculating the electric field within and outside of the particle. Several methods for the simulation of light scattering of particles will be introduced by solving Maxwell's equations under certain boundary conditions dictated by the features of the particle.

2.1 Review of electromagnetic theory

2.1.1 Maxwell's equations

„War es ein Gott, der diese Zeichen schrieb?"

— Ludwig Boltzmann

As the physicist Feynman said, the formulation of Maxwell's equations is one of the most significant events during the 19th century. Before the formulation of the Maxwell's equation, the French mathematician and physicist François Arago, discovered in 1823 that a magnetic field could be induced by an electric current. Subsequently, the British physicist Michael Faraday discovered that an electric field could be created by changing the magnetic flux of a closed loop and that the magnitude of the electric field is proportional to the rate of change of the magnetic flux. Then the Scottish physicist James Clerk Maxwell used a set of differential equations to describe Faraday's work, achieving the second unification in physics. It mathematically interprets how electric charges and currents create the electric and magnetic field as well as how the electric field induces the magnetic field, and vice versa. Maxwell's equations can be formulated either in differential or integral form, as summarized in the following Tab. 2.1.

	Differential Form	Integral Form
Gauss' law	$\nabla \cdot \mathbf{D} = \rho$	$\oint_S \mathbf{D} \cdot d\mathbf{A} = \oint_V \rho \, dV$
Gauss' law for magnetism	$\nabla \cdot \mathbf{B} = 0$	$\oint_S \mathbf{B} \cdot d\mathbf{A} = 0$
Faraday's law of induction	$\nabla \times \mathbf{E} = -\frac{\partial \mathbf{B}}{\partial t}$	$\oint_C \mathbf{E} \cdot d\mathbf{l} - \oint_C \mathbf{B} \times \mathbf{v}_l \cdot d\mathbf{l} = -\frac{d}{dt} \oint_S \mathbf{B} \cdot d\mathbf{A}$
Ampère's law	$\nabla \times \mathbf{H} = \mathbf{J} + \frac{\partial \mathbf{D}}{\partial t}$	$\oint_C \mathbf{H} \cdot d\mathbf{l} = \oint_S \mathbf{J} \cdot d\mathbf{A} + \oint_S \frac{\partial \mathbf{D}}{\partial t} \cdot d\mathbf{A}$

Table 2.1: Maxwell's equations in differential and integral form.

In this table $\mathbf{E}$ is the electric field, $\mathbf{H}$ is the magnetic field, $\mathbf{D}$ is the electric displacement, $\mathbf{B}$ is the magnetic induction, $\mathbf{v}_l$ is the velocity of a part of the boundary loop, $\mathbf{J}$ is the current density and ρ represents the macroscopic free charge density without counting the induced dipole charges bounded by the matter [38]. The Gauss law for the electric displacement formulates how a certain amount of free charge within a space volume results in the electric field. It also states briefly that electric lines diverge away from a positive electric charges and converge towards a negative charge. For the magnetic field, the divergence is zero everywhere; therefore, no magnetic monopole exists. The third equation is a formulation for Faraday's law of induction, which indicates that the time varying magnetic field can induce the electric field. The fourth equation is a generalization of the Ampère's law, which indicates that an electric current induces a magnetic field that swirls around its direction and that a time varying electric field could also contribute to the magnetic field. When the properties of the matter do not change continuously, the boundary conditions depicted as Eqs. (2.1) and (2.2) need to be invoked.

$$\mathbf{n} \times (\mathbf{E}_1 - \mathbf{E}_2) = 0 \tag{2.1}$$

$$\mathbf{n} \cdot (\mathbf{B}_1 - \mathbf{B}_2) = 0 \tag{2.2}$$

in which $\mathbf{n}$ is the normal vector at the boundary. Eqs. (2.1) and (2.2) indicate that the tangential component of $\mathbf{B}$ and the normal component of $\mathbf{E}$ should be continuous.

2.2 Methods for simulation of light scattering from particles

Following Tropea [58], particles can be classified according to their shape and composition, as depicted in Fig. 2.1.

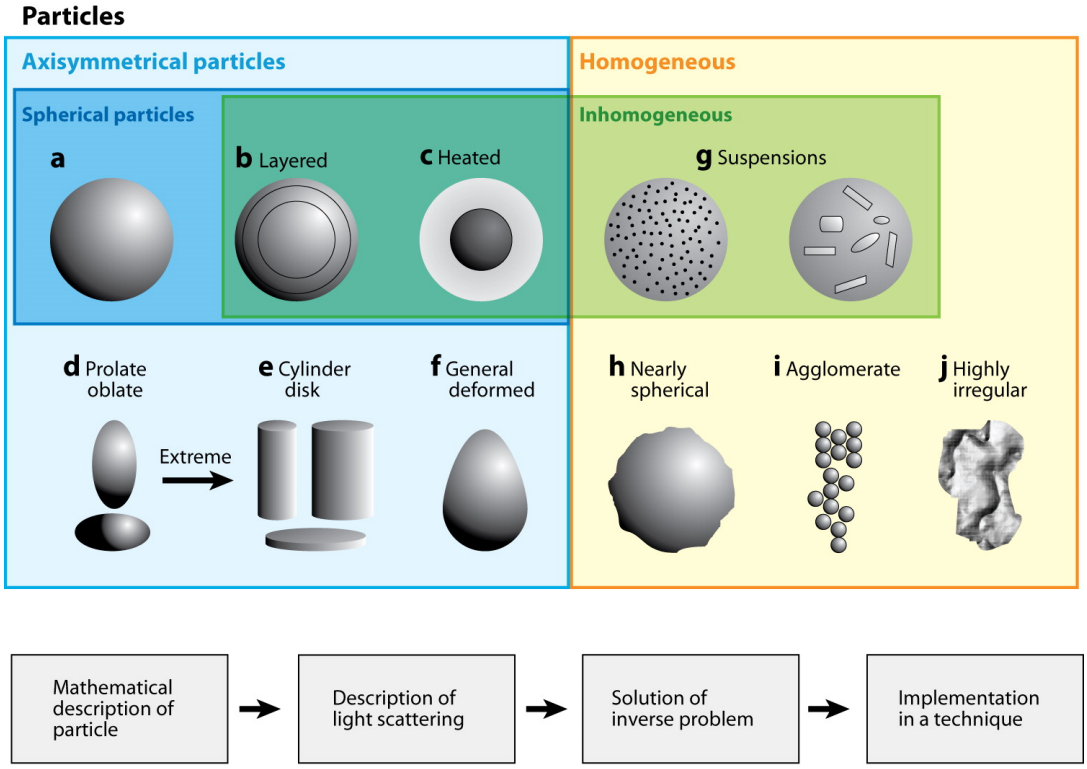

Figure 2.1: Particle classification. Permission granted from the publisher Annual Reviews [58]

To simulate the light scattering of particles, the most appropriate method depends on their shape, size parameter and the composition of the particle. The size parameter is defined as the particle diameter (d) relative to the wavelength λ of the incident light

$$x = \frac{\pi d}{\lambda} \tag{2.3}$$

and is often known as the Mie parameter. The Lorenz-Mie theory embodies a rigorous analytic solution for the light scattering of homogeneous spherical particles illuminated by a plane wave [36]. Subsequently, analytic solutions for homogeneous infinitely long cylinders[47], homogeneous spheroids [3] and a multi-layered spherical particle[21] were also obtained. The Debye series decomposition of the light scattering by a spheroid has been studied, which gives more physical insight into the light scattering by a spheroidal particle [60]. For particles with irregular shapes or inhomogeneous composition, the Discrete Dipole Approximation (DDA) method, which is a numerically exact solution of the electromagnetic scattering of matter, can be used to compute the electromagnetic scattering of such particles [73]. However, as the size parameter and the refractive index of the particle increases, the computation time rises dramatically. The extended boundary condition method can be used to solve the light scattering problem for single or compounded particles with arbitrary shapes as well, especially when particles with arbitrary symmetry and only the orientation average is desired. This method is also known as the T-Matrix method [37]. The intersection between the shaped beam and the particles, which is a more common situation for the practical usage, has been addressed in numerous studies [13] [63] [33]. When the particle is homogeneous and with a smooth surface and large size parameter, geometric optics methods can be used [48] [61] [62] [57] [55]. These various methods for the computation of light scattering, many of which are used in the present study, will be briefly introduced in the following subsections.

2.2.1 Lorenz-Mie theory

The German physicist Gustav Mie gave an exact analytical solution for the scattering of a plane wave by a homogeneous sphere. The idea is to solve Maxwell's equations in a spherical coordinate system by using the variable separation method [36]. Details of the solution can be found in [5]; here only a short introduction of the solution is given. The time dependent harmonic electric field **E** satisfies the vector wave function, when it propagates in a linear, isotropic and homogeneous medium, as the following equation prescribes [37].

$$\nabla^2\mathbf{E} + k^2\mathbf{E} = 0 \tag{2.4}$$

where k is the wave number and equal to $\omega\sqrt{\epsilon\mu}$, and ω is the angular frequency of the electric field, ϵ is the permittivity and μ is the magnetic permeability. However, this does not mean that the single component of **E** satisfies the scalar wave function. Solving this vector wave function can be changed into solving a scalar wave function by constructing a vector function $\mathbf{M} = \nabla \times (\mathbf{c}\Psi)$, in which Ψ is a scalar function, **c** is constant vector and **M** is divergence free and satisfies the vector wave function. Using vector identities, the following equation can be obtained.

$$\nabla^2\mathbf{M} + k^2\mathbf{M} = \nabla \times [\mathbf{c}(\nabla^2\Psi + k^2\Psi)] \tag{2.5}$$

Finding the solution **M** for the vector wave function is replaced by finding the solution for the scalar wave function Ψ. An equation for the scalar wave function in spherical coordinates is given as

$$\frac{1}{r^2}\frac{\partial}{\partial r}(r^2\frac{\partial\Psi}{\partial r}) + \frac{1}{r^2\sin\theta}\frac{\partial}{\partial\theta}(\sin\theta\frac{\partial\Psi}{\partial\theta}) + \frac{1}{r^2\sin\theta}\frac{\partial^2\Psi}{\partial\phi^2} + k^2\Psi = 0 \tag{2.6}$$

Using the separation of variables a solution in the following form is postulated.

$$\Psi(r,\theta,\phi) = R(r)Y(\theta,\phi) = R(r)\Theta(\theta)\Phi(\phi) \tag{2.7}$$

Here $Y(\theta,\phi)$ is the solution of the Laplace function of the angular part in a spherical coordinate system, known as spherical harmonics. The spherical harmonic function is a set of orthogonal basic functions defined on the surface of a sphere; therefore, any function defined on the surface of the sphere can be expressed with spherical harmonics. Substituting Eq. (2.7) into Eq. (2.6), the following equations can be obtained

$$\frac{d^2\Phi}{d\phi^2} + m_c^2\phi = 0 \tag{2.8}$$

$$\frac{1}{\sin\theta}\frac{d}{d\theta}(\sin\theta\frac{d\Theta}{d\theta}) + [n_c(n_c+1) - \frac{m_c^2}{\sin^2\theta}]\Theta = 0 \tag{2.9}$$

$$\frac{d}{dr}(r^2\frac{dR}{dr}) + [k^2r^2 - n_c(n_c+1)]R = 0 \tag{2.10}$$

in which the separation constants m_c and n_c can be determined by subsidiary conditions that ψ must satisfy. The Eqs. (2.9) and (2.10) are the Legendre equation and the Bessel differential equation respectively, whose solutions are the associated Legendre functions and the Bessel functions. Then the generating function ψ that satisfies the scalar wave function can be constructed. By using the same procedure, the scalar wave function for the magnetic field **H** can also be constructed.

The incident plane wave is expanded using vector spherical harmonics, as well as the scattered field. The solution is then obtained by invoking the following boundary condition and utilizing the orthogonality of the vector harmonics.

$$\mathbf{n} \times (\mathbf{E}_{incident} + \mathbf{E}_{scattered} - \mathbf{E}_{inside}) = 0 \tag{2.11}$$

$$\mathbf{n} \times (\mathbf{H}_{incident} + \mathbf{H}_{scattered} - \mathbf{H}_{inside}) = 0 \tag{2.12}$$

The general solution of the scattered electric field is given in the form of an infinite series, as the following equations describe.

$$S_1(\alpha, m, \theta) = \sum_{n=1}^{\infty} \frac{2n+1}{n(n+1)} [a_n(\alpha, m)\pi_n(\cos(\theta)) + b_n(\alpha, m)\tau_n(\cos(\theta))] \tag{2.13}$$

$$S_2(\alpha, m, \theta) = \sum_{n=1}^{\infty} \frac{2n+1}{n(n+1)} [a_n(\alpha, m)\tau_n(\cos(\theta)) + b_n(\alpha, m)\pi_n(\cos(\theta))] \tag{2.14}$$

in which a_n and b_n are scattering coefficient; π_n and τ_n are related through Legendre polynomials defined as follows

$$\pi_n = \frac{P_n^1}{\sin(\theta)} \tag{2.15}$$

$$\tau_n = \cos\theta \pi_n(\cos\theta) - (1 - \cos\theta^2) \frac{d\pi_n(\cos\theta)}{d\cos\theta} \tag{2.16}$$

$$a_n = \frac{m\psi_n(mx)\psi_n'(x) - \psi_n(x)\psi_n'(mx)}{m\psi_n(mx)\zeta_n'(x) - \zeta_n(x)\psi_n'(mx)} \tag{2.17}$$

$$b_n = \frac{m\psi_n(x)\psi_n'(mx) - \psi_n(mx)\psi_n'(x)}{m\zeta_n(x)\psi_n'(mx) - \psi_n(mx)\zeta_n'(x)} \tag{2.18}$$

Although with the Lorenz-Mie theory the incident wave is limited to a monochromatic wave with arbitrary polarization, an arbitrary field can be viewed as the superposition of numerous monochromatic fields using a Fourier decomposition [1]. Therefore, for an arbitrary wave that is incident on a homogeneous spherical particle, the solution for its light scattering can be obtained by superimposing the solution from single Fourier components of the arbitrary incident field [5].

2.2.2 Debye series decomposition

Peter Debye solved the Maxwell's equations, for a plane wave incident on a homogeneous infinite long cylinder, which is known as the Debye series decomposition [8]. Debye theory provides further physical insight into the light scattering problem. The scattering coefficients a_n and b_n in the Lorenz-Mie theory can be expressed using the Debye series decomposition [30] [54].

$$a_n = \frac{1}{2}[1 - R_{n,TM}^{212} - \sum_{p=1}^{\infty} \frac{T_{n,TM}^{21} T_{n,TM}^{12}}{1 - R_{n,TM}^{121}}] \tag{2.19}$$

$$b_n = \frac{1}{2}[1 - R_{n,TE}^{212} - \sum_{p=1}^{\infty} \frac{T_{n,TE}^{21} T_{n,TE}^{12}}{1 - R_{n,TE}^{121}}] \tag{2.20}$$

in which R_n^{212} and R_n^{121} are the coefficients for reflection of the partial-wave and T_n^{21}; T_n^{12} are the coefficient for transmission of partial-wave; the subscript TE and TM refer to the transverse electric wave and transverse magnetic wave respectively. These coefficients are formulated with Eqs. (2.21) - (2.24)[30].

$$T_n^{12} = -\frac{2i}{D_n^1} \tag{2.21}$$

$$T_n^{12} = -\frac{m_1}{m_2}\frac{2i}{D_n^1} \tag{2.22}$$

$$R_n^{212} = -\frac{\alpha\xi_n^{(2)'}(m_2ka)\xi_n^{(2)}(m_1ka) - \beta\xi_n^{(2)}(m_2ka)\xi_n^{(2)'}(m_1ka)}{D_n^1} \tag{2.23}$$

$$R_n^{121} = -\frac{\alpha\xi_n^{(1)'}(m_2ka)\xi_n^{(1)}(m_1ka) - \beta\xi_n^{(1)}(m_2ka)\xi_n^{(1)'}(m_1ka)}{D_n^1} \tag{2.24}$$

in which $\xi_n^{(1)}$ and $\xi_n^{(2)}$ are the Riccati-Bessel functions and D_n is given by Eq. (2.25).

$$D_n = -\alpha\xi_n^{(1)'}(m_2ka)\xi_n^{(2)}(m_1ka) + \beta\xi_n^{(1)}(m_2ka)\xi_n^{(2)'}(m_1ka) \tag{2.25}$$

$$\alpha = \begin{cases} 1 & TE\ wave \\ \frac{m_1}{m_2} & TM\ wave \end{cases} \tag{2.26}$$

$$\beta = \begin{cases} \frac{m_1}{m_2} & TE\ wave \\ 1 & TM\ wave \end{cases} \tag{2.27}$$

Eqs. (2.19) and (2.20) can be rewritten as

$$a_n = \frac{1}{2}[1 - R_{n,TM}^{212} - \sum_{p=1}^{\infty} T_{n,TM}^{21} \left(R_{n,TM}^{121}\right)^{p-1} T_{n,TM}^{12}] \tag{2.28}$$

$$b_n = \frac{1}{2}[1 - R_{n,TE}^{212} - \sum_{p=1}^{\infty} T_{n,TE}^{21} \left(R_{n,TE}^{121}\right)^{p-1} T_{n,TE}^{12}] \tag{2.29}$$

in right hand side of Eqs. (2.28) and (2.29), the physical meaning of the three terms are the diffraction around the particle, the outgoing waves reflected from the particle surface and the sum of outgoing waves after $p-1$ internal reflections respectively, as Fig. 2.2 illustrates.

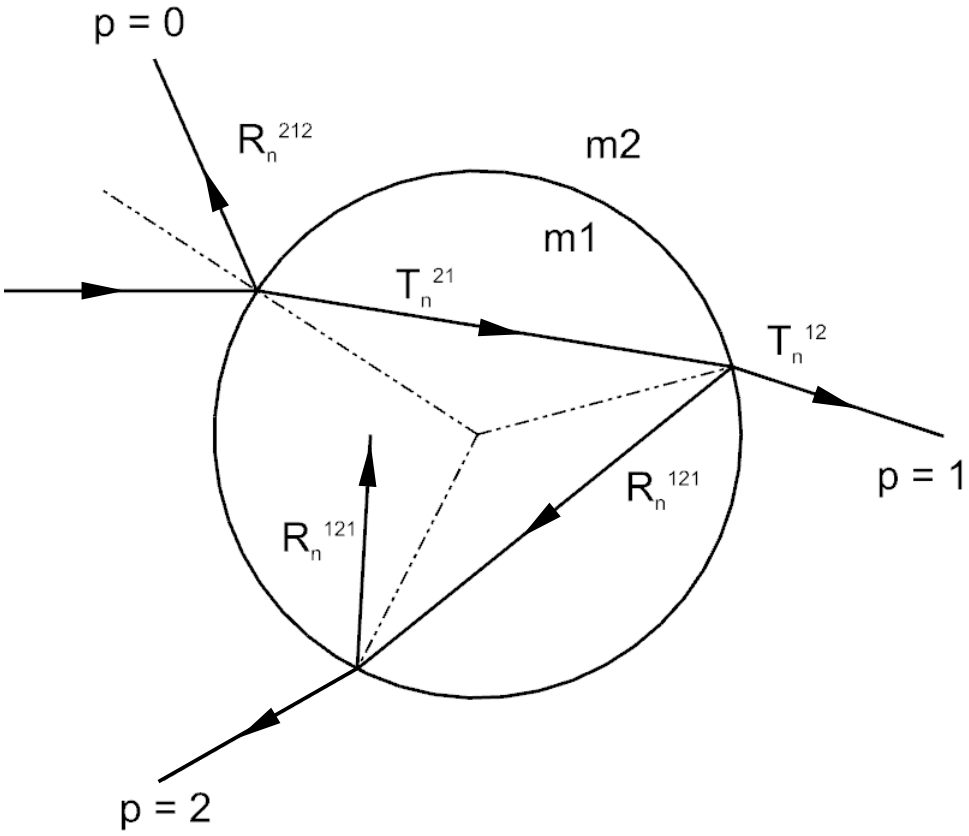

Figure 2.2: Illustration for Debye series decomposition.

2.2.3 Discrete dipole approximation

The Discrete Dipole Approximation method, also known as DDA, is a common method to study electromagnetic scattering and absorption of a particle of arbitrary shape and composition. It was originally developed to study interstellar light scattering by Purcell and Pennypacker [44]. Several DDA codes were developed, such as the DDSCAT by Draine et al. [9], which is written in Fortran and ADDA by Yurkin et al., which is written in C [72]. The basic idea of DDA is based on the physical principle that matter is composed of electrons and protons. When matter is in an electric field, the positive charges and the negative charges become polarized. Then the matter is equivalent to many electric dipoles, polarized in the electric field, as Fig. 2.3 illustrates. Then the total scattered field can be obtained by superposition of the scattered vector field from the individual dipoles.

By introducing a volume current density $\mathbf{J_r}$, the vector Helmholtz Eq. (2.4) can be rewritten as

$$(\nabla \times \nabla \times \mathbf{I} - k^2)\mathbf{E}(\mathbf{r}) = i\omega\mu_0\mathbf{J}(\mathbf{r}) \tag{2.30}$$

$$\mathbf{J}(\mathbf{r}) = \begin{cases} -i\omega\epsilon_0[\epsilon_r(\mathbf{r}) - 1]\mathbf{E}(\mathbf{r}) : \mathbf{r} \in V_{internal} \\ \mathbf{0} \qquad\qquad\qquad\qquad\quad : \mathbf{r} \in V_{external} \end{cases} \tag{2.31}$$

in which $\mathbf{I}$ is the identity dyadic, ϵ_0 is the vacuum permittivity, $\epsilon_r(\mathbf{r})$ is the relative permittivity and $\mathbf{J}(\mathbf{r})$ is the volume current density. This linear inhomogeneous differential equation can be solved by adding the solution of the solution for the homogeneous equation when the right-hand side of

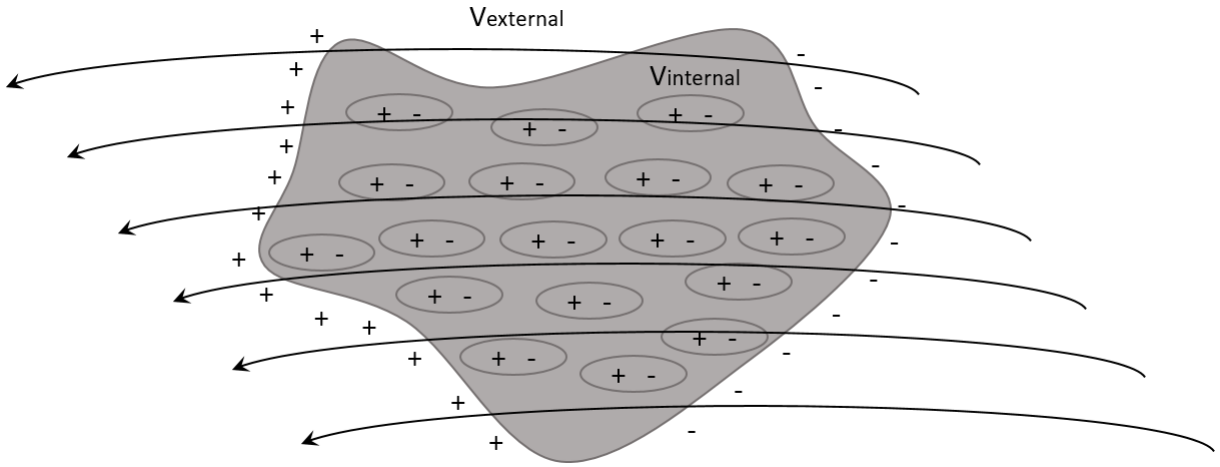

Figure 2.3: Polarization of material by an electric field to create dipoles throughout the matter.

the Eq. (2.30) is **0** and a particular solution of this inhomogeneous equation. The homogeneous equation describes the electric field in free space when matter is absent; and the particular solution of Eq. (2.30) corresponds to the scattered electric field by the matter. A standard technique to find the solution is to use Green's function and the Dirac delta function. Green's function has the following property, which can be expressed by [74]

$$(\nabla \times \nabla \times \mathbf{I} - k^2)\mathbf{G}_0(\mathbf{r}, \mathbf{r}') = \mathbf{I}\delta^3(\mathbf{r} - \mathbf{r}') \tag{2.32}$$

Green's function in Eq. (2.32) can be analytically expressed as

$$\mathbf{G}_0(\mathbf{r}, \mathbf{r}') = [\mathbf{I} + \frac{1}{k_0}\nabla\nabla]\frac{exp(ik_0|\mathbf{r} - \mathbf{r}'|)}{4\pi|\mathbf{r} - \mathbf{r}'|} \tag{2.33}$$

By using Green's function, the solution of Eq. (2.30) can be written as

$$\mathbf{E}(\mathbf{r}) = \mathbf{E}_{incident}(\mathbf{r}) + i\omega\mu_0 \int_{V_{internal}} d^3r' \mathbf{G}_0(\mathbf{r}, \mathbf{r}')\mathbf{J}(\mathbf{r}) \tag{2.34}$$

in which $\mathbf{E}_{incident}(\mathbf{r})$ is the incident electric field. Eq. (2.34) can be evaluated numerically by discretizing the interior region of the matter into N cells, as Fig. 2.4 illustrates.

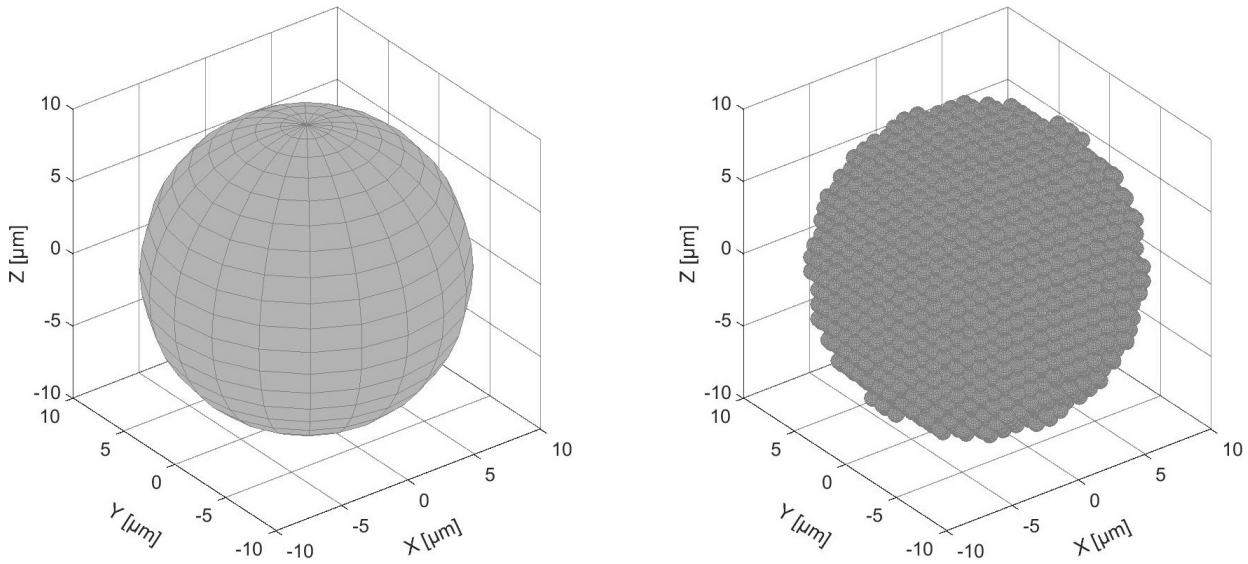

Figure 2.4: Discretisation of a sphere using the DDA method. The left part is a sphere with the diameter of 10 μm; the right part shows the discretisation of the sphere.

The discretisation leads to a reformulation of Eq. (2.34) [23].

$$\mathbf{E}(\mathbf{r}) - i\omega\mu_0 \int_{V_m} d^3r' \mathbf{G}_0(\mathbf{r},\mathbf{r}')\mathbf{J}(\mathbf{r}) = \mathbf{E}_{incident}(\mathbf{r}) + i\omega\mu_0 \sum_{k=1k\neq m}^{N} \int_{V_k} d^3r' \mathbf{G}_0(\mathbf{r},\mathbf{r}')\mathbf{J}(\mathbf{r}) \quad (2.35)$$

The right-hand side of Eq. (2.35) can be physically treated as the excited electric field $\mathbf{E}_{excited}$ throughout the volume V_m by the incident electric field and the contributions from all the other cells V_k. By invoking the long-wave approximation, Eq. (2.35) can be further converted into a set of simultaneous algebraic equations that are solved using standard procedures.

$$\mathbf{E}_i^{incident} = \mathbf{E}_i^{excited} - \sum_{i\neq j} \mathbf{G}_{ij}\boldsymbol{\alpha}_{ij}\mathbf{E}_j^{excited} \quad (2.36)$$

where $\boldsymbol{\alpha}_{ij}$ is the polarization tensor[73]. A review about the calculation of $\boldsymbol{\alpha}_{ij}$ has been given by Yurkin and Hoekstra [72].

Fig. 2.5 shows the scattering diagram of a sphere, computed with the Lorenz-Mie theory and the DDA method respectively. Comparing these two scattering diagrams, the agreement in the forward direction is excellent and only small deviations can be observed in the direction of backward scattering.

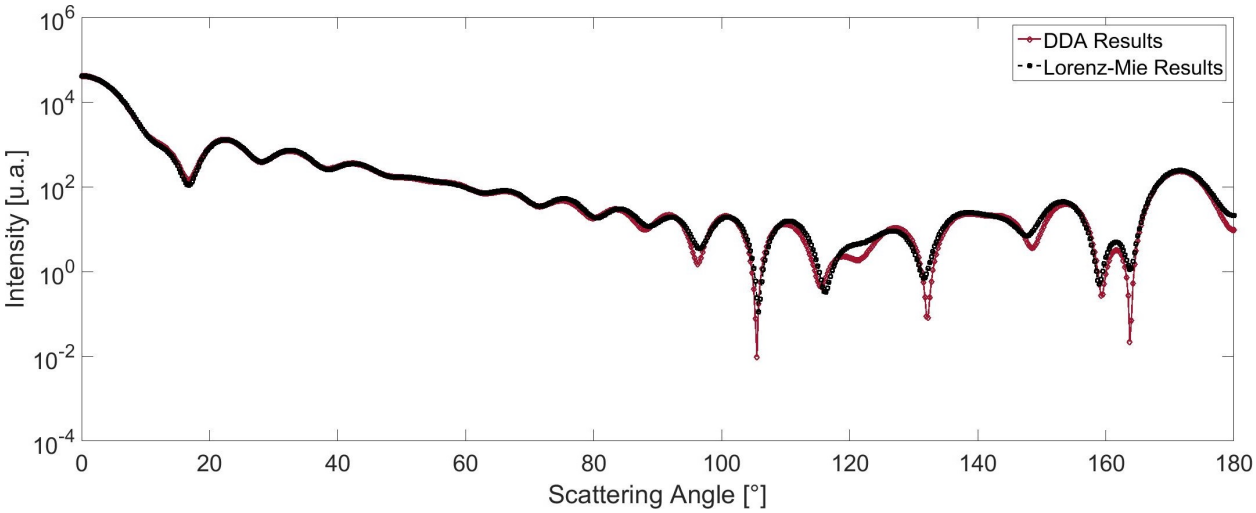

Figure 2.5: Comparison of the scattering diagram of a spherical particle illuminated by a plane wave for parallel polarization by using the Lorenz-Mie theory and the DDA method. The results for DDA method were obtained using the ADDA code. [72] (Refractive index of medium is 1, refractive index of particle is 1.4, size of particle 2.5μm, wavelength of the plane wave 405 nm)

2.2.4 Ray-tracing technique

For particles with a large size parameter and a smooth surface, a complete electromagnetic description of the scattering is computationally time consuming; the ray-tracing method then provides a faster approach to obtain the light scattering properties of particles. Numerous studies have been conducted for improving the ray-tracing technique. In the study from Hovenac and Lock [16], forward diffraction has been taken into consideration; in Yang and Liou's integral geometrical optics model, the ray-tracing technique has been combined with electromagnetic wave method to solve the near field and far field of the light scattering from ice crystals [66]; in the vector complex ray model from Ren et al. [48], the divergence of a ray bundle has been considered. One direct comparison of the geometrical optics approach and optical measurements of arbitrarily shaped particles was published by Stegmann and Tropea. [57]

When the incident beam is not a plane wave, it can be expanded as the sum of many individual plane waves using a Fourier decomposition. Therefore, only the plane wave will be discussed here. The ray-tracing method treats the light source as a bundle of light rays. Each ray is specified with an amplitude A_q, phase ψ_q and propagation direction $\mathbf{k}_i$, as Eq. (2.37) describes.

$$\mathbf{E} = A_{q\mu} \exp(-i\psi_q)\mathbf{k}_i \tag{2.37}$$

The polarization state of the light rays is described with the Stokes vector $\mathbf{S}$. When the light ray intersects with matter, at the intersection boundary it will be reflected and transmitted. The reflection and the transmission follows the Fresnel's equation and Snell's law [14]; an alternative way is to track the Stokes vector by multiplying the Mueller matrix and the rotation matrix [29], which will be discussed in Chapter 3 in more detail. Fig. 2.6 illustrates the reflection and transmission of the electromagnetic wave at an intersection boundary for different polarization states. Fig. 2.7 shows

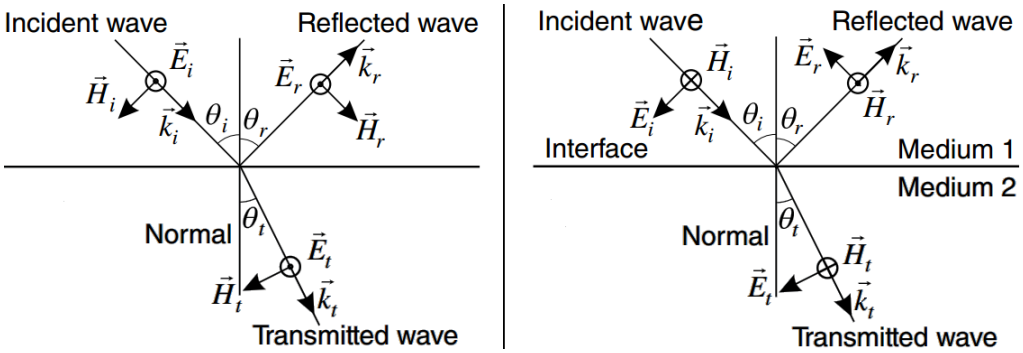

Figure 2.6: Sketch of reflection and refraction at an intersection boundary for different polarization of the electromagnetic wave.

the scattering diagram of a water drop with a diameter of 800 μm, computed using the Lorenz-Mie theory and the three-dimensional ray-tracing technique respectively. Fig. 2.8 shows the scattering diagram for the first four scattering orders, computed with the Debye series decomposition and the ray-tracing technique respectively. For particles with a large size parameter, the scattering diagrams computed with the ray-tracing technique exhibit very good agreement with the Lorenz-Mie theory.

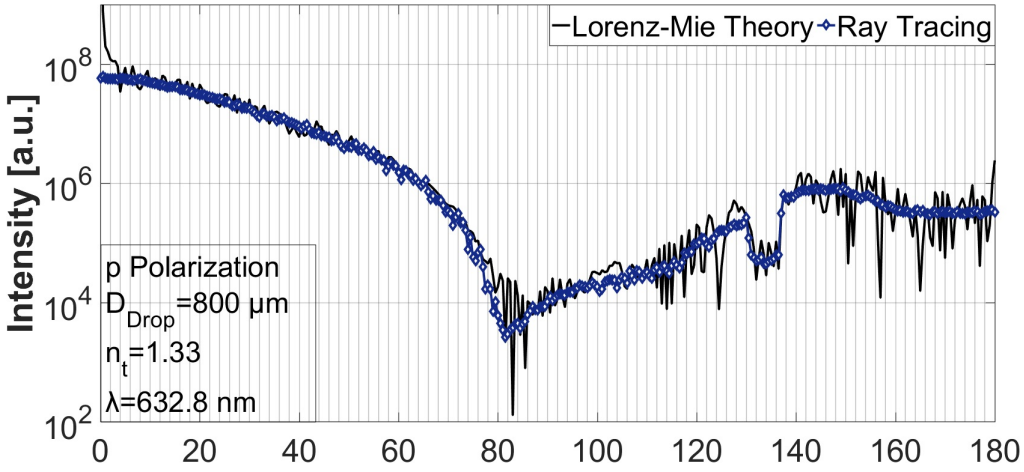

Figure 2.7: Comparison of parallel polarized scattering diagrams from Lorenz-Mie theory and geometrical optics for a sphere. The results for Debye series decomposition and the ray-tracing method from Young were obtained using the MiePlot software [25]. ($D_{Drop} = 800$ μm, $n_t = 1.33$, $\lambda = 0.6328$ μm). Reproduced from [28].

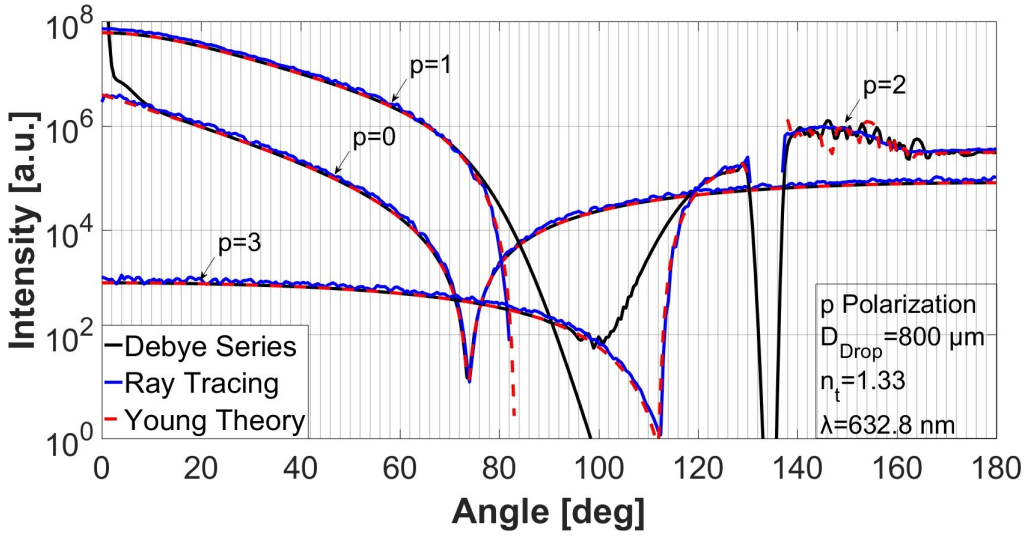

Figure 2.8: Comparison of parallel polarized scattering diagrams from Debye series decomposition, ray-tracing method from Young and geometrical optics for a sphere. The results for Debye series decomposition and the ray-tracing method from Young were obtained using the MiePlot software [25]. (D_{Drop}=800 μm, $n_t = 1.33$, $\lambda = 0.6328$ μm). Reproduced from [28].

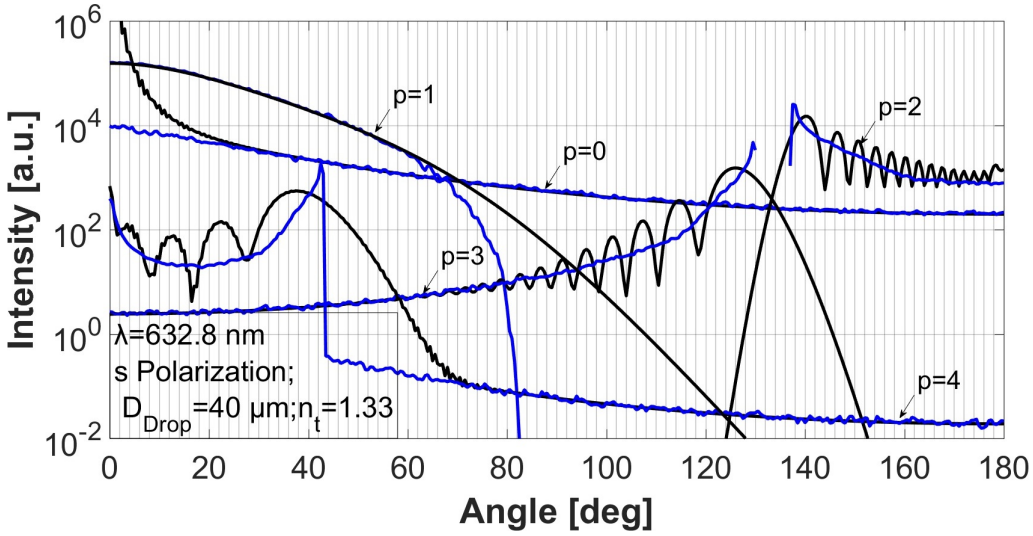

Figure 2.9: Comparison of orthogonal polarized scattering diagrams from Debye Series and geometric optic for a sphere. Black line and blue line represents the scattering diagram from the Debye Series and geometric optic separately for different scattering orders. ($D_{Drop} = 40$ μm, $n_t = 1.33$, $\lambda = 0.6328$ μm)

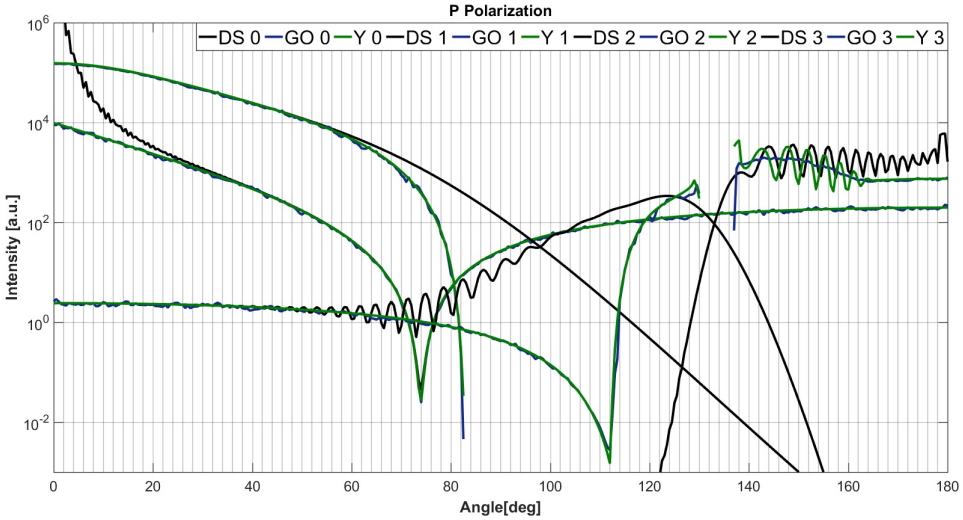

Figure 2.10: Comparison of parallel polarized scattering diagrams from Debye Series (DS), geometric optics (GO) and Young theory (Y) for a sphere. The black line and blue line represent the scattering diagram from the Debye Series and geometric optic separately for different scattering orders. ($D_{Drop} = 40\ \mu m$, $n_t = 1.33$, $\lambda = 0.6328\ \mu m$)

As the Figs. 2.8 and 2.9 depict, when the size parameter of the particle increases, the agreement between the results from geometric optics and the Lorenz-Mie theory becomes better.

3 Simulation of light scattering by particles with inclusions

This chapter deals with the simulation of light scattering from complex particles. The simulations were carried out for drop with an embedded spherical flake, drop with an embedded spherical particle and for drop with multiple nanoparticle inclusions.

3.1 Light scattering from a drop with an embedded particle

This part of the study is devoted to light scattering from drops with an embedded particle, as would be expected in an encapsulation/coating process or with spraying of metallic paints. A ray-tracing approach is taken, in which the polarization and intensity of all rays impinging onto a defined detector aperture are documented, allowing the signal generation arising from the drop passing through a plane wave or focused Gaussian beam to be simulated. The geometric situation considered is that of a spherical drop with a single embedded spherical particle or flake, situated arbitrarily in the drop. It will be assumed that any rays intersecting the embedded particle are fully reflected at the interface. Parts of this work have been published in the article "Light scattering from a drop with an embedded particle and its exploitation in the time-shift technique" (Journal of Quantitative Spectroscopy and Radiative Transfer, 227, 20-31) [28])

Overview of algorithm

The input parameters to the code include the above-mentioned parameters of the incident beam, the geometric parameters of the drop and embedded particle, and the relative refractive index between medium and drop, n_t. Furthermore, the number of scattering orders to be computed must be specified. The drop is described by the generalized ellipsoidal form:

$$\frac{x^2}{a^2} + \frac{y^2}{b^2} + \frac{z^2}{c^2} = 1 \tag{3.1}$$

in which, the a, b and c are the half-axes of the ellipsoid. Similarly, the embedded particle is also described using the general ellipsoidal form, albeit with a possible offset within the drop (x_0, y_0, z_0), the center of the drop being the origin of the coordinate system:

$$\frac{(x-x_0)^2}{R_x^2} + \frac{(y-y_0)^2}{R_y^2} + \frac{(z-z_0)^2}{R_z^2} = 1 \tag{3.2}$$

Although the algorithm is capable of accepting ellipsoidal drops and particles with arbitrary orientation with respect to the incident beam, the present study is restricted to spherical geometries for the main drop and for the embedded particles, i.e. $a = b = c, R_x = R_y = R_z$. Furthermore, the drops and flakes are aligned such that the drop centered x axis coincides with the beam X axis.

The first step determines which of the initial rays intersect with the drop. If intersection occurs, the intersection coordinate is determined and is used as the basis for the normal vector $\mathbf{n}$, the incident angle θ_i, reflected angle θ_r and refracted (transmitted) angle θ_t. The coordinate of the intersection points from each scattering order of each ray are saved in a cell, which is a data type in

Matlab. When the ray impinges on the outer drop surface, the amplitudes of the electric field of the reflected ray and refracted ray are given by the Fresnel equations, whereby the incident electric field amplitude $\mathbf{E}_i$ is decomposed into two parts: $\mathbf{E}_{pi}$, which is parallel to the plane of incidence, and $\mathbf{E}_{oi}$, which is orthogonal to the plane of incidence.

$$\mathbf{E}_i = \mathbf{E}_{pi} + \mathbf{E}_{oi} \tag{3.3}$$

$$\mathbf{E}_{oi} = \frac{\mathbf{E}_i \cdot (\mathbf{n} \times \mathbf{k}_i)}{(|\mathbf{n} \times \mathbf{k}_i|)^2} \cdot (\mathbf{n} \times \mathbf{k}_i) \tag{3.4}$$

$$\mathbf{E}_{pi} = \mathbf{E}_i - \mathbf{E}_{oi} \tag{3.5}$$

These two decomposed vectors are then used to compute the parallel (p) and perpendicular (o) electric fields for transmitted and reflected light, respectively, using the Fresnel amplitude coefficients

$$\mathbf{E}_{pr} = \mathbf{E}_{pi} * r_{||} \tag{3.6}$$

$$\mathbf{E}_{pt} = \mathbf{E}_{pi} * t_{||} \tag{3.7}$$

$$\mathbf{E}_{or} = \mathbf{E}_{oi} * r_{\perp} \tag{3.8}$$

$$\mathbf{E}_{ot} = \mathbf{E}_{oi} * t_{\perp} \tag{3.9}$$

$$\mathbf{E}_r = \mathbf{E}_{pr} + \mathbf{E}_{or} \tag{3.10}$$

$$\mathbf{E}_t = \mathbf{E}_{pt} + \mathbf{E}_{ot} \tag{3.11}$$

In the plane of incidence, measured in the clockwise direction, the rotation angle of the reflected ray and transmitted ray are given by:

$$\theta_{rot_r} = \pi + 2\theta_i \tag{3.12}$$

$$\theta_{rot_t} = |\theta_i - \theta_t| \tag{3.13}$$

For the ray with parallel polarization, after using the Fresnel equation to calculate the amplitude of the reflected and transmitted electric field, rotation is needed to obtain the vector of the reflected electric field and transmitted electric field. The 3D rotation is based on the Rodrigues' rotation formula [2]

$$\mathbf{V}_{rot} = \mathbf{V}\cos\theta + (\mathbf{D}_{RA} \times \mathbf{V})\sin\theta + \mathbf{D}_{RA}(\mathbf{D}_{RA} \cdot \mathbf{V})(1 - \cos\theta) \tag{3.14}$$

$\mathbf{V}$ is the vector to be rotated; Vector $\mathbf{D}_{RA}$ is the unit vector that describes the rotation axis. It is the cross product of any two unit non-zero vectors $\mathbf{A}_i$ and $\mathbf{B}_i$ in the plane of rotation.

$$\mathbf{D}_{RA} = \frac{\mathbf{A}_i \times \mathbf{B}_i}{|\mathbf{A}_i \times \mathbf{B}_i|} \tag{3.15}$$

For the computation of the first scattering order, the code checks whether the transmitted ray impinges onto the embedded particle; for subsequent scattering orders, the code checks whether the (internally) reflected ray again impinges onto the embedded particle. For rays reflected from the embedded particle, the amplitude of the electric field remains the same after reflection.

For each ray, the computation for one scattering order is followed by the computation for the next scattering order, based on the computational results up to that stage. This process is repeated until the computation of all prescribed scattering orders of all rays is complete. The scattered intensity is the intensity sum of all rays impinging onto the detector surface. All rays are treated completely incoherent, and the intensity of individual rays is first computed. If M stands for the number of the rays which falls onto the prescribed detector aperture, the total received intensity is given by

$$I_k = \frac{c_l n \epsilon_0}{2} |\mathbf{E}_k|^2 \tag{3.16}$$

$$I_{total}(\theta_i, \phi_i) = \sum_{k=1}^{M} I_k \tag{3.17}$$

in which c_l is the speed of the light in vacuum, n is the refractive index and ϵ_0 is the permittivity in vacuum.

3.1.1 Scattering diagrams for a drop with an embedded spherical particle

Following the validation of the ray-tracing code, scattering diagrams for a drop with an embedded particle have been computed. First an embedded spherical particle will be examined, followed by an embedded circular flake. In the scope of the geometric optics, the size of the drop will have no influence on the computed scattering diagrams or later on the simulated signals generated by a time-shift optical configuration, other than through the scattered intensity; therefore, all geometric dimensions are scaled to the drop diameter to achieve a more universal representation of the results, including the relative position (x_0, y_0, z_0) of the embedded spherical particle or circular flake.

$$D_P^* = \frac{D_{Particle}}{D_{Drop}} \tag{3.18}$$

$$D_F^* = \frac{D_{Flake}}{D_{Drop}} \tag{3.19}$$

$$\psi = \frac{(x_0, y_0, z_0)}{D_{Drop}} \tag{3.20}$$

The scattered light from a drop of diameter D_{Drop} with a spherical particle of diameter $D_{Particle}$ centered and embedded in the drop has been simulated for a plane incident wave and for s polarization. The scattering plane is the YZ plane, as defined in Fig. 3.1

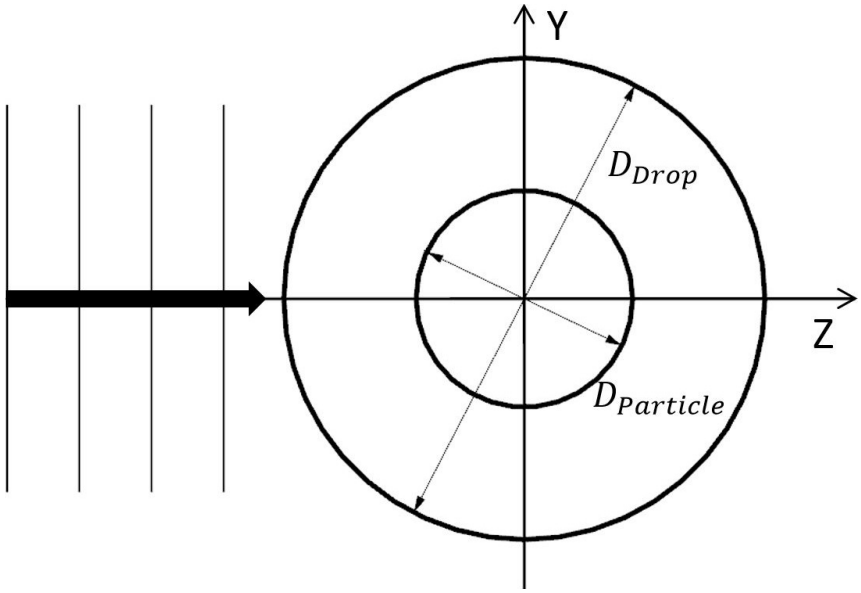

Figure 3.1: *s* polarized plane wave incident on a drop with an embedded spherical particle. Definition of coordinate system.

In the first set of simulations D_P^* is changed from 0 (no particle case for comparison) to 0.45, leaving the particle in the centre of the drop. Figure 3.2 shows the simulation results, indicating that scattering in the forward direction is significantly affected. The scattered light from first-order refraction in the forward direction has been blocked by the embedded particle and the blocking effect increases with embedded particle size. Nevertheless, the rainbow could still be captured. This interpretation is confirmed by examining the scattering diagram for first-order refraction only, as is shown in 3.3.

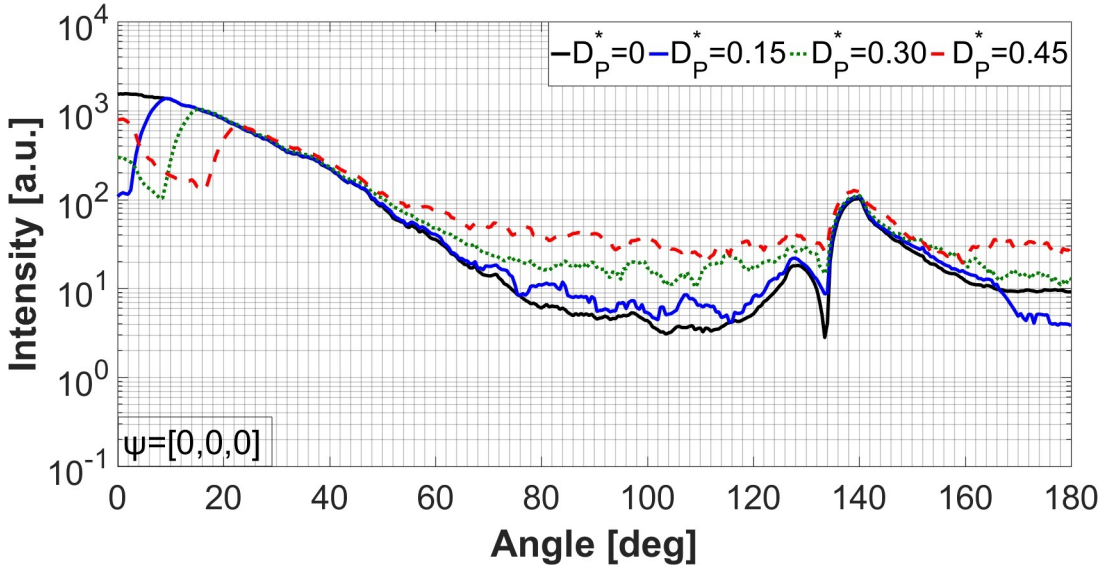

Figure 3.2: Simulation results by changing diameter of particle. ($n_t = 1.33$). Reproduced from [28].

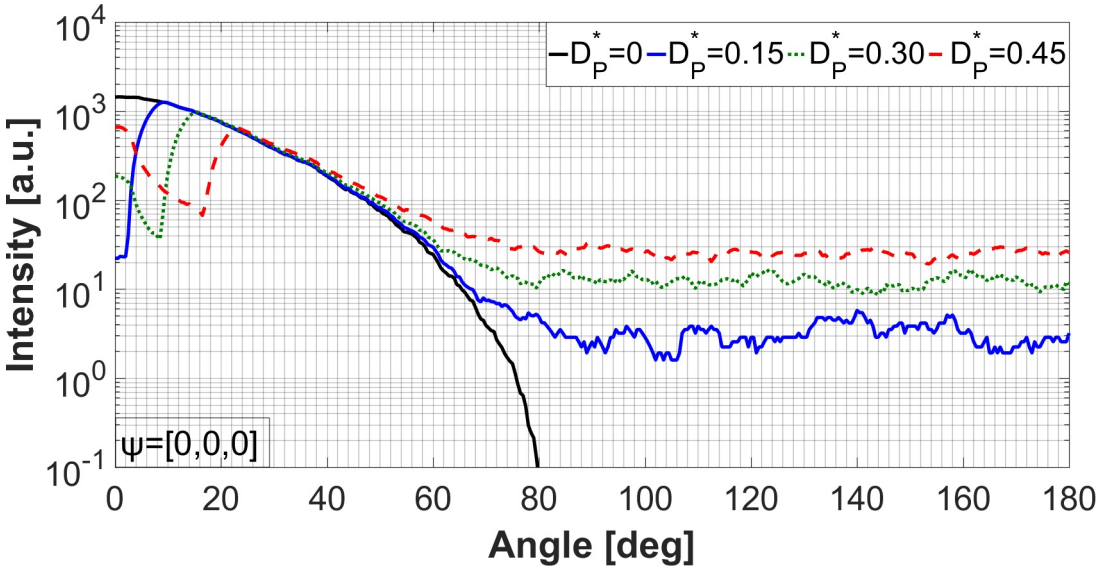

Figure 3.3: Scattering diagram for first-order refraction and varying the diameter of the embedded particle. ($n_t = 1.33$). Reproduced from [28].

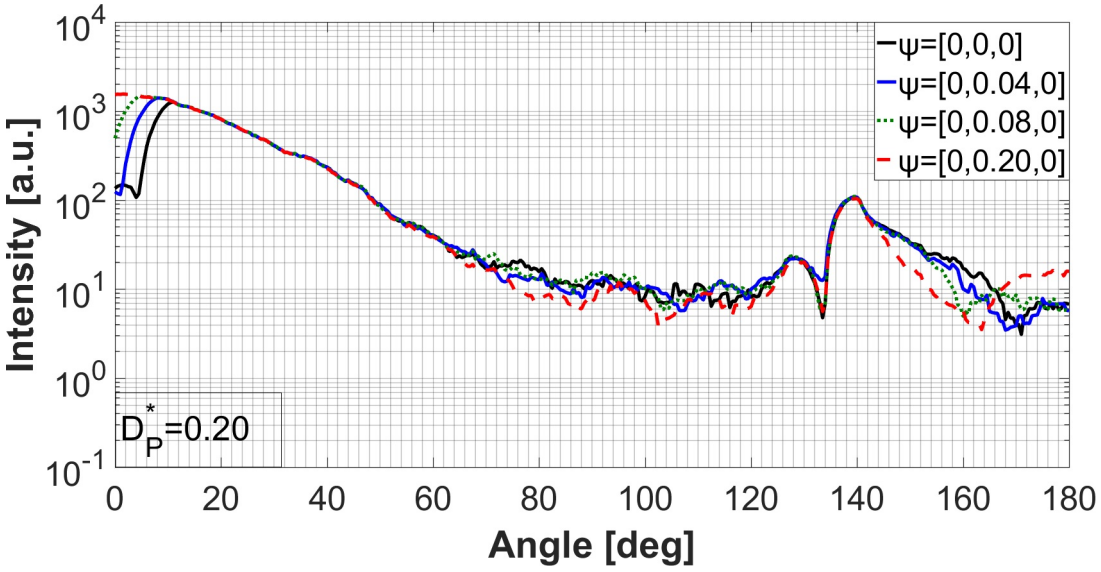

Figure 3.4: Simulation results by varying the position of embedded particle on the Y-axis. ($n_t = 1.33$). Reproduced from [28].

Clearly the first-order refraction is the scattering order being affected by the embedded particle in the forward direction (compare to the result without a particle inside, $D_P^* = 0$). However, a uniform backward scattering level is also obtained. This backward scattering arises from light reflecting off the surface of the embedded particle and could be useful for detecting an embedded particle. The results obtained by changing the position of the particle along the Y-axis are shown in Fig. 3.4. This figure shows that by changing the y position of the embedded particle, also the forward scattering is affected, since the blocking effect of first-order refraction will depend on the particle position. As before, a uniform backscatter intensity is obtained. Fig. 3.5 shows the simulation results when changing the z position of the embedded particle. Compared with the results shown in Fig. 3.4, the scattering exhibits less sensitivity to position changes in the z direction.

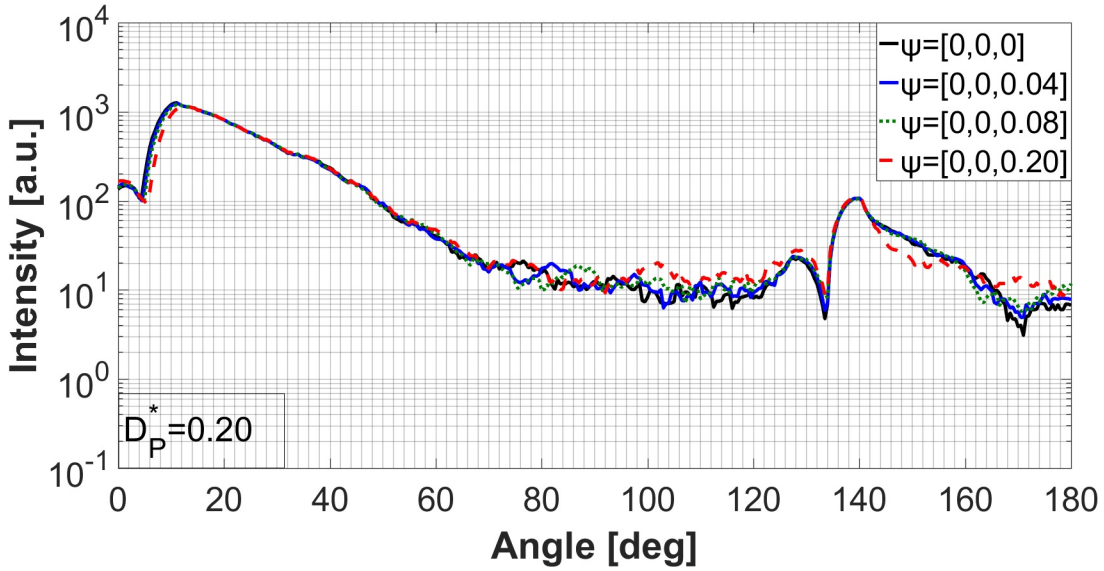

Figure 3.5: Simulation results by varying the position of embedded particle on the Z-axis. ($n_t = 1.33$). Reproduced from [28].

3.1.2 Scattering diagrams for drop with embedded flake

A flake inside the drop is treated as a flat disc, with the flake center at some (x, y, z) coordinate, with dimensionless diameter D^*_{Flake} and the surface normal $\mathbf{n}$. The surface normal is a vector with the zenith angle α and azimuthal angle β, as shown in Fig. 3.6.

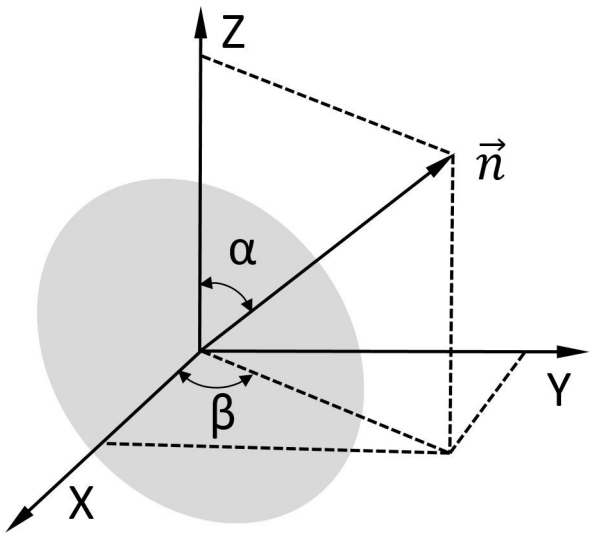

Figure 3.6: Description of the normal vector of the flake in a Cartesian coordinate system. (scattering plane: YZ plane). Reproduced from [28].

Using the zenith angle and azimuthal angles, the normal vector of the flake can be described as [59]:

$$\mathbf{n} = \begin{pmatrix} \mathbf{n}1 \\ \mathbf{n}2 \\ \mathbf{n}3 \end{pmatrix} = \begin{pmatrix} \mathbf{e}_x \cdot \mathbf{n}1 \\ \mathbf{e}_y \cdot \mathbf{n}2 \\ \mathbf{e}_z \cdot \mathbf{n}3 \end{pmatrix} = \begin{pmatrix} \sin\alpha \cdot \cos\beta \\ \sin\alpha \cdot \sin\beta \\ \cos\alpha \end{pmatrix} \tag{3.21}$$

To analyse the effect of the flake on the scattering diagram under the p polarized plane wave, the scattered intensity has been normalized and plotted together with the results without a flake and compared to the Lorenz–Mie solution with Debye series decomposition. Such a comparison is shown in Fig. 3.7 for the reflection scattering order. As expected, the embedded flake does not influence the scattering through reflection and the geometric optics solution does not include diffraction in forward scatter.

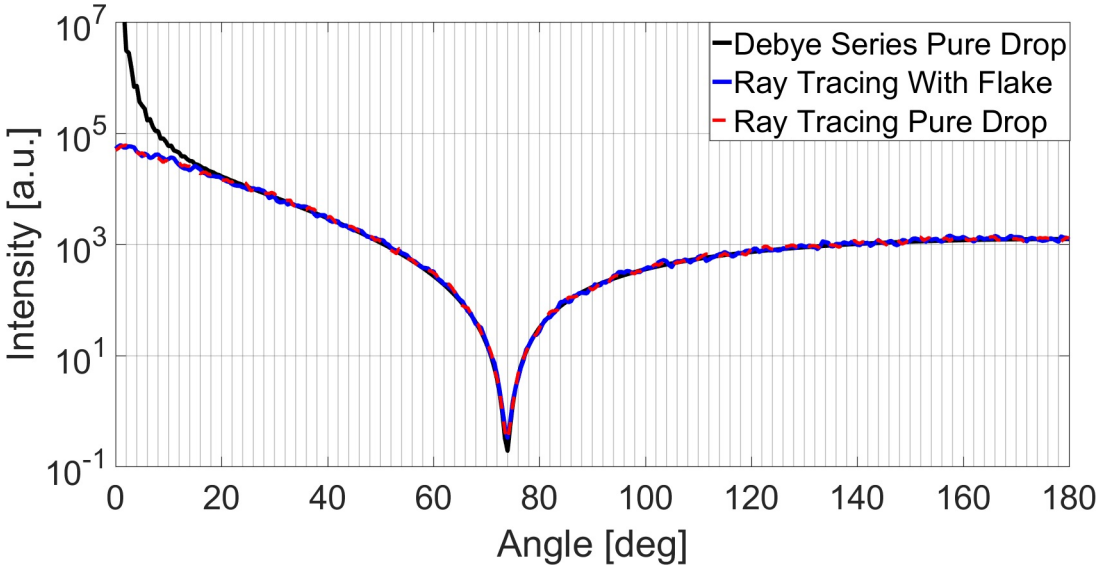

Figure 3.7: Comparison of the reflection scattering order (p=0) for the parameters: $D_F^* = 0.60$, $\psi = [0, 0, 0]$, $\alpha = 0$ deg, $\beta = 0$ deg, $n_t = 1.33$. Reproduced from [28].

A similar comparison for the same drop is given in Fig. 3.8 for first-order refraction. The scattering diagram indicates that the flake now blocks some of the light in forward scattering; the blocking angle is indicated in Fig. 3.9. Additional light is scattered in the backward direction; this light comes from reflection off the surface of the flake.

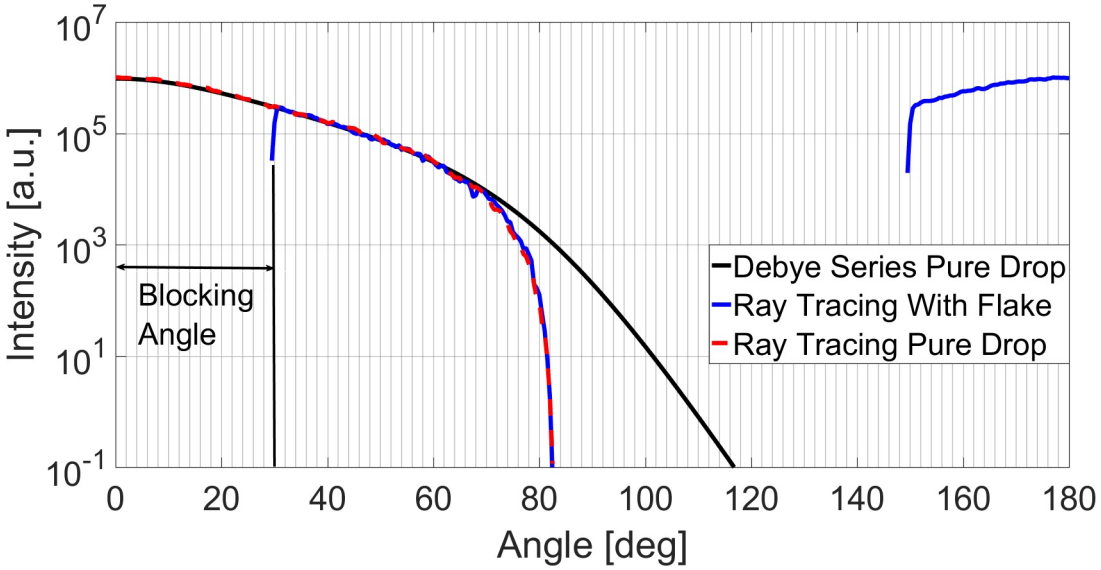

Figure 3.8: First-order refraction scattering: comparison of Lorenz-Mie solution, ray tracing without flake, ray tracing with flake: $D_F^* = 0.60$, $\psi = [0, 0, 0]$, $\alpha = 0$ deg , $\beta = 0$ deg, $n_t = 1.33$. Reproduced from [28].

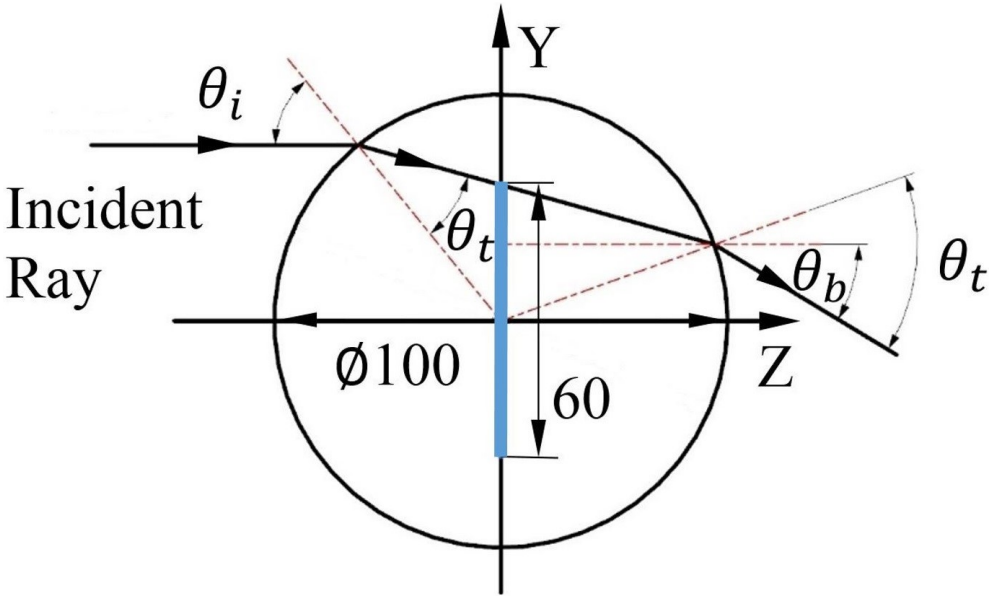

Figure 3.9: Disk positioned inside the drop can block the transmission of first-order refractive rays: $D_F^* = 0.60$, $\psi = [0, 0, 0]$, $\alpha = 0$ deg, $\beta = 0$ deg, $n_t = 1.33$. Reproduced from [28].

The blocking angle θ_b of first-order refraction in the forward direction, as depicted in figure 3.9, can be analytically expressed using the equations:

$$\frac{r}{\sin\theta_t} = \frac{R}{\sin(0.5 * \pi + \sin^{-1}(\sin\theta_t * n_t) - \theta_t)} \tag{3.22}$$

$$\theta_b = 2 * (\theta_i - \theta_t) \tag{3.23}$$

The same comparison is shown in Fig. 3.10 for scattering of second-order refraction. In this case, the high intensity of the rainbow is properly captured; however, additional light is now found in the forward direction, again coming from reflection off the surface of the flake, as explained in Fig. 3.11(a). In Fig. 3.11, the black line with arrows represents the ray path inside the drop; the dashed line shows the imaginary ray path when the drop does not contain a flake. For rays in which only one reflection from the flake occurs (Fig. 3.11(a)), the light exits in the forward direction and this is the intensity observed in Fig. 3.10 in the angular region ca. 30–40 deg. However, if the ray reflects twice from the embedded flake, as shown in Fig. 3.11(b), then the exiting ray contributes to the backscatter intensity. It is evident that the ray path and the imaginary ray path, shown by the dashed line, share the same exit point and exit the drop with the same angle as for second-order scattering; therefore, the backward scattering from the second-order refraction does not change much, as Fig. 3.10 illustrates.

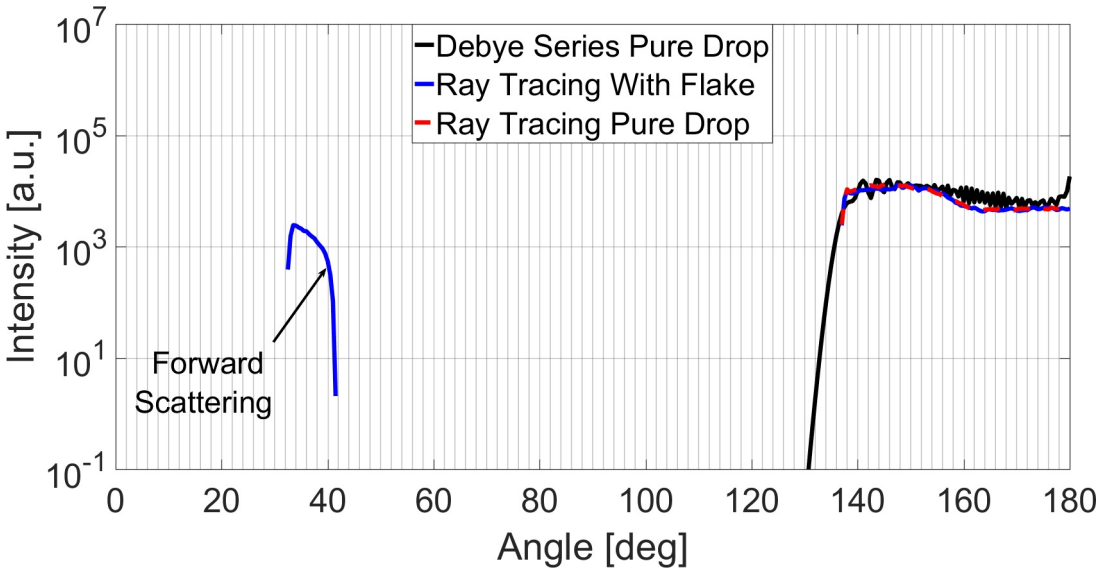

Figure 3.10: Comparison of second-order refraction scattering (p=2) for the parameters: $D_F^* = 0.60$, $\psi = [0, 0, 0]$, $\alpha = 0$ deg, $\beta = 0$ deg, $n_t = 1.33$. Reproduced from [28].

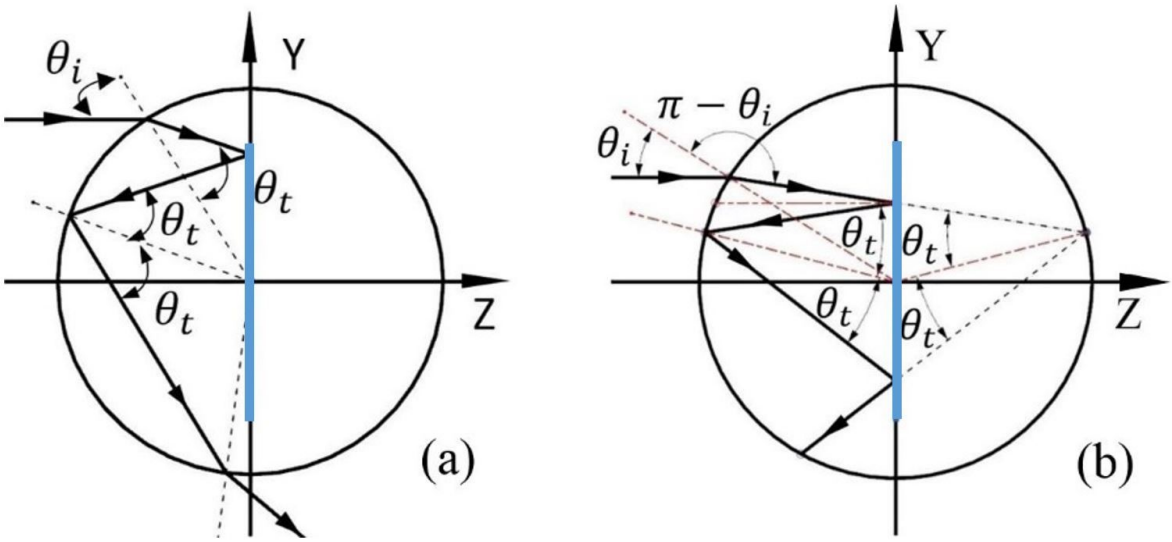

Figure 3.11: Ray path for second-order refraction scattering (a) Ray path for forward scattering (b) Ray path for backward scattering: D_F^*=0.60, $\psi = [0, 0, 0]$, $\alpha = 0$ deg, $\beta = 0$ deg, $n_t = 1.33$. Reproduced from [28].

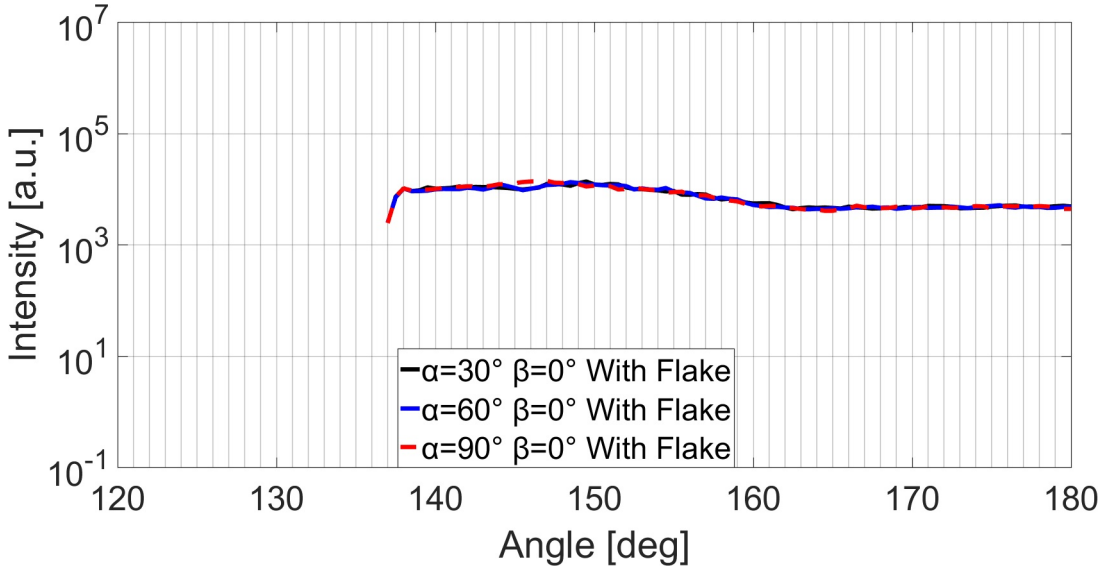

Figure 3.12: Scattering diagram for the second-order refraction scattering by varying the zenith angle: D_F^* = 0.60, ψ = [0, 0, 0], β = 0 deg, n_t = 1.33. Reproduced from [28].

The previous results were obtained using a flake azimuthal angle of 0 deg and a zenith angle of 0 deg. In the following, the azimuthal angle remains at 0 deg, but the zenith angle varies from 30 deg to 90 deg with an interval of 30 deg. The embedded flake does not affect the reflection of the drop; therefore, the reflection intensity at 0 deg scattering angle has been used as reference to normalize the scattering intensity from the second-order scattering. This normalized second-order scattering for different zenith angles has been plotted in Fig. 3.12, whereby only the backscatter region is shown, since this will be the more interesting region for application to the time-shift technique. The scattering intensity in the backscatter direction near the rainbow is almost unaffected by the flake. This is because most incident rays intersect with the flake twice as shown in Fig. 3.11(b).

Further scattering diagrams have been computed for zenith and azimuthal angles of 0 deg but varying the size of the flake. D_F^* is varied from 0.20 to 0.60 with intervals of 0.20. Fig. 3.13 shows the scattering diagram for first-order refraction scattering. As expected, when the flake size becomes larger, the blocking angle of the first- order scattering also becomes larger and the backward scattering becomes stronger, because of total reflection from the flake.

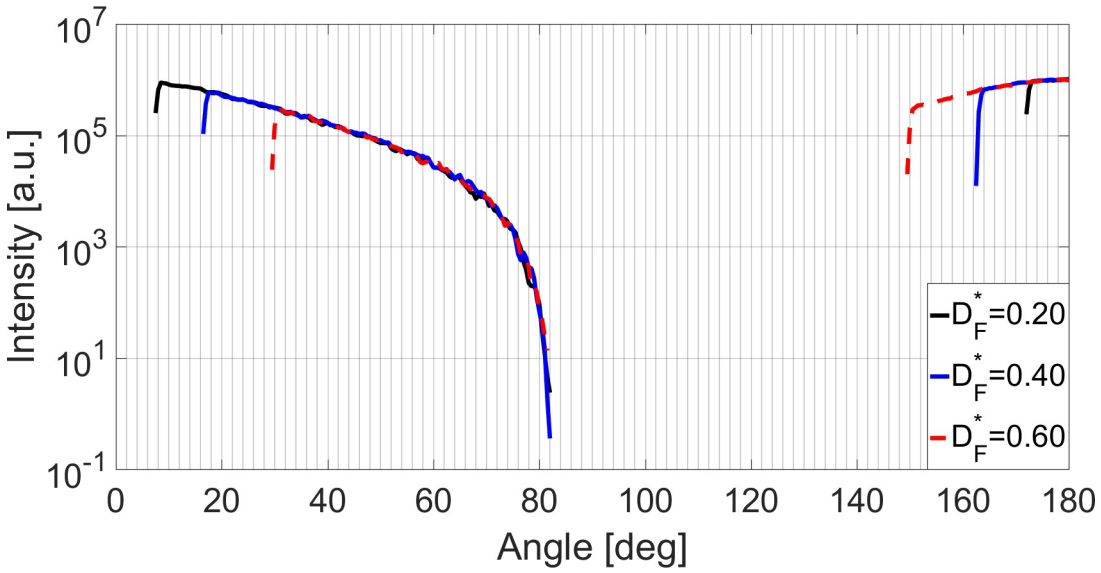

Figure 3.13: Comparison for the first-order scattering for varying D_F^*: $\psi = [0, 0, 0]$, $\alpha = 0$ deg, $\beta = 0$ deg, $n_t = 1.33$. Reproduced from [28].

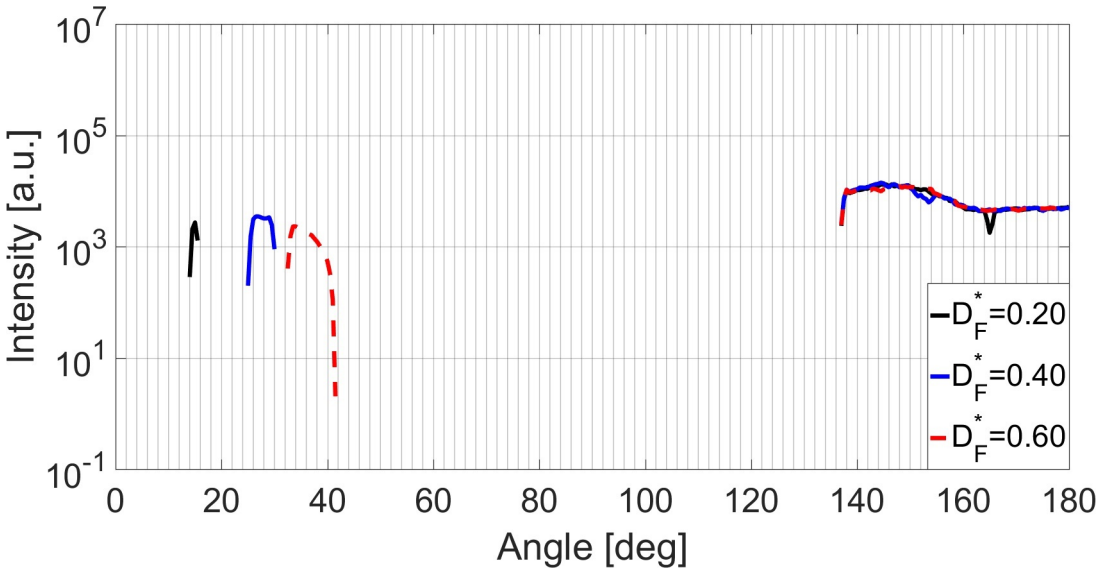

Figure 3.14: Comparison for the second-order scattering for varying D_F^*: $\psi = [0, 0, 0]$, $\alpha = 0$ deg, $\beta = 0$ deg, $n_t = 1.33$. Reproduced from [28].

Fig. 3.14 shows the scattering diagram for second-order refraction scattering. For second-order scattering, as the flake size increases the scattered intensity in backscatter does not change much, the reason is that most rays intersect with the flake twice, so the rays share the same exit point and exit the drop with same angle as if no flake exists. However, changing the flake size will affect the forward scattering of the second-order scattering, since this directly affects to what extent first-order refraction is blocked by the flake.

The scattering diagram for single scattering orders by varying the azimuthal angle is shown in Fig. 3.15, while keeping the zenith angle constant. The scattering diagrams for different azimuthal angles overlap with each other, so the scattering amplitude does not change when the zenith angle is constant at 90 deg and only the azimuthal angle varies.

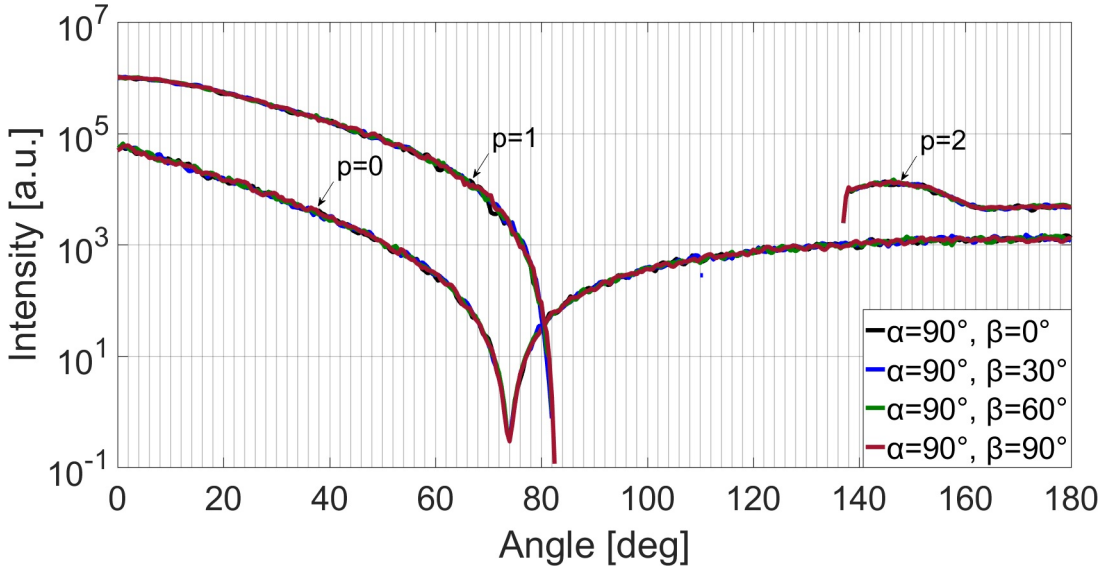

Figure 3.15: Scattering diagrams for single scattering order by varying azimuthal angle of the normal vector of the flake: $D_F^* = 0.60$, $\psi = [0, 0, 0]$, $\beta = 0$ deg, $n_t = 1.33$. Reproduced from [28].

3.2 Polarized Monte Carlo ray-tracing method for simulation the light scattering of colloidal drop

Light can be considered both a wave and a particle. When light is treated as particle, a light ray transissions within the colloidal drop is a radiative transfer problem and can be described with the radiative transfer equation. The radiative transfer equation is written as [31] [75]

$$\vec{\mathbf{S}} \cdot \nabla I(\vec{\mathbf{x}}, \vec{\mathbf{S}}) = -\mu_{ext} I(\vec{\mathbf{x}}, \vec{\mathbf{S}}) + \mu_{sca} \int_{\Omega} I(\vec{\mathbf{x}}, \vec{\mathbf{S}}_i) P(\vec{\mathbf{x}}, \vec{\mathbf{S}}, \vec{\mathbf{S}}_i) d\Omega(\vec{\mathbf{S}}) \tag{3.24}$$

in which the $\vec{\mathbf{S}}$ is the vector for the scattered direction; $\vec{\mathbf{S}}_i$ is the vector for the incident direction; $\mathbf{x}$ is the scattering point. Therefore, by integration of Eq. (3.24), the intensity scattered in the direction $\vec{\mathbf{S}}$ at the scattering point $\mathbf{x}$ is formulated as

$$I(\vec{\mathbf{x}_0}, \vec{\mathbf{S}_0}) = t_{trans}(\vec{\mathbf{x}_0}, \vec{\mathbf{u}_0}) I(\vec{\mathbf{u}_0}, \vec{\mathbf{S}_0}) + \int_{\vec{\mathbf{u}_0}}^{\vec{\mathbf{x}_0}} d\vec{\mathbf{x}_1} t_{trans}(\vec{\mathbf{x}_0}, \vec{\mathbf{x}_1}) \beta(\vec{\mathbf{x}_1}) \int_{\Omega} I(\vec{\mathbf{x}_1}, \vec{\mathbf{S}_1}) P(\vec{\mathbf{x}_1}, \vec{\mathbf{S}_0}, \vec{\mathbf{S}_1}) d\Omega(\vec{\mathbf{S}_1}) \tag{3.25}$$

in which t_{trans} is the transmittance of the medium between the points $\vec{\mathbf{x}'}$ and $\vec{\mathbf{x}}$ and is given as

$$t_{trans}(\vec{\mathbf{x}}, \vec{\mathbf{x}'}) = \exp\left[-l_{op}(\vec{\mathbf{x}}, \vec{\mathbf{x}'})\right] \tag{3.26}$$

in which l_{op} is formulated as

$$-l_{op}(\vec{\mathbf{x}}, \vec{\mathbf{x}'}) = \int_{\vec{\mathbf{x}'}}^{\vec{\mathbf{x}}} d\vec{\mathbf{x}''} \mu_{ext}(\vec{\mathbf{x}''}) \tag{3.27}$$

For multiple scattering within the colloidal drop, the solution of Eq. (3.25) can be obtained through iteration. The radiative transfer equation can be solved indirectly by using the Monte Carlo method, which simulates the radiative transfer processes [41][75]. The Monte-Carlo ray-tracing method, which combines the geometric optic method and the Lorenz-Mie theory, has been used to simulate

light scattering when the host particle contains multiple nanoparticle inclusions with a uniform size distribution. This approach was derived from Monte-Carlo methods used in radiative transfer problems, such as the lidar satellite observation problem discussed by Stegmann et al [56]. The Lorenz-Mie theory has been used to compute the phase function of the nanoparticle inclusions within the host drop. Parts of this section have been published in the article "Simulation of light scattering from a colloidal drop using a polarized Monte Carlo method: application to the time-shift technique".[29].

The optical mean free path

The optical mean free path $E(L)$ has been introduced to simulate the light scattering of the turbid medium. The optical mean free path describes the average distance travelled by a light ray between successive interactions with the inclusions. Besides the optical mean free path, the equivalent designations "optical mean path length" and the "transport mean free path" are also sometimes used when describing the optical properties of the turbid medium. The transport mean free path length refers to the mean distance, after which the direction of photon becomes random. As an example, the three solutions pictured in Fig. 3.16 have the same volume concentration of nanoparticles (inclusions); however, the size of the nanoparticles differ: from left to right the sizes are 30 nm, 200 nm and 600 nm. Since the extinction efficiency factor is dependent on the size of the nanoparticles, the three solutions exhibit different optical mean free paths. The optical mean free path for these three different solutions from left to right are 31510.46 μm, 315.06 μm and 105.78 μm respectively, which are much larger than the wavelength of the incident beam of a time-shift instrument. Therefore, the propagation of the light ray in the solution can be considered as independent or incoherent.

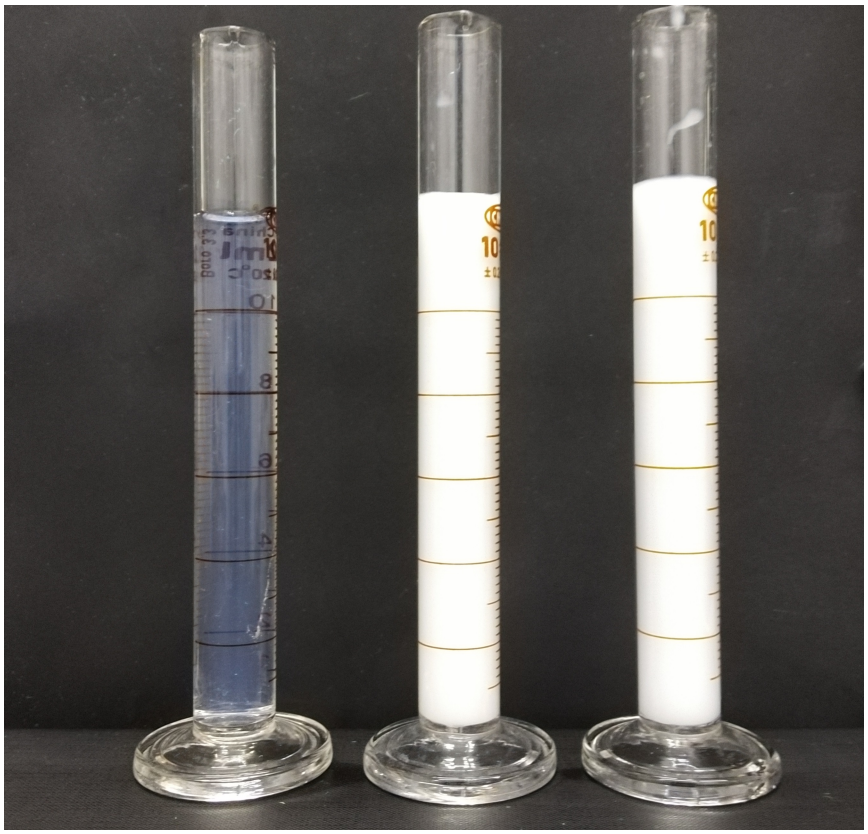

Figure 3.16: Three solutions containing polystyrene nanoparticles of different sizes. The volume concentration of the nanoparticles in the solutions are 0.14%. The diameter of the nanoparticles within the solutions, from left to right are: 30 nm, 200 nm and 600 nm.

Because of the importance of the optical mean free path for the simulation of the light scattering from colloidal drops, a derivation of this parameter will be given. The change of intensity after the photon travelling a distance ds satisfies the Eq. (3.28).

$$dI = -\mu_e I ds \tag{3.28}$$

where I is the intensity of the incoming light; μ_e is the extinction coefficient of the medium, which has the units m^{-1}; μ_a and μ_s are the absorption and scattering coefficients respectively; they satisfy the relationship

$$\mu_e = \mu_a + \mu_s \tag{3.29}$$

Integrating both sides of Eq. (3.28) yields

$$\ln \frac{I}{I_0} = -\mu_e s \tag{3.30}$$

$$\frac{I}{I_0} = e^{-\mu_e s} \tag{3.31}$$

As Eq. (3.31) indicates, the intensity of the light decays e^{-1} after travelling the distance μ_e^{-1}. The probability that the photon is absorbed or scattered between the path s and $s + ds$ is given as

$$dP(s) = \frac{I(s) - I(s + ds)}{I_0} = \frac{1}{\mu_e} e^{-\mu_e s} ds \tag{3.32}$$

The average value of the free path length can be written as

$$\langle s \rangle = \int_0^\infty s dP(s) = \frac{1}{\mu_e} \tag{3.33}$$

Therefore, the optical mean free path is written as

$$E(L) = \langle s \rangle = \frac{1}{\mu_e} \tag{3.34}$$

which is simply the inverse of the extinction coefficient.

Geometric model of the colloidal drop

In the following subsection a description of how a colloidal drop is mathematically represented will be presented. The spherical host drop has a diameter of D and the colloidal particles within have a uniform diameter of d, as pictured in Fig. 3.17. The volume of the drop and the particles are denoted V_D and V_P respectively. The extinction cross-section σ_e of the embedded particles is $Q_{ext}\pi d^2/4$, whereby Q_{ext} is the extinction efficiency factor. The refractive indices of the surrounding medium, drop and the colloid particles are n_1, n_2 and n_3 respectively. The colloidal particles are randomly distributed in space within the drop.

For packed multi-spherical particle systems, the extinction coefficient is given as

$$\mu_e = N\sigma_e = NQ_{ext}\pi r^2 \tag{3.35}$$

where N is the number density of the colloidal particles, obtained using

$$N = \frac{C_v \times V_D}{V_P \times V_D} = \frac{3C_v}{4\pi r^3} \tag{3.36}$$

whereby C_v is the volume fraction of the colloidal particles in the drop. The optical mean free path can then be formulated as [35]

$$\mathbf{E}(L) = \frac{1}{\mu_e} = \frac{V_p}{C_v \cdot \sigma_e} = \frac{4r}{3C_v Q_{ext}} \tag{3.37}$$

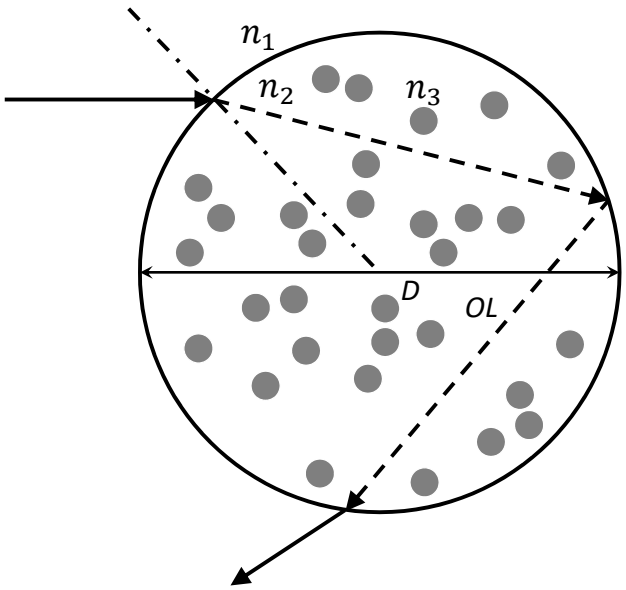

Figure 3.17: Drop with diameter D containing colloidal particles with diameter of d. The refractive indices of medium, drop and colloidal particles are n_1, n_2 and n_3 respectively.

When the volume concentration is lower than 3% the colloidal drop can be treated as a dilute system. The optical mean free path is used to characterize the colloidal concentration, because the attenuation of the rays transmitted through the drop obey the Lambert-Beer relation, which is used later in Chapter 4 to characterize the signal attenuation for second-order refraction scattering when the colloidal concentration is low.

Light ray intersects with drop interface

The incident beam is treated as a very large number of light rays, as in [28] [57]. The polarization state of individual light rays is specified with the Stokes vector **S**, given in Eq. (3.38) [59]. The propagation direction of the light rays is also specified, which can account for Gaussian beam properties, e.g. divergence. Nevertheless, since the measurement volume of the time-shift instrument is in the Rayleigh range of the Gaussian beam, the propagation direction of all light rays has been kept constant in the present study.

The Stokes vector is tracked during its propagation at each scattering event. After a scattering event, the light ray is scattered from the propagation direction k to a new direction k', as depicted in Fig. 3.18. The scattered Stokes vector is updated by multiplication of the rotation matrix $\mathbf{R}(\phi)$ and the Mueller matrix $\mathbf{M}(\theta)$, according to

$$\mathbf{S} = \begin{cases} I = \mathbf{E}_{||}\mathbf{E}_{||}^* + \mathbf{E}_{\perp}\mathbf{E}_{\perp}^* \\ Q = \mathbf{E}_{||}\mathbf{E}_{||}^* - \mathbf{E}_{\perp}\mathbf{E}_{\perp}^* \\ U = \mathbf{E}_{||}\mathbf{E}_{\perp}^* + \mathbf{E}_{||}\mathbf{E}_{\perp}^* \\ V = i(\mathbf{E}_{||}\mathbf{E}_{\perp}^* - \mathbf{E}_{||}\mathbf{E}_{\perp}^*) \end{cases} \tag{3.38}$$

$$\mathbf{S}_{sra}(\theta, \phi) = \mathbf{M}(\theta) \cdot \mathbf{R}(\phi) \cdot \mathbf{S}_i \tag{3.39}$$

The rotation matrix $\mathbf{R}(\phi)$ transforms the polarization state to a new incident reference frame and is written as

$$\mathbf{R}(\phi) = \begin{pmatrix} 1 & 0 & 0 & 0 \\ 0 & \cos 2\phi & -\sin 2\phi & 0 \\ 0 & \sin 2\phi & \cos 2\phi & 0 \\ 0 & 0 & 0 & 1 \end{pmatrix} \tag{3.40}$$

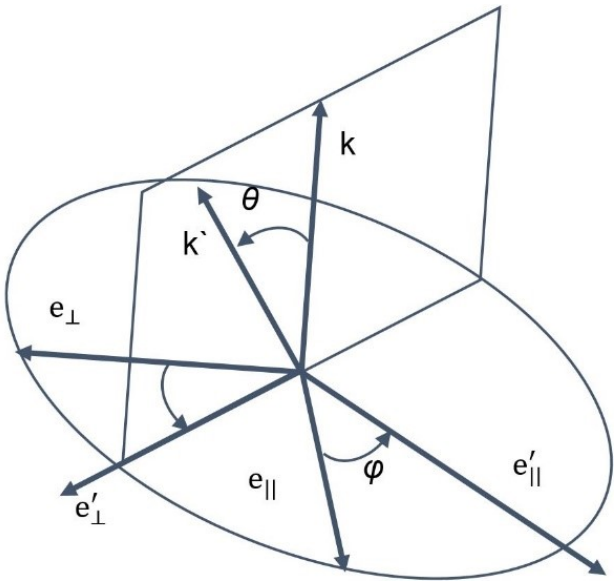

Figure 3.18: Local reference coordinate system and rotation that depicts the new propagation direction of the light ray. Reprinted with permission from [29] © The Optical Society.

The light scattering from the colloid suspension drop is simulated using a Monte Carlo ray-tracing method based on a combination of geometrical optics and Lorenz-Mie theory [6] [36] [42] [49] [52]. Light scattering at the interface between the drop and the surrounding medium is dealt with using the Fresnel equations and Snell's law [48] [70]; for the ray-tracing method used in [48], the curvature of the wave front is also considered. For tracking of the light ray path after a scattering event with a colloidal particle, the rejection sampling is used for the scattering angle sampling [17] [19] [24] [45] [46] [64]. The generation of the polar deflection angle and the azimuthal angle will be discussed later.

When the light ray intersects with the drop surface, the amplitude of the electric field of the reflected ray and transmitted ray is calculated using the Fresnel equations and Snell's law. The computational procedure can follow either a vector decomposition, as in [28] [70], or by multiplying the Stokes vector with the Fresnel equations, which should be in the form of the Mueller-Stokes matrix. The Mueller-Stokes matrix at the dielectric surface is described well in the literature; however, it does not consider the case of total internal reflection. Here the Mueller matrix at the dielectric surface is derived with consideration of the total internal reflection, to update the Stokes vector.

By treating the incident electric field and the scattered electric field separately, the scattering is described in matrix form [59]

$$\begin{pmatrix} \mathbf{E}_{s||} \\ \mathbf{E}_{s\perp} \end{pmatrix} = \frac{\exp[i \cdot k \cdot (R-z)]}{-i \cdot k \cdot R} \cdot \mathbf{S} \cdot \begin{pmatrix} \mathbf{E}_{i||} \\ \mathbf{E}_{i\perp} \end{pmatrix} \tag{3.41}$$

in which, R is the radial distance from the scattering particle; and $\mathbf{S}$ is called the complex scattering matrix. It contains the scattering properties of the particle and can be written as

$$\mathbf{S} = \begin{pmatrix} A_{11} & A_{12} \\ A_{21} & A_{22} \end{pmatrix} \tag{3.42}$$

For spherical drops, the complex scattering matrix is diagonal and the elements A_{12} and A_{21} are zero [18]. For reflection at the drop surface, the reflected electric field for parallel and perpendicular polarization is written as

$$\begin{pmatrix} \mathbf{E}_{r||} \\ \mathbf{E}_{r\perp} \end{pmatrix} = \frac{\exp[i \cdot k \cdot (R-z)]}{-i \cdot k \cdot R} \cdot \begin{pmatrix} r_p & 0 \\ 0 & r_s \end{pmatrix} \cdot \begin{pmatrix} \mathbf{E}_{i||} \\ \mathbf{E}_{i\perp} \end{pmatrix} \tag{3.43}$$

in which r_p and r_s are the Fresnel coefficients for reflection. In a similar manner, for the transmission, the transmitted electric field is given by

$$\begin{pmatrix} \mathbf{E}_{t||} \\ \mathbf{E}_{t\perp} \end{pmatrix} = \frac{\exp[i \cdot k \cdot (R-z)]}{-i \cdot k \cdot R} \cdot \begin{pmatrix} t_p & 0 \\ 0 & t_s \end{pmatrix} \cdot \begin{pmatrix} \mathbf{E}_{i||} \\ \mathbf{E}_{i\perp} \end{pmatrix} \tag{3.44}$$

in which t_p and t_s are the Fresnel coefficients for transmission. When total internal reflection occurs, because the phase shift is no longer 0 or π, the elements of the $\mathbf{S}$ can have imaginary parts [4]. Instead of using the complex scattering matrix $\mathbf{S}$, the scattering process is described with the real Mueller matrix. In the case of spherical drops, only 6 elements in the Mueller matrix are independent and can be written as

$$\mathbf{M} = \begin{pmatrix} S_{11} & S_{12} & 0 & 0 \\ S_{12} & S_{22} & 0 & 0 \\ 0 & 0 & S_{33} & S_{34} \\ 0 & 0 & -S_{34} & S_{44} \end{pmatrix} \tag{3.45}$$

With the solutions from the scattering equations of reflection and transmission Eqns. (3.44) and (3.45), the elements of the Mueller matrix are formulated as [5]

$$S_{11} = \frac{1}{2} \cdot (|A_{11}|^2 + |A_{22}|^2 + |A_{21}|^2 + |A_{12}|^2) \tag{3.46}$$

$$S_{12} = \frac{1}{2} \cdot (|A_{11}|^2 - |A_{22}|^2 + |A_{21}|^2 - |A_{12}|^2) \tag{3.47}$$

$$S_{22} = \frac{1}{2} \cdot (|A_{11}|^2 + |A_{22}|^2 - |A_{21}|^2 - |A_{12}|^2) \tag{3.48}$$

$$S_{33} = Re(A_{11}^* \cdot A_{22} + A_{12} \cdot A_{21}^*) \tag{3.49}$$

$$S_{34} = Im(A_{11} \cdot A_{22}^* + A_{21} \cdot A_{12}^*) \tag{3.50}$$

$$S_{44} = Re(A_{11}^* \cdot A_{22} - A_{12} \cdot A_{21}^*) \tag{3.51}$$

This leads to the reflection and the transmission Mueller matrix at the two dielectric interfaces

$$\mathbf{R} = \begin{pmatrix} \frac{r_p^2+r_s^2}{2} & \frac{r_p^2-r_s^2}{2} & 0 & 0 \\ \frac{r_p^2-r_s^2}{2} & \frac{r_p^2+r_s^2}{2} & 0 & 0 \\ 0 & 0 & Re(r_p^* \cdot r_s) & Im(r_p \cdot r_s^*) \\ 0 & 0 & -Im(r_p \cdot r_s^*) & Re(r_p^* \cdot r_s) \end{pmatrix} \tag{3.52}$$

$$\mathbf{T} = \begin{pmatrix} \frac{t_p^2+t_s^2}{2} & \frac{t_p^2-t_s^2}{2} & 0 & 0 \\ \frac{t_p^2-t_s^2}{2} & \frac{t_p^2+t_s^2}{2} & 0 & 0 \\ 0 & 0 & Re(t_p^* \cdot t_s) & Im(t_p \cdot t_s^*) \\ 0 & 0 & -Im(t_p \cdot t_s^*) & Re(t_p^* \cdot t_s) \end{pmatrix} \tag{3.53}$$

R and **T** are the Mueller matrices for the reflection and transmission at the drop surface respectively. For the case of a light ray transmitted from an optically dilute medium to an optically denser medium, the Fresnel coefficients are real and given by [14]

$$r_p = \frac{tan(\theta_i - \theta_t)}{tan(\theta_i + \theta_t)} \tag{3.54}$$

$$r_s = -\frac{sin(\theta_i - \theta_t)}{sin(\theta_i + \theta_t)} \tag{3.55}$$

$$t_p = \frac{2sin\theta_t cos\theta_i}{sin(\theta_i + \theta_t)cos(\theta_i - \theta_t)} \tag{3.56}$$

$$t_s = \frac{2sin\theta_t cos\theta_i}{sin(\theta_i + \theta_t)} \tag{3.57}$$

For this case, the elements S_{34} and S_{43} are zero. For the case of a light ray transmitted from an optically denser medium to an optically less dense medium, the Fresnel coefficients are given by Eqns. (3.58) and (3.59). When the incident angle θ_i is larger than the critical angle θ_c, total internal reflection occurs. Due to the phase shift of the reflected and transmitted electric field [69] [53], which can take values other than 0 or π, the Fresnel coefficients will be complex [20]

$$r_p = \frac{cos\theta_i - i \cdot m \cdot \sqrt{m^2 sin^2\theta_i - 1}}{cos\theta_i + i \cdot m \cdot \sqrt{m^2 sin^2\theta_i - 1}} \tag{3.58}$$

$$r_s = \frac{mcos\theta_i - i\sqrt{m^2 sin^2\theta_i - 1}}{mcos\theta_i + i\sqrt{m^2 sin^2\theta_i - 1}} \tag{3.59}$$

in which i is the imaginary number, $m = n_t/n_i$, and n_t and n_i are the refractive indexes of the optical denser medium and the optical rarer medium respectively. When the incident angle θ_i is smaller than the critical angle θ_c, r_p and r_s are still real numbers. Hence, the elements S_{34} and S_{43} are zero; however, when the incident angle θ_i is larger than the critical angle θ_c, total internal reflection occurs and r_p and r_s become complex numbers and the elements S_{34} and S_{43} are no longer zero.

Light ray intersects with suspended colloidal particles

For the scattering within the drop, a random walk model is utilized to predict the light ray path [49]. The procedure used follows that described by the flow chart given in Fig. (3.19), which is similar to the procedures for the Monte Carlo simulation of the light transport in scattering medium described in [46].

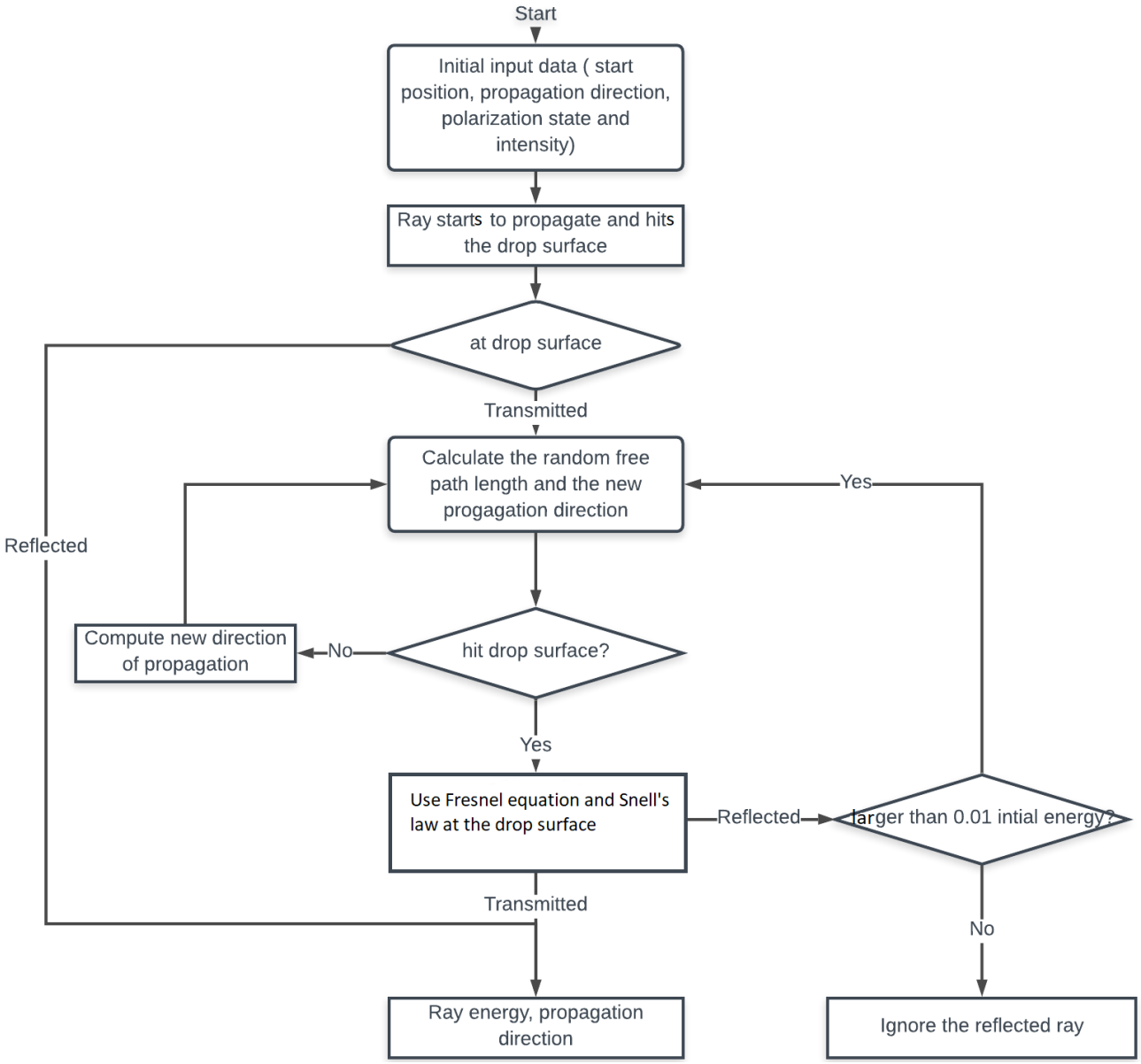

Figure 3.19: Flow chart for using the polarized Monte-Carlo ray-tracing method to simulate the light scattering of the colloidal drop.

The essential task is to generate the polar deflection angle θ and azimuthal angle ϕ to yield the new propagation direction of the light ray after the scattering event between the light ray and the inclusions within the colloidal drop. The conventional way for the angle sampling is to use the Henyey-Greenstein phase function (HG phase function) as the probability density function for the sampling of the polar deflection angle θ; and the sampling for the azimuthal angle ϕ is treated as

isotropic. The HG phase function is written as

$$P_{HG}(\theta) = \frac{1}{4\pi}(1-g^2)(1+g^2-2g\cos\theta)^{-\frac{3}{2}} \tag{3.60}$$

in which, g is the asymmetric factor and given in Eq. (3.61). The integral of the $P_{HG}(\theta)$ over 4π steradians is unity. For the Monte Carlo simulation, when the scatter is spherical, g is usually computed using the Lorenz-Mie theory [59]. In the current study the asymmetric factor is computed using the software MiePlot [25].

$$g = \iint_S p(\theta)\cdot\cos\theta d^2\Omega \tag{3.61}$$

The HG function could not be used directly for the angle sampling. For the Monte Carlo simulations its integral form is required to obtain the cumulative distribution function for θ, which is written as

$$\cos\theta = \begin{cases} \frac{1}{2g}[1+g^2-(\frac{1-g^2}{1-g+2g\xi})^2], & if\ g\ \neq\ 0 \\ 2\xi-1, & if\ g\ =\ 0 \end{cases} \tag{3.62}$$

in which ξ is a random number that is uniformly distributed between 0 and 1. However, using the HG phase function to predict the new scattering direction is very approximate, as the scattering pattern of the particle is related to the polarization state of the incident beam; and for using the HG phase function, the polarization state of the incident beam is not considered. To make the simulation more precise the Lorenz-Mie phase function is used. The scattered intensity by an isotropic sphere is a function of θ, ϕ and the polarization state. Using Eq. (3.39), the scattered intensity can be expressed as

$$I_{sca}(\theta,\phi) = S_{11}\cdot I_i + S_{12}\cdot(\cos(2\phi)\cdot Q_i - \sin(2\phi)\cdot U_i) \tag{3.63}$$

As evident from this equation, for polarized beams the scattered intensity exhibits a bivariate dependence on the angles θ and ϕ; for the non-polarized beam, whose Stokes vector is $[1\ 0\ 0\ 0]^T$, the scattered intensity is then only a function of θ. For this case, the Henyey-Greenstein phase function can be used to predict the angle θ and the sampling of angle ϕ can be treated as being isotropic.

Fig. 3.20 shows the three-dimensional scattered intensity from a colloidal particle, which is illuminated by plane waves exhibiting vertical linear polarization (s) and right-hand circular polarization respectively. The intensity is plotted with color on a logarithmic scale. The incident wave impinges on the particle in the positive z direction. As the figure shows, the polarization state has a detectable effect on the scattered phase function of the particle, primarily in the backward direction. This influence of polarization on the time-shift signals can be noticed seen Figs. 3.21 and 3.22. In Fig. 3.21 a comparison of the simulated time-shift signals when the polarization state of the incident beam are perpendicular and parallel polarized. It indicates that for a pure water drop, the polarization state of the incident beam has an significant effect on the signal amplitude of the second-order refraction scattering. In Fig. 3.22 the simulated time-shift signals from a colloidal drop, when the laser beam is perpendicular and parallel polarized are shown. The time-shift signals generated by the scattering from the inclusions within the colloidal drop have been illustrated in Fig. 3.22 as well. The polarization state could also affect the scattering from the inclusions within the drop.

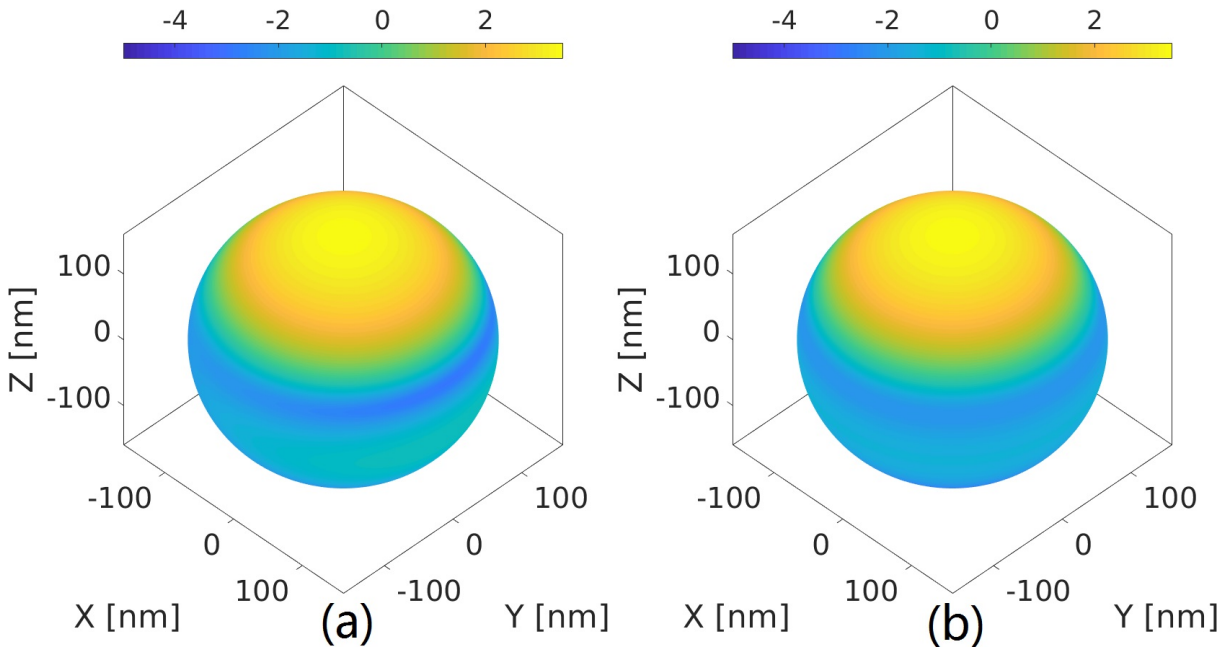

Figure 3.20: Comparison of the scattering phase functions of a colloidal particle illuminated by a plane wave for different polarization. The scattered intensity is expressed by color on a logarithmic scale. a): the incident plane wave is linearly polarized with the Stokes vector $[1 \ -1 \ 0 \ 0]^T$; b): the incident plane wave is circularly polarized with the Stokes vector $[1 \ 0 \ 0 \ 1]^T$. (Refractive index of medium 1.3431, refractive index of particle 1.6268, size of embedded particles is 320 nm, wavelength of the plane wave 405 nm). Reprinted with permission from [29] © The Optical Society.

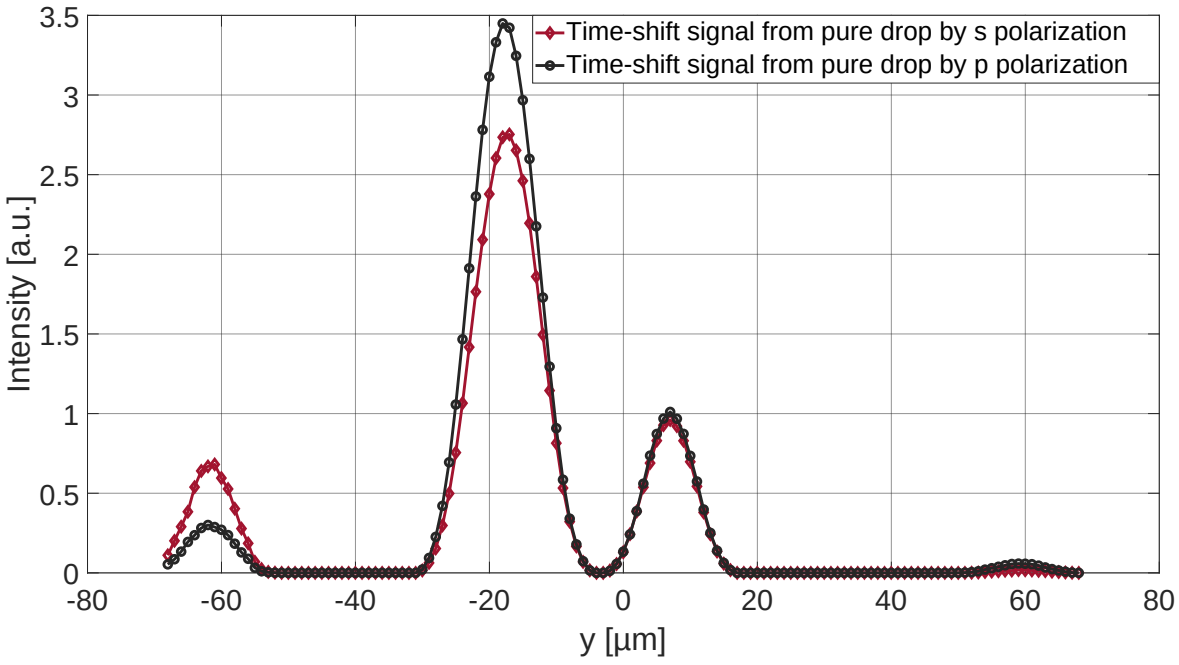

Figure 3.21: Compare simulated time-shift signals from pure water drop when the polarization states of the laser beam are perpendicular and parallel polarized.

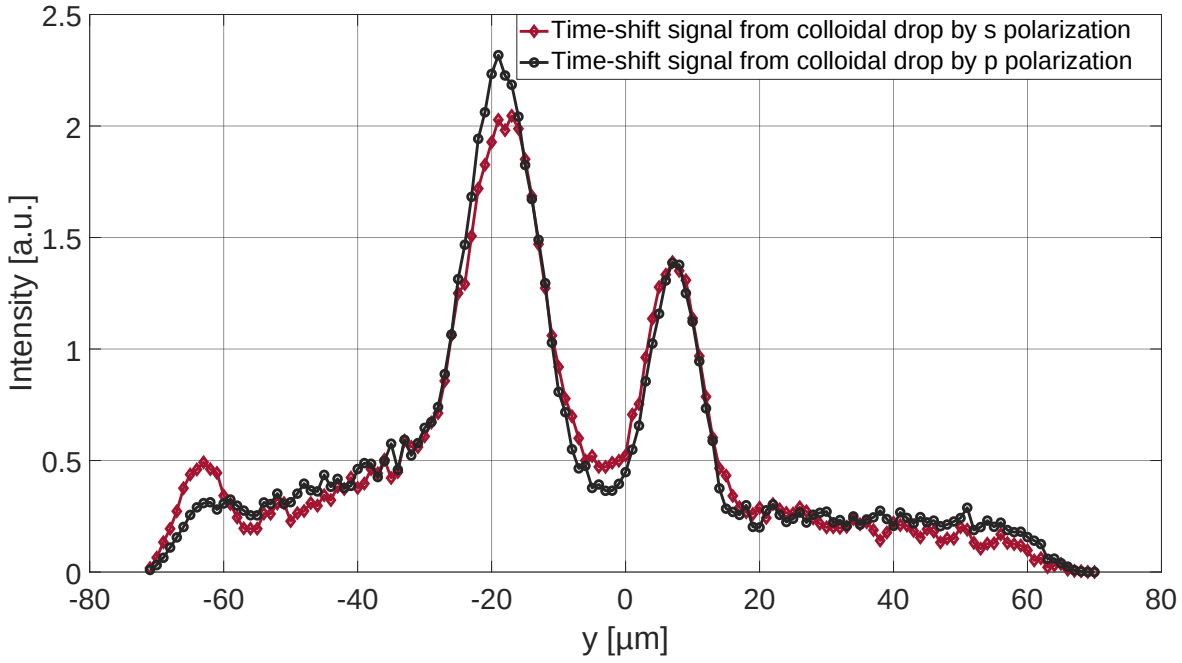

Figure 3.22: Comparison of simulated time-shift signals from a colloidal water drop when the polarization state of the laser beam is perpendicular and parallel polarized. The time-shift signals generated by the scattering of the inclusions within the colloidal drop are also shown. Reprinted with permission from [29] © The Optical Society.

The left picture in Fig. 3.20 shows the scattering diagram over the solid angle 4π when the particle is illuminated by a plane wave with the polarization state $[1-1\ 0\ 0]^T$. This is used to generate the probability density function $\rho(\theta,\phi)$ for sampling θ and ϕ, whose integration over the solid angle 4π should be unity. Therefore, when a large number of light rays with the polarization state $[1-1\ 0\ 0]^T$ are incident on the particle, the scattered light ray density in each direction specified by angle θ and ϕ should be proportional to the scattered intensity $I_{sca}(\theta,\phi)$. Since θ and ϕ are not separable, and the accumulative method cannot be used for sampling, the rejection sampling method is used [46] [19] [24]. With Eq. (3.63), the scattered intensity over the solid angle 4π can be expressed as [24]

$$I_{sca} = \int_{\theta=0}^{\pi}\int_{\phi=0}^{2\pi} I_{sca}(\theta,\phi)\sin\theta d\theta d\phi \tag{3.64}$$

Therefore, the probability density function that a photon scatters in the direction $(\theta,\phi,)$ can be expressed as

$$f(\theta,\phi) = \frac{I_{sca}(\theta,\phi)}{I_{sca}} \tag{3.65}$$

For using the rejection sampling method, the target scattering direction (θ,ϕ) has a probability density function $f(\theta,\phi)$. A probability distribution $G(\theta,\phi)$ needs to be found, corresponding to the probability density function $g(\theta,\phi)$, for which we already have an efficient generation algorithm. The ratio $f(\theta,\phi)/g(\theta,\phi)$ should be bounded by a constant C, and C should be as close to 1 as possible to save computational time. For embedded nanoparticles with diameter 320nm and a refractive index of 1.6268, the maximum scattered intensity occurs in the forward direction $(\theta=0)$ [25]. Therefore, the probability distribution G can be constructed by utilizing the maximum scattered intensity at

($\theta = 0$), and its $g(\theta, \phi)$ can be expressed as

$$g(\theta, \phi) = \frac{I_{sca}(\theta = 0, \phi)}{I_{sca}} \tag{3.66}$$

For the probability density function $g(\theta, \phi)$ both of the scattering angles θ and ϕ are uniformly distributed within $[0, \pi]$ and $[0, 2\pi]$. The angle sampling can be achieved by using the following equations

$$\theta_0 = \pi\xi_1 \tag{3.67}$$

$$\phi_0 = 2\pi\xi_2 \tag{3.68}$$

$$F = S_{11}(\theta = 0)I_i + S_{12}(\theta = 0)(\cos(2\phi_0)Q_i - \sin(2\phi_0)U_i) \tag{3.69}$$

$$I_{sca} = S_{11}(\theta_0)I_i + S_{12}(\theta_0)(\cos(2\phi_0)Q_i - \sin(2\phi_0)U_i) \tag{3.70}$$

$$I_{com} = \xi_3 F \tag{3.71}$$

Strictly speaking, a standard Mie calculation is insufficient in the context of an absorbing host medium such as water. The corresponding theory for light scattering by a spherical particle in an absorbing host medium is given in Mishchenko et al. [39]. However, to consider an absorbing host medium is out of the scope of the present study. For sampling of θ, a lookup table having a resolution of 0.001° was created for the Mueller matrix elements S_{11} and S_{12}, in order to speed up the computation. ξ_1,ξ_2 and ξ_3 are random numbers. If I_{com} is smaller than $I_{sca}(\theta_0, \phi_0)$, then the (θ_0, ϕ_0) values are accepted, otherwise these steps need to be repeated until the condition is met that $I_{com} < I_{sca}(\theta_0, \phi_0)$. After the generation of θ and ϕ the Stokes vector needs to be updated with Eq. (3.72), to modify the probability of the light ray scattering in the next direction.

$$\begin{pmatrix} I_{sca} \\ Q_{sca} \\ U_{sca} \\ V_{sca} \end{pmatrix} = \begin{pmatrix} 1 & S_{12}/S_{11} & 0 & 0 \\ S_{12}/S_{11} & S_{22}/S_{11} & 0 & 0 \\ 0 & 0 & S_{33}/S_{11} & S_{34}/S_{11} \\ 0 & 0 & -S_{34}/S_{11} & S_{44}/S_{11} \end{pmatrix} \cdot \mathbf{R}(\phi) \cdot \begin{pmatrix} I_i \\ Q_i \\ U_i \\ V_i \end{pmatrix} \tag{3.72}$$

After the intersection with the colloidal particle, the local reference frame needs to be updated from $[e_x^0 \;\; e_y^0 \;\; e_z^0]^T$ to $[e_x^1 \;\; e_y^1 \;\; e_z^1]^T$, i.e.

$$\begin{pmatrix} e_x^1 \\ e_y^1 \\ e_z^1 \end{pmatrix} = \begin{pmatrix} \cos\theta_0 & 0 & -\sin\theta_0 \\ 0 & 1 & 0 \\ \sin\theta_0 & 0 & \cos\theta_0 \end{pmatrix} \begin{pmatrix} \cos\theta_0 & \sin\theta_0 & 0 \\ -\sin\theta_0 & \cos\theta_0 & 0 \\ 0 & 0 & 1 \end{pmatrix} \begin{pmatrix} e_x^0 \\ e_y^0 \\ e_z^0 \end{pmatrix} \tag{3.73}$$

Following a scattering event from an embedded colloidal particle, the intensity of any ray reaching the detector decreases significantly. After two or more internal scattering events inside the drop, the intensity again decreases strongly. Therefore, a threshold intensity level is set, below which the ray tracing is terminated.

Validation and comparison between the simulation and experiment results

First, the generation of the new scattering direction of the light ray was validated, since this is one of the most essential parts of the Monte Carlo code. To validate this step, a scattering diagram for the particle is computed with the rejection sampling method and compared to results given by the Lorenz-Mie theory. Thirty billion light rays were launched for the computation of the scattering diagram. With the Mueller matrix computed from the Software MiePlot [25] and Eq. (3.63), the bivariate scattering diagram is plotted in Fig. 3.23 (a), when the incident plane wave is linearly polarized with the Stokes vector $[1 \quad -1 \quad 0 \quad 0]^T$. Then the scattering diagram is generated with the rejection sampling method for comparison, as shown in Fig. 3.23(b). The agreement can be seen to be very good.

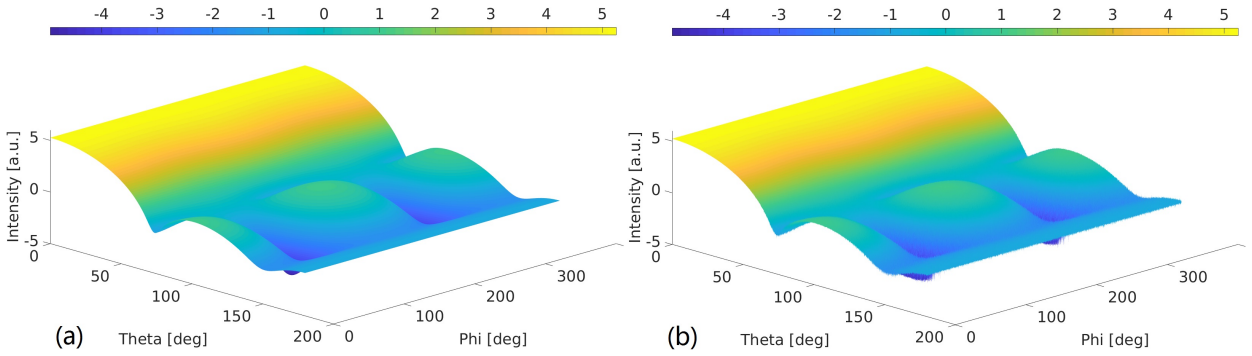

Figure 3.23: Bivariate scattering diagram calculated with a) the Mueller matrix computed from the MiePlot Software [25] and b) the rejection sampling method using 30 billion light rays. The intensity in Z-axis is plotted on a logarithmic scale. The incident plane wave is linearly polarized with the Stokes vector $[1 \quad -1 \quad 0 \quad 0]^T$. (refractive index of surrounding medium 1.3431, refractive index of colloidal particle 1.6268, size of nanoparticle 320 nm, wavelength of the plane wave 405 nm). Reprinted with permission from [29] © The Optical Society.

To underline this good agreement the difference between the two scattering diagrams from the Lorenz-Mie theory and the rejection sampling method is shown in Fig. 3.24. This difference is normalized with the local value; hence, given as percent deviation. The maximum normalized deviation occurs where the absolute intensity becomes very low (due to the normalization), but for the most part the deviation remains extremely low. However the deviation can be reduced to any arbitrary level by increasing the number of the incident light rays. For a detector located in the direction of lower scattered intensity, more incident light rays will needed to obtain a converged signal.

3.3 Discrete dipole approximation method for computation the light scattering of colloidal drop

Compared to the Monte Carlo ray-tracing method, the discrete dipole approximation (DDA) method is a more accurate method to compute the electromagnetic scattering of matter. To study the light scattering properties of a colloidal drop, the DDA method has also been used. The goal is to check how sensitive the scattering properties are against the change of the colloidal inclusions. The colloidal drop has been treated as a large number of polarized dipoles; the position and the refractive index of each dipole are specified before computation. As the computation time using the DDA method increases dramatically when the size parameter of the drops is over 100 or the

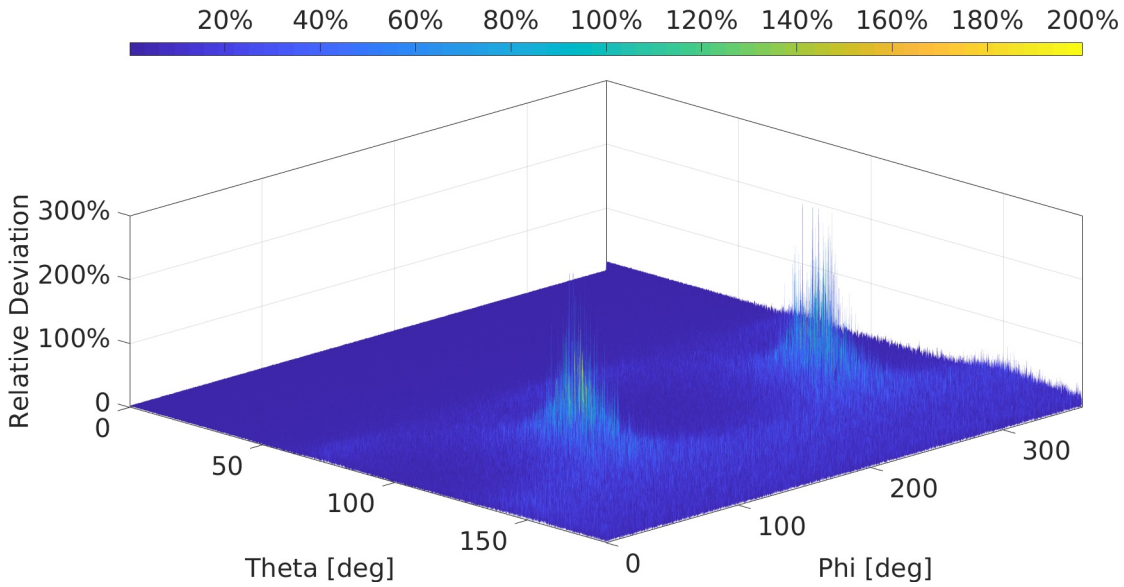

Figure 3.24: Relative deviation between the scattering diagrams computed from the Lorenz-Mie theory and the rejection sampling method using 30 billion light rays. Reprinted with permission from [29] © The Optical Society.

refractive index of the inclusions increases, only computations were performed for drops, whose size parameter remained under 100. In the following computations, the size of the host drop is kept as 10 μm.

Three sets of computations were implemented by varying the size of inclusions, the refractive index of inclusions and the volume fraction of the inclusions. These computations were made by using the high performance computing center "Lichtenberg-Hochleistungsrechner" of TU Darmstadt. It took about eight hours with 500 cores to finish a single computation. In the first set of computations, the size of the inclusions is varying from 50 nm to 110 nm by keeping the drop size, the volume fraction of the inclusion and the refractive index of the inclusion constant. The parameters for computation are listed in Tab. (3.1). The results are shown in Fig. 3.25, in which the 16 elements of the Mueller matrix are plotted from 0° to 180° individually in each sub-figure, in order to present what effect the change of the inclusion size brings to each Mueller matrix element. The computation results, when the sizes of the inclusion are 0 μm, 50 μm, 70 μm, 90 μm and 110 μm, are plotted with blue, red, yellow, purple and green respectively. As the figure indicates, by changing the size of the inclusion, the Mueller matrix elements do not change significantly.

	D	f	d	Refractive index inclusion
1	10 μm	0.05	0.05 μm	1.5
2	10 μm	0.05	0.07 μm	1.5
3	10 μm	0.05	0.09 μm	1.5
4	10 μm	0.05	0.11 μm	1.5
incident plane wave with $\lambda = 0.405$ μm				
uniform distribution of granules				

Table 3.1: Condition for DDA simulation for different size of inclusion

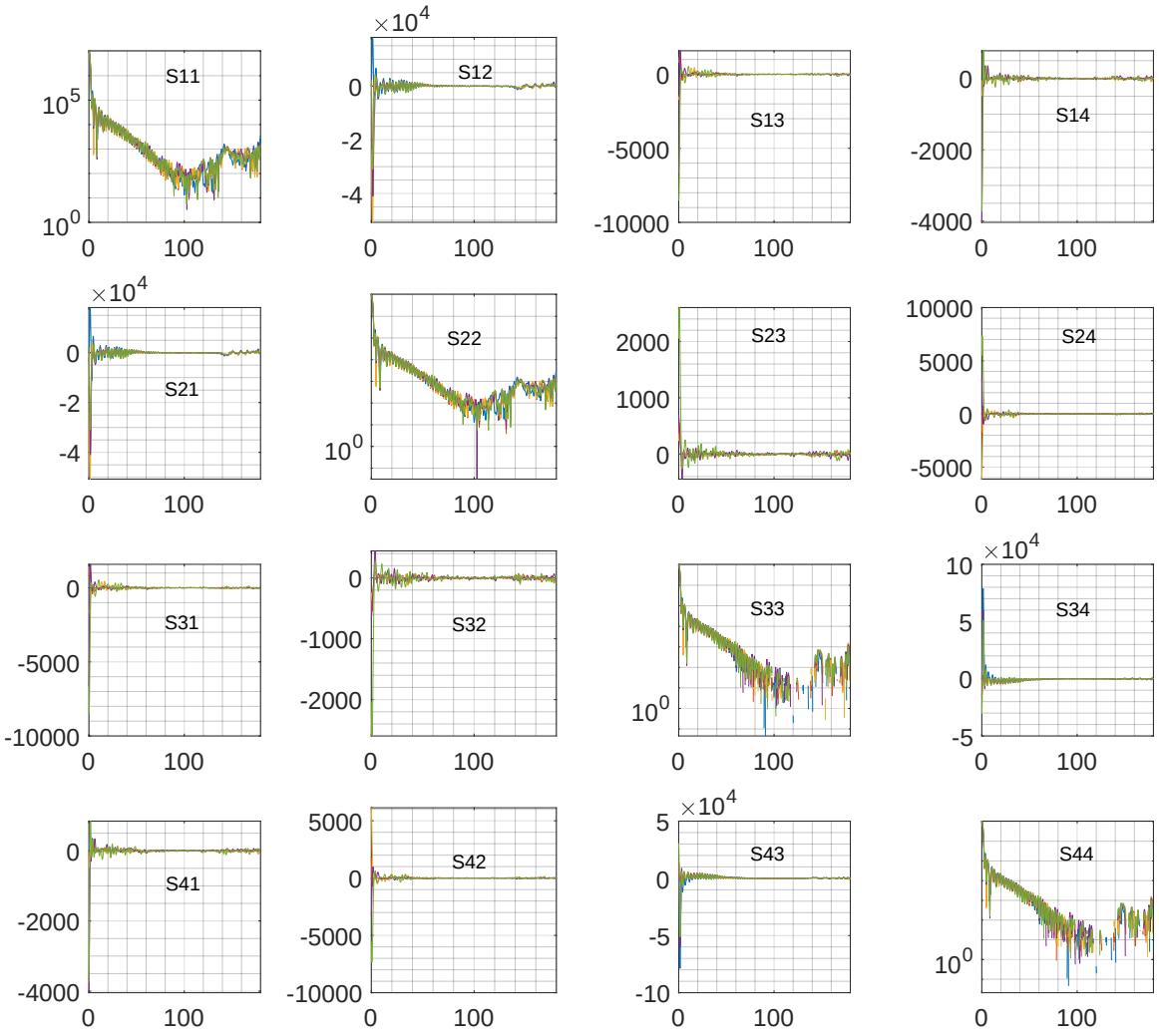

Figure 3.25: Mueller matrix comparison for different size of inclusion by keeping volume fraction of the inclusions as constant. The color blue, red, yellow, purple and green represents the results, when the inclusion sizes are 0 μm, 50 μm, 70 μm, 90 μm, 110 μm respectively. (drop size : 100 μm, drop refractive index: 1.3431; nanoparticle refractive index: 1.6268; wavelength: 405 nm)

For the second set of computations, the volume fraction of the inclusions varies from 1% to 9%. The parameters for individual computations are listed in Tab. (3.2). The computation results are illustrated in Fig. 3.26, in which the 16 Mueller matrix elements are plotted from 0° to 180° for different volume fractions of the inclusions.

	D	f	d	Refractive index inclusion
1	10 μm	0.01	0.05 μm	1.5
3	10 μm	0.05	0.05 μm	1.5
4	10 μm	0.09	0.05 μm	1.5
incident plane wave with $\lambda = 0.405$ μm				
uniform distribution of inclusions				

Table 3.2: Conditions for DDA simulation for different volume fraction of inclusion

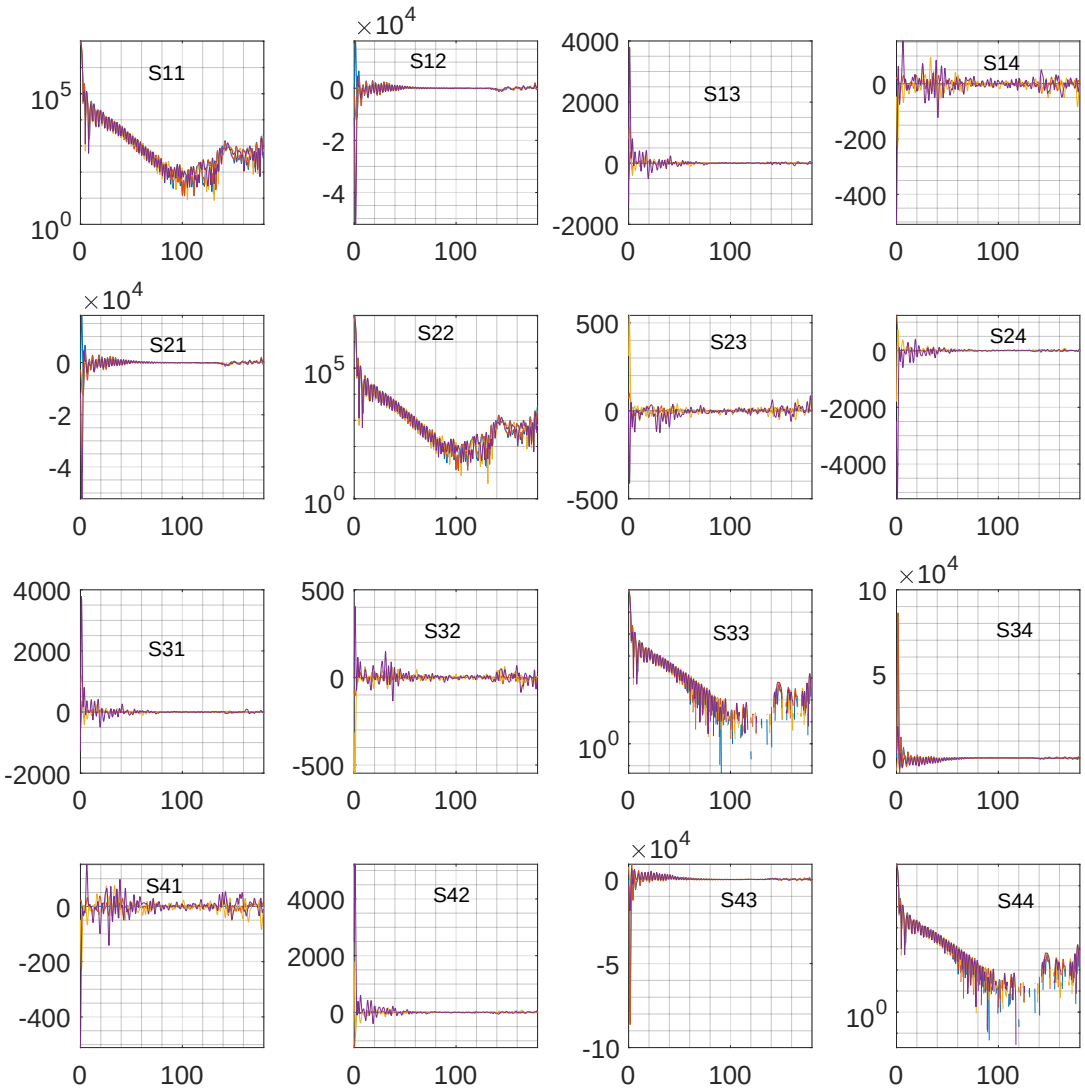

Figure 3.26: Mueller matrix comparison for different volume fraction of inclusions.(drop size : 100 μm, drop refractive index: 1.3431; nanoparticle size: 50 nm; wavelength: 405 nm)

For the third set of computations, the refractive indices of the inclusions vary from 1.1 to 1.9 while keeping the size and the refractive index of the host drop and the volume fraction of the inclusion as constant.

	D	f	d	Refractive index inclusion
1	10 μm	0.05	0.05 μm	1.1
3	10 μm	0.05	0.05 μm	1.5
4	10 μm	0.05	0.05 μm	1.9
incident plane wave with $\lambda = 0.405$ μm				
uniform distribution of inclusions				

Table 3.3: Conditions for DDA simulation for different refractive index of inclusion

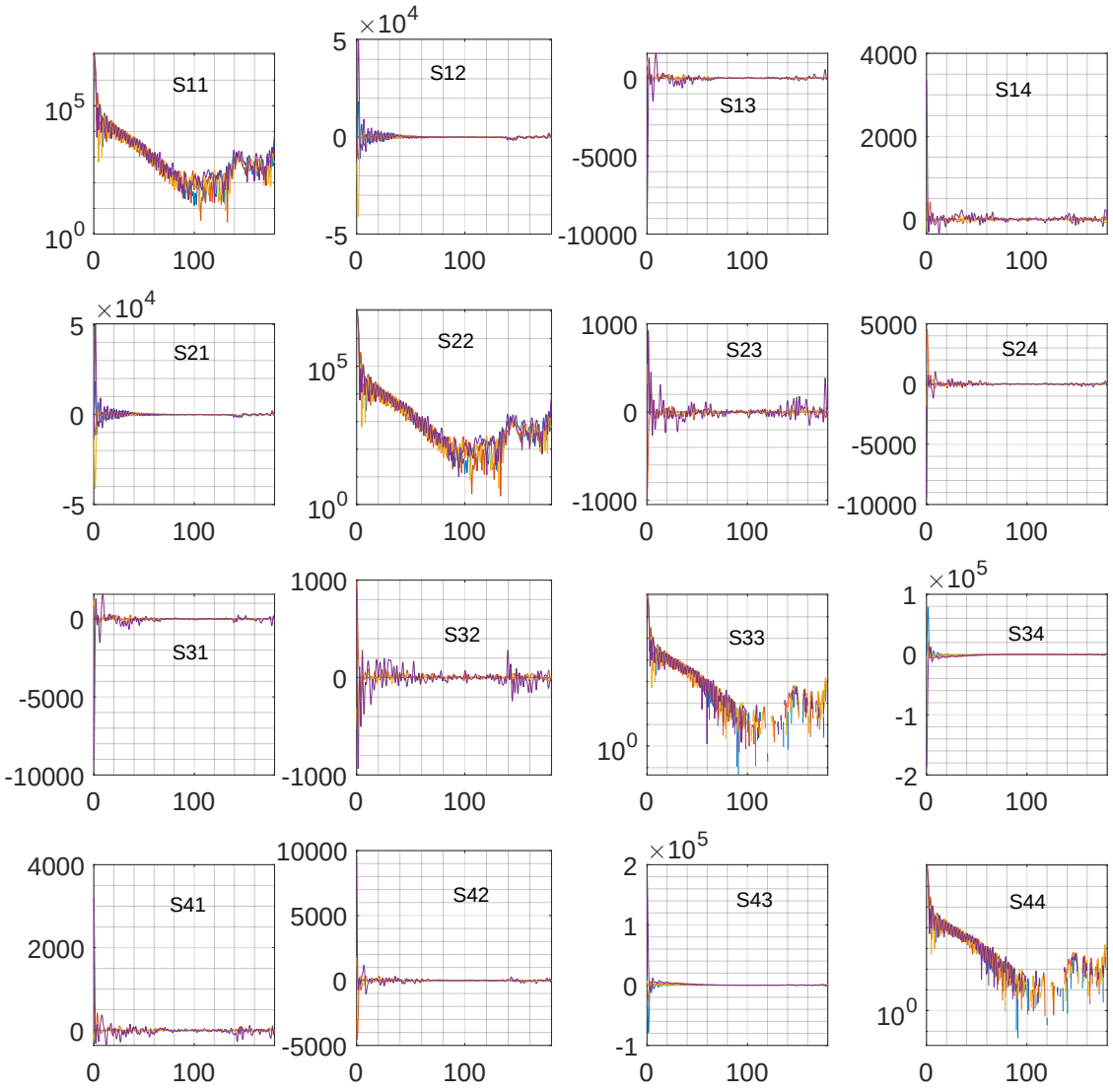

Figure 3.27: Mueller matrix comparison for different refractive indices of inclusion.(drop size : 100 μm, drop refractive index: 1.3431; nanoparticle size: 50 nm; wavelength: 405 nm)

As these computation results show, when the refractive indices of the inclusion and the host drop are close to one another, the scattering properties of the colloidal drop do not change significantly.

As the results from the three sets of computations indicate, when the refractive index of the drop and the refractive index of the inclusion are close to one other, by changing the size or the volume fraction of the inclusions, the scattering properties of the colloidal drop will not be strongly affected.

4 Simulation of time-shift signals from complex particles

4.1 Measurement principle of the time-shift technique

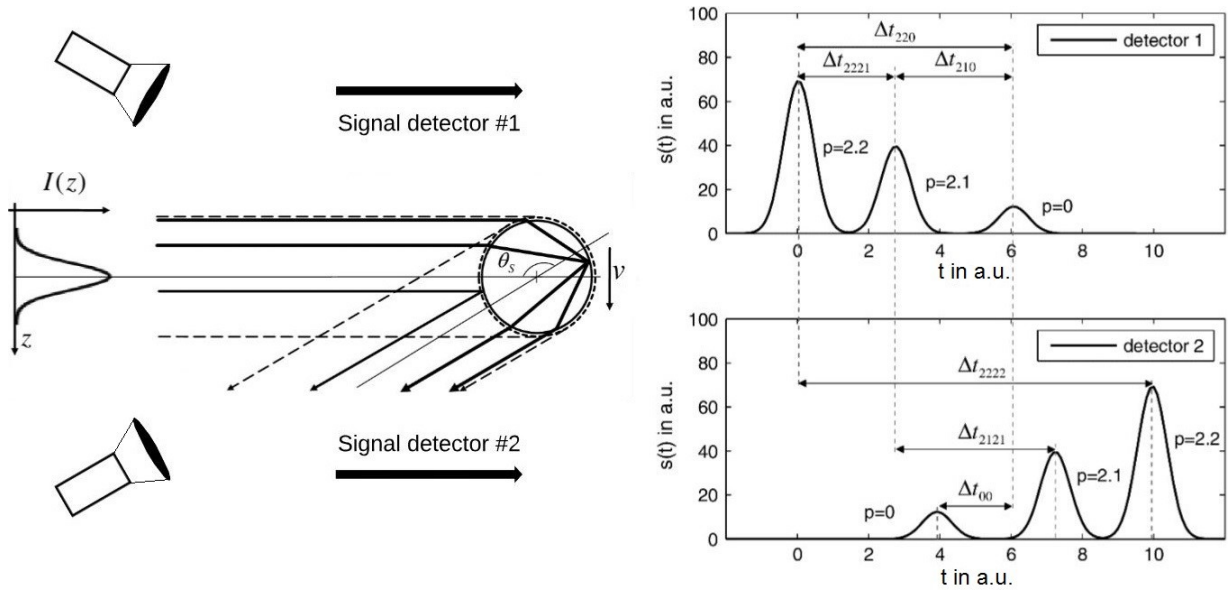

Figure 4.1: Time-shift measurement principle. Permission granted from the publisher Elsevier.

The time-shift technique, which is also known as the pulsed-displacement technique [15], [32], is a method to measure size, velocity, and relative refractive index (m) of spherical particles. As Fig. 4.1 illustrates, a detector placed in the backscatter direction (e.g. 150°) will register a time dependent signal comprising several peaks, corresponding to the different scattering orders as a transparent drop passes through the shaped beam. Details about the measurement principle and optical design can be found in [51]; however, an important distinguishing factor for the time-shift technique is that the beam has a focused waist is much smaller than the size of the drop to be measured. This insures that the different scattering orders appearing in the detector signal will be separated in time.

To compute the signal arising from the passage of a drop through the focused beam of a time-shift instrument, first a drop position is specified and the light scattered onto a defined detector (position and aperture size) is computed. With a given velocity, the drop is then displaced in the flight direction by a time step of Δt and the computation is repeated. The intensity collected on the detector of diameter d for each drop position is converted into a time signal using the prescribed drop velocity v_z. To obtain the time-shift signal, the light scattering of all drop positions in which incident rays intersect with the drop need to be computed. The time-shift signal, illustrated in Fig. 4.1 for detectors placed on either side of the illuminated laser sheet, comprises three main peaks: one arising from reflected light (p = 0) and one each from the two modes of second-order refraction (p = 2.1, p = 2.2) [1]. The particle/drop size can be computed from the time-shift between the signal peaks; either peaks within one detector (e.g. Δt_{220}, Δt_{2221}, Δt_{210}) or between peaks in different detector signals (e.g. Δt_{2222}, Δt_{2121}). More details about the size and velocity

measurement are given in [51]. Due to the redundancy of size information in various time shifts between signal peaks, should parts of the signal be missing, e.g. if rays are blocked by an embedded particle, it may still be possible to estimate the drop size using the remaining signal peaks.

Laser beam description

The laser beam incident on the drop corresponds to that used by a time-shift instrument, for instance the SpraySpy instrument from AOM-Systems [50]. In this case, the laser beam has a beam waist of 1 mm in the X direction and approximately 10 μm in the Y direction (direction of particle movement), the Z direction being the direction of laser beam propagation. Such a non-circular Gaussian beam (light sheet) is used to improve the directional sensitivity of the instrument, as described in [51]. This non-circular Gaussian beam is treated as a large number of rays (N), each ray being defined by its starting point, propagation direction, and the initial amplitude of the electric field $\mathbf{E}_0$. Because the measurement volume of time-shift technique is in the Rayleigh range, the initial propagation direction is the same for all rays($\mathbf{k}_i$). The starting points of the rays are randomly distributed in space. This is similar to the approach used in [57] and experience confirms that convergence of the computed light scattering diagrams is achieved with much fewer rays than if a regular grid spacing is used for the ray starting points.

4.2 Mathematical expression of the time-shift signal for pure a drop

Incident regions for different signal modes of time-shift signal

For the intersection of a laser beam with a pure liquid drop, the drop can be treated as a sphere or spheroid. When considering the time-shift instrument, light only reaches the detector when the laser beam illuminates certain parts of the drop corresponding to the incident points of ray paths for the respective scattering order, e.g. reflected or second-order refractive light. The illuminated region on the drop when light of a given scattering order propagates into the instrument detector is called the "incident region". Since the detector of the time-shift instrument covers a solid angle, the incident region for each scattering order is finite.

The propagation direction of the incident ray in the particle coordinate system is expressed as $\mathbf{k}_i = [0\ \ 0\ \ 1]$, when the incident point is expressed with the coordinates (x, y, z). The unit normal vector of the detector used in this study is $\mathbf{n}_D = [0\ \ \sin 15^\circ\ \ -\cos 15^\circ]$, given in the particle coordinate system, being the same as the arrangement of the time-shift instrument. The detector covers an angle range of 11.6°; therefore, reflection rays that reach the detector surface should satisfy

$$\mathbf{n}_D \cdot \mathbf{n}_R >= \cos 5.8^\circ \tag{4.1}$$

The vector for the reflected ray is given by

$$\begin{aligned} \mathbf{n}_R &= \mathbf{k}_i - 2(\mathbf{k}_i \cdot \mathbf{n})\mathbf{n} \\ &= [-\frac{2xz}{R^2}\ \ -\frac{2yz}{R^2}\ \ \frac{R^2-2z^2}{R^2}] \end{aligned} \tag{4.2}$$

with

$$\mathbf{n} = [\frac{x}{R}\ \ \frac{y}{R}\ \ \frac{z}{R}] \tag{4.3}$$

Therefore, the incident angle can be computed as

$$\theta_i = \arccos\left(\mathbf{n} \cdot \mathbf{k}_i\right) \tag{4.4}$$

$$\theta_i = \arccos\frac{z}{R} = \arccos\frac{\sqrt{R^2 - x^2 - y^2}}{R} \tag{4.5}$$

The transmitted angle is calculated as

$$\theta_t = \arcsin\left(\frac{\sin\left(\arccos\frac{z}{R}\right)}{n_t}\right) = \arcsin\left(\frac{\sin\left(\arccos\frac{\sqrt{R^2-x^2-y^2}}{R}\right)}{n_t}\right) = \arcsin\left(\frac{\sqrt{x^2+y^2}}{R \times n_t}\right) \tag{4.6}$$

Then the incident region for the time-shift signal for reflection from the drop can be formulated as

$$2y \times \frac{\sqrt{R^2 - x^2 - y^2}}{R^2}\sin 15^\circ + \frac{R^2 - 2x^2 - 2y^2}{R^2}\cos 15^\circ >= \cos 5.8^\circ \tag{4.7}$$

in which R is the radius of the drop, x and y are the coordinates of the incident intersection points on the drop in the X axis direction and Y axis direction respectively. The incident region for the reflection on a spherical homogeneous water drop is illustrated as a red patch in Fig. 4.2 (a) and (b).

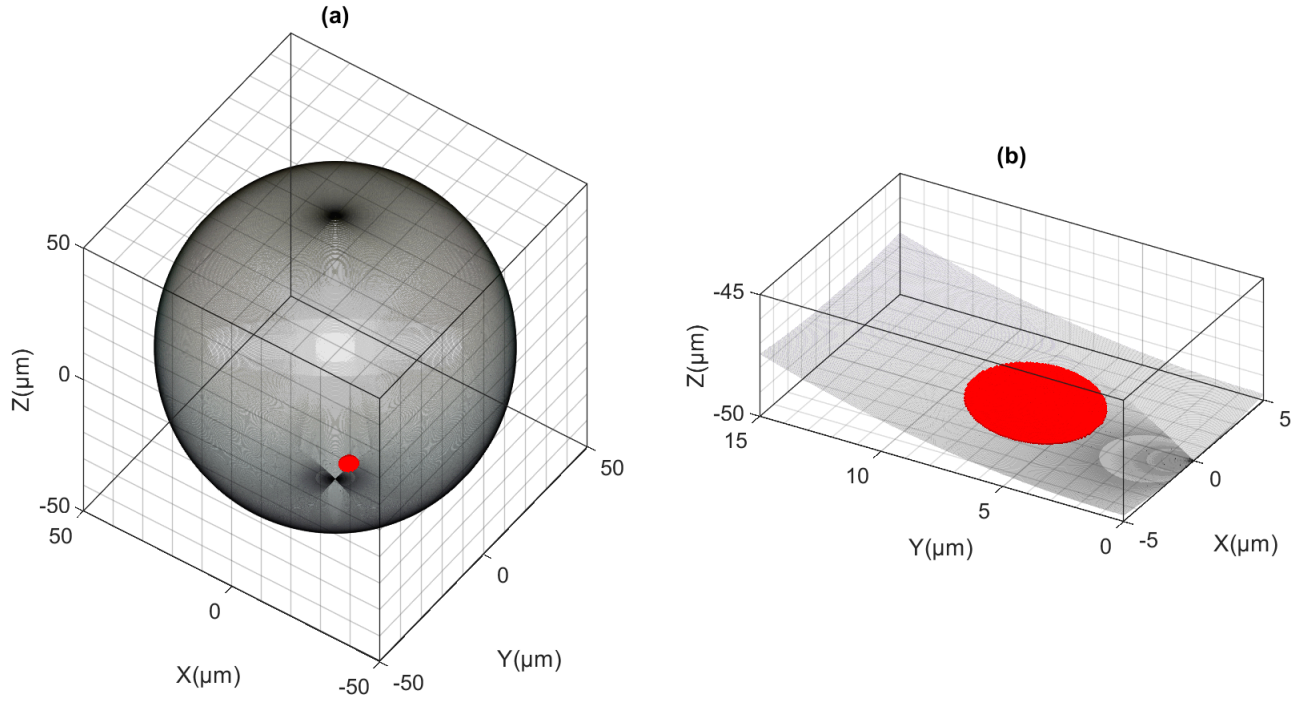

Figure 4.2: Incident region for reflection scattering on a spherical, homogeneous water drop. The region is marked with red color. (b) is an enlarged view for of the region.

At the incident intersection point, with the coordinate (x, y, z), the Fresnel coefficient for the reflection can be obtained by substitute the Eqs. (4.5) - (4.6) in Eqs. (3.54) - (3.59).

Fig. 4.3 illustrates the ray path for second-order scattering. As the figure shows, when the rotation direction is clockwise, the rotation angle of the second-order transmitted ray in the plane of incidence can be expressed as

$$\theta_T = \pi - 2\theta_i + 4\theta_t \tag{4.8}$$

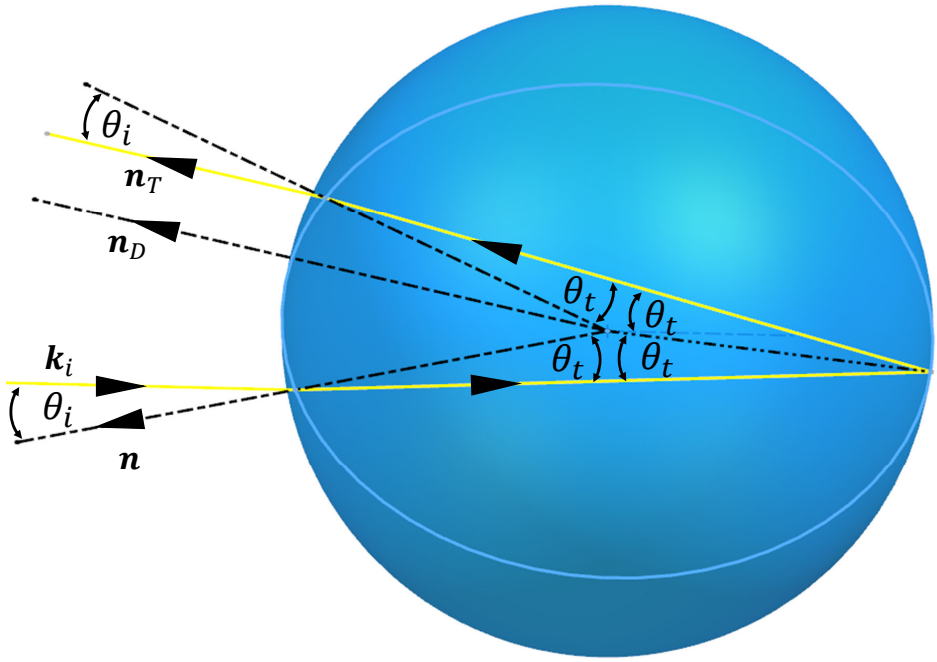

Figure 4.3: Direction change of second order transmitted ray

θ_T can be rewritten as

$$\theta_T = 2\arccos\left(\frac{-z}{R}\right) + \pi - 4\arcsin\frac{\sin\left(\arccos\left(\frac{-z}{R}\right)\right)}{n_t} \tag{4.9}$$

$$\theta_T = \pi - 2\arccos\left(\frac{\sqrt{R^2-x^2-y^2}}{R}\right) + 4\arcsin\frac{\sqrt{R^2-x^2-y^2}}{R\times n_t} \tag{4.10}$$

Therefore, the propagation direction of the second-order transmitted ray can be obtained after rotation of the incident ray by the angle θ_T within the scattering plane. The propagation direction can then be formulated by using Eq. (3.14) for rotation of a vector in three-dimensional space, the vector for the propagation direction of the outgoing ray for the second order becomes

$$\begin{aligned}\mathbf{n}_T &= \mathbf{k}_i\cos\theta_T + (\mathbf{D}_{RA}\times\mathbf{k}_i)\sin\theta_T + \mathbf{D}_{RA}(\mathbf{D}_{RA}\cdot\mathbf{k}_i)(1-\cos\theta_T)\\ &= [\frac{x}{\sqrt{(x^2+y^2)}}\sin\theta_T \quad \frac{y}{\sqrt{(x^2+y^2)}}\sin\theta_T \quad \cos\theta_T]\end{aligned} \tag{4.11}$$

in which $\mathbf{D}_{RA}$ is the vector for the rotation axis, which is given by the cross-product of two unit vectors $\mathbf{n}$ and $\mathbf{k}_i$ in the plane of rotation.

$$\begin{aligned}\mathbf{D}_{RA} &= \frac{\mathbf{k}_i\times\mathbf{n}}{|\mathbf{k}_i\times\mathbf{n}|}\\ &= [-\frac{y}{\sqrt{(x^2+y^2)}} \quad \frac{x}{\sqrt{(x^2+y^2)}} \quad 0]\end{aligned} \tag{4.12}$$

The incident region of the time-shift signal from second-order refraction scattering of the drop should satisfy

$$\mathbf{n}_D\cdot\mathbf{n}_T >= \cos 5.8^\circ \tag{4.13}$$

which can be rewritten as

$$\frac{y}{\sqrt{(x^2+y^2)}} \sin\theta_T \sin 15^\circ - \cos\theta_T \cos 15^\circ >= \cos 5.8^\circ \tag{4.14}$$

The incident region for the time-shift signal from second-order refraction scattering, which is marked in red, is illustrated in Fig. (4.4).

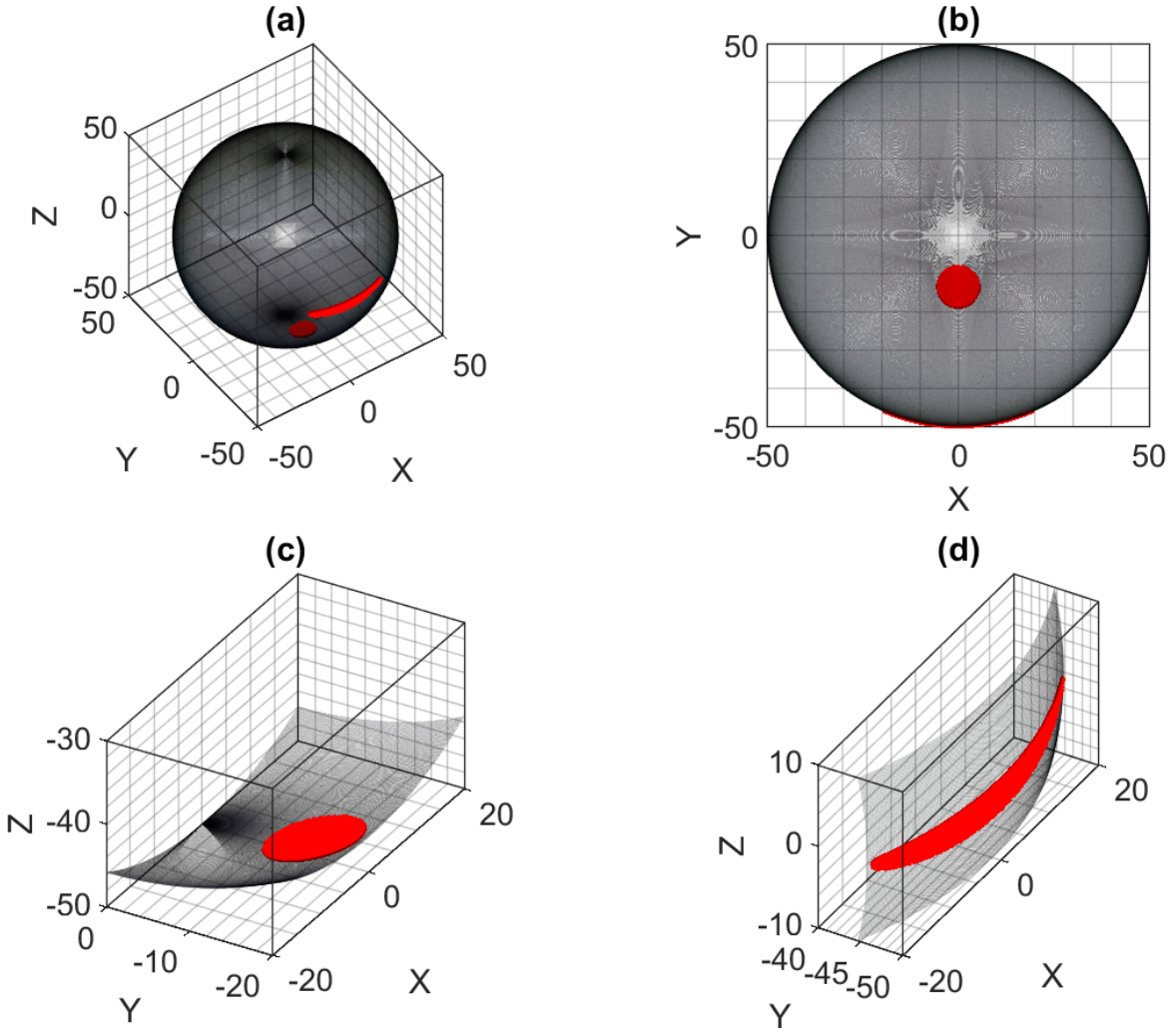

Figure 4.4: Incident region for second-order refraction scattering on a spherical homogeneous water drop. The region is marked in red . (diameter of drop = 100 μm, refractive index of drop: 1.3431.) (a) is the view of incident region in 3D; (b) is the view of (a) in the XY plane; (c) and (d) are enlarged views of the incident regions for the time-shift signal for second-order refraction scattering from the drop.

Compared with the incident region for time-shift signal from the reflective scattering, the incident region from the time-shift signal for second-order refraction scattering contains two parts, which correspond to the time-shift signal modes $p = 2.1$ and $p = 2.2$. In Fig. 4.5 is the comparison of the incident regions for the signal modes $p = 2.1$ and $p = 2.2$ for the refractive indices 1.3431 and 1.4. As the figure indicates, the area as well as the location of the incident regions are strongly affected by the refractive index of the drop.

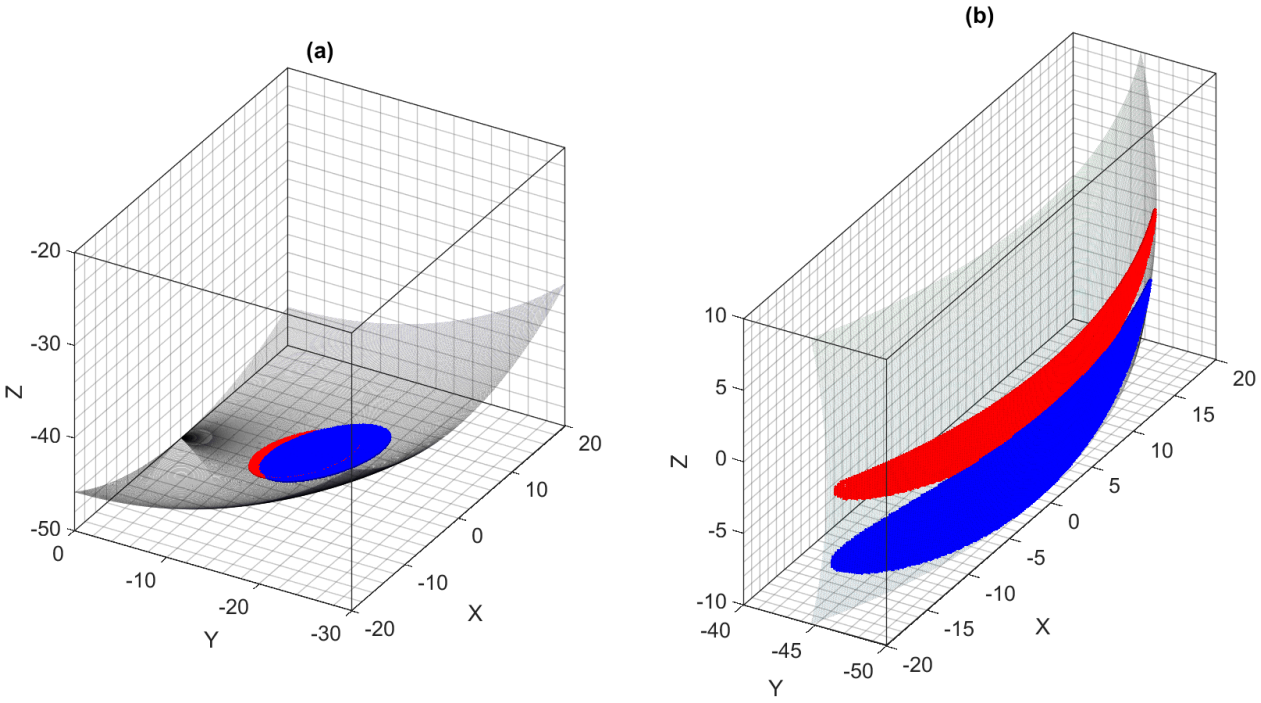

Figure 4.5: Compare incident region for second order refraction for different refractive indices.

Mathematical formulation of the time-shift signal

The time-shift signal is generated when the drop passes through the laser beam, as Fig. (4.1) illustrates. When using the drop center as the origin of the coordinate system, the coordinate of the beam center is expressed as $(x_s,\ y_s,\ z_s)$. The laser beam used in the time-shift instrument is a simple astigmatic beam, which has an elliptical beam profile; its beam waist in the direction of X axis and Y axis are w_x and w_y respectively. Therefore, its intensity can be split into two orthogonal directions. Then the intensity distribution of the laser beam in the coordinate system can be expressed by

$$I(x,y) = I_0 e^{-2\frac{(x-x_s)^2}{w_x^2} - 2\frac{(y-y_s)^2}{w_y^2}} \tag{4.15}$$

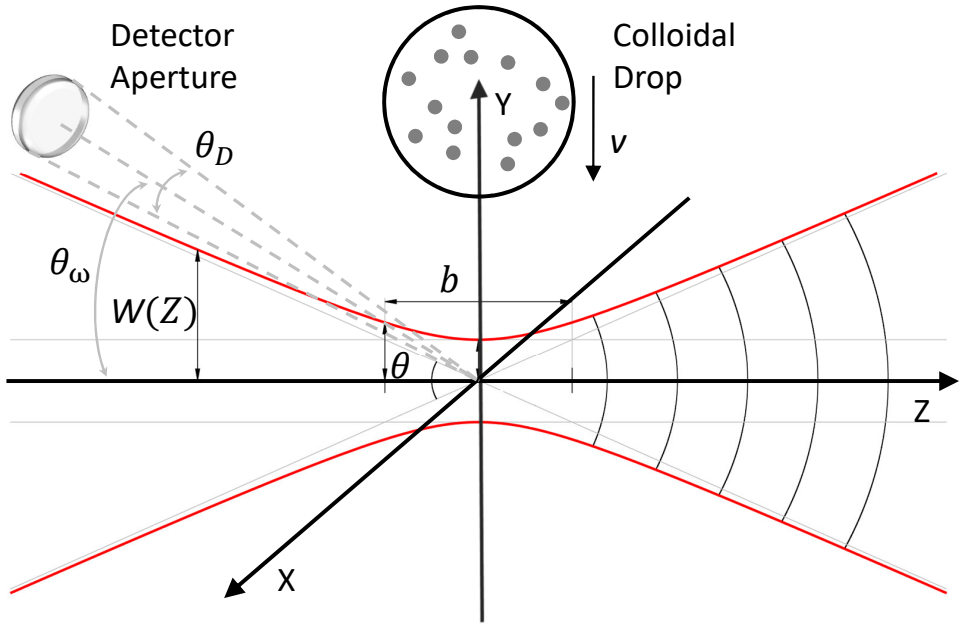

Figure 4.6: Gaussian beam intersection with drop

The time-shift signal comprises mainly reflection and second-order refraction scattering from the drop, scattering from first-order refraction does not reach the detector in backscatter and scattering from fourth-order refraction is very weak in intensity; therefore, in the following simulation only scattering from reflection and second-order refraction will be considered. The incident beam is treated as a large number of rays and the polarization state of each ray is the same and can be described using the normalized Stokes vector as $\mathbf{S}_i = [I \;\; Q \;\; U \;\; V]^T$. For a light ray which intersects the drop surface at the point $(x, \;\; y, \;\; z)$, if it reaches the detector, its Stokes vector can be calculated using

$$\mathbf{S}_R = I_0 e^{-2\frac{(x-x_s)^2}{w_x^2} - 2\frac{(y-y_s)^2}{w_y^2}} \times \mathbf{M}_{RRD} \cdot \mathbf{R}(\theta_R) \cdot \mathbf{S}_i \tag{4.16}$$

where $\mathbf{R}(\theta_R)$ is the rotation matrix; and $\mathbf{M}_{RRD}$ is the Mueller matrix at the incident point, when the light ray propagates from an optical rare medium to an optical dense medium. They are given with the Eqs (3.40) and (3.52). θ_R is the rotation angle for updating the local coordinate system and can be computed using

$$\theta_R = \arccos\left(\frac{x}{\sqrt{x^2+y^2}}\right) \tag{4.17}$$

The first element of the Stokes vector $\mathbf{S}_R$ represents the intensity of the reflected ray. Therefore, the time-shift signal generated by the reflection scattering from the drop can be obtained by integration of the first element of the Stokes vector $\mathbf{S}_R$ over the incident region S_R for the reflection:

$$P_R(y) = \iint_{S_R} \mathbf{S}_R(1,1)\, dx\, dy \tag{4.18}$$

For the outgoing ray from second-order refraction scattering, before reaching the detector it undergoes twice transmission and once reflection. Similar to the formulation of the Stokes vector for the reflection, the Stokes vector for second-order refraction scattering can be formulated as

$$\mathbf{S}_T = I_0 e^{-2\frac{(x-x_s)^2}{w_x^2} - 2\frac{(y-y_s)^2}{w_y^2}} \times \mathbf{M}_{TDR} \cdot \mathbf{M}_{RDR} \cdot \mathbf{M}_{TRD} \cdot \mathbf{R}(\theta_R) \cdot \mathbf{S}_i \tag{4.19}$$

where $\mathbf{M}_{TRD}$ is the Mueller matrix for transmission from an optically rare medium to an optically dense medium; $\mathbf{M}_{TDR}$ is the Mueller matrix for transmission from optical dense medium to an optically rare medium. Therefore, the time-shift signal generated by second-order refraction scattering can be formulated by integration of the first element of the Stokes vector $\mathbf{S}_T$ over the incident region S_T for second-order refraction scattering, i.e.

$$P_T(y) = \iint_{S_T} \mathbf{S}_T(1,1)\, dx\, dy \tag{4.20}$$

Then the time-shift signal can be formulated by combination of the signal generated by the reflection scattering and second-order refraction scattering:

$$P(y) = P_R(y) + P_T(y) \tag{4.21}$$

A time-shift signal has been computed with this analytical method and the ray-tracing method respectively, with the laser beam being perpendicularly polarized. The comparison is shown in Fig. (4.8).

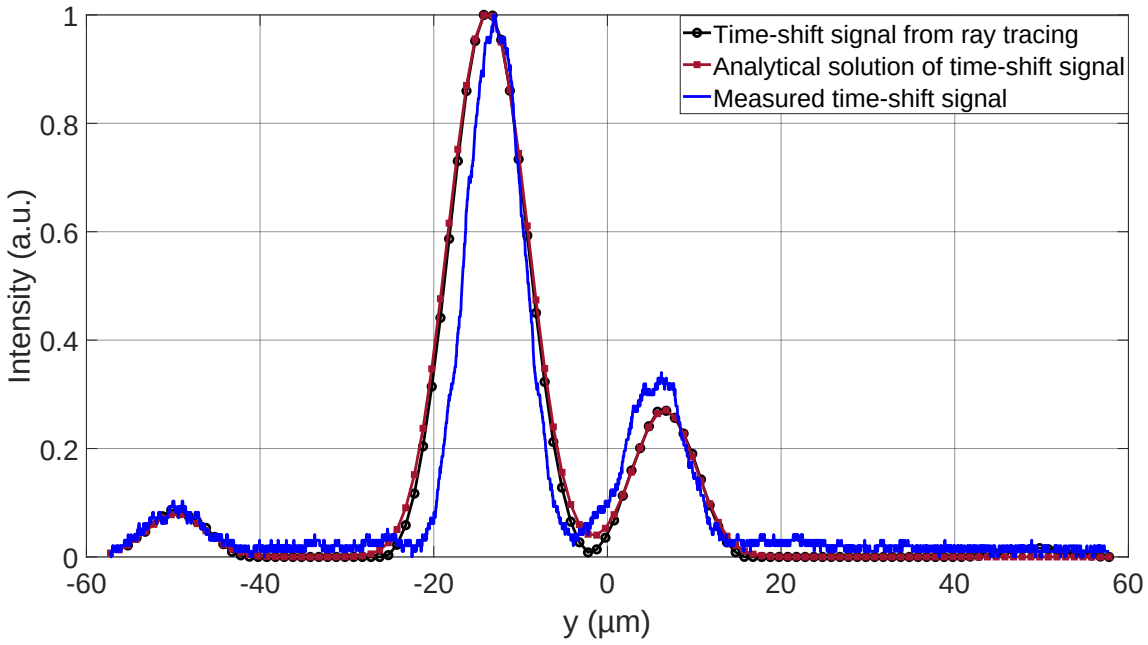

Figure 4.7: Comparison between ray tracing, measured time-shift signal and analytical solution for time-shift signal as the laser beam is parallel polarized.

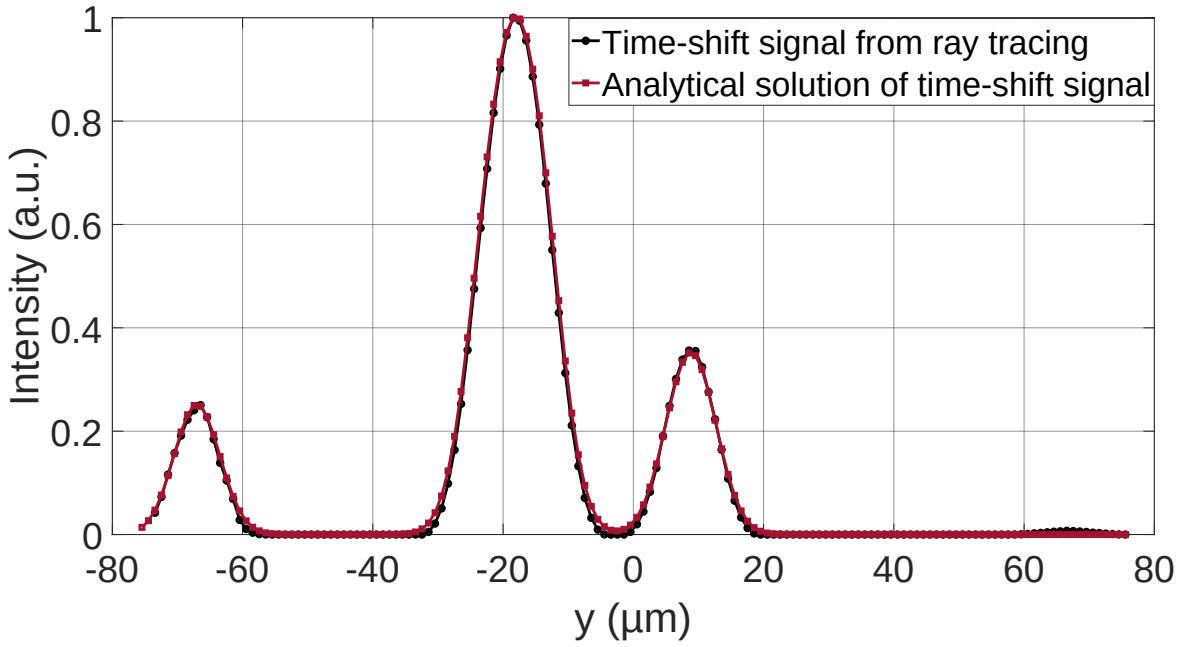

Figure 4.8: Comparison between ray-tracing and the analytical solution for the time-shift signal for perpendicular polarization.

When the incident region for the time-shift signal for the reflection scattering and second-order refraction scattering overlaps, the time-shift signal will also overlap. This would occur for larger ratios of laser beam waist to drop diameter or for certain spheroidal drops.

4.3 Simulated time-shift signal of complex particles

4.3.1 Spheroidal particles

In numerous applications of atomization it is of interest to determine whether the drops are spherical or non-spherical. Most commercial instruments for particle/drop characterization measure the particle size under the assumption that the particle is spherical; both the phase Doppler technique and the time-shift technique do so. The effect of non-sphericity on the size measurement using the phase Doppler technique has already been studied [7]. The effect of non-sphericity on the size measurement using the time-shift technique has not been investigated and the present subsection is devoted to this topic. Parts of this section have been published in the article Li, L., Rosenkranz, S., Schäfer, W., & Tropea, C. (2018). *Sensitivity of the time-shift technique in characterizing non-spherical drops.* In Proceedings of the Nineteenth International Symposium on the Application of Laser and Imaging Techniques to Fluid Mechanics.

As is evident from the light scattering simulations pictured in Fig. 4.9, a change of drop sphericity will strongly effect the light scattering. In the present study light scattering from ellipsoidal drops using the ray-tracing method will be examined. The signal from a time-shift instrument has been simulated for varying non-sphericities of the drop, but keeping the drop volume constant: i.e. the aspect ratio and refractive index have been varied. The aspect ratio is defined as the ratio of the major (a) to minor (c) axis dimension, thus values $a/c < 1$ correspond to prolate drops and values $a/c > 1$ to oblate drops. The incident light and the receiving detectors are chosen to correspond to typical configurations used in implementing the time-shift technique for particle sizing. The computational procedure is described for the most general case and results are presented for drops

aligned such that their major axis corresponds to the incident beam propagation direction. The resulting size measurement is then studied as a function of changing aspect ratio and relative refractive index (1.33, 1.36, 1.40). Using the simulated time-shift signal, the drop size has been calculated, as well as deviations from the nominal (equivalent spherical) diameter.

The simulation results indicate that the signals arising from the time-shift technique will reveal non-sphericity of drops, but that a reasonably good estimate of the volume equivalent size can be made by combining the size estimates from reflective and second-order scattered light. For the present ranges of aspect ratio and relative refractive index investigated, the average diameter fell within 14% of the true volume equivalent diameter.

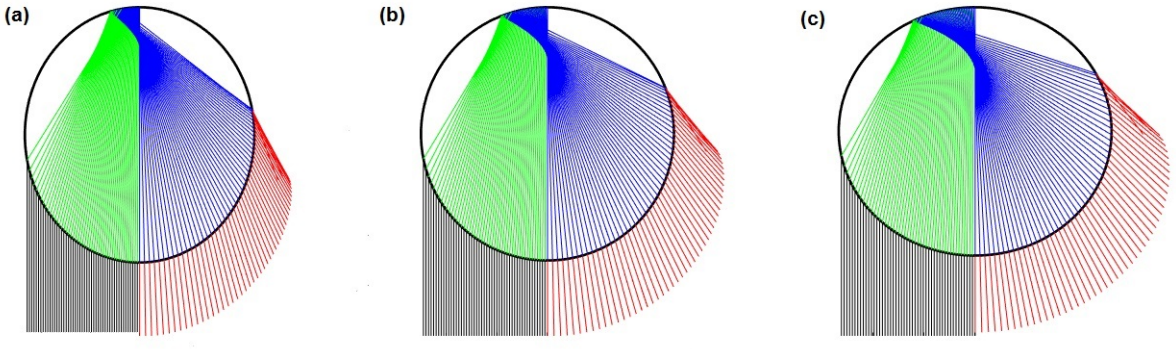

Figure 4.9: Ray-tracing simulations for $p = 2$: (a) $a/c = 0.90$, (b) $a/c = 1.0$ and (c) $a/c = 1.1$. The black lines represent the incident rays, and the green and blue lines represent, respectively, the refraction rays at the surface of a drop and reflected rays at the inner surface of a drop. The red lines denote the refracted rays $p = 2$. (p: scattering order)

Computational Procedure

The primary coordinate system is centered at the beam waist and aligned such that the Z-axis is in the beam propagation direction; polarization is with respect to the X-axis (s polarization). The drop is a spheroid (ellipsoid of revolution), given by

$$\frac{(x-x_0)^2}{a^2} + \frac{(y-y_0)^2}{b^2} + \frac{(z-z_0)^2}{c^2} = 1 \tag{4.22}$$

where (x_0, y_0, z_0) are the coordinates of the drop with respect to the center of the Gaussian beam waist. However, in the present study the drop can also be arbitrarily orientated when passing through the laser beam. The particle rotation is achieved using the Euler rotation theorem, by which the rotation can be described using three angles. There are several variations of this matrix and the so-called ZXZ rotation is used in this study. A right-handed coordinate system with a positive angle to represent any right-handed rotation is used. Rotations are first performed around the Z axis through an angle ψ, then around the (rotated) X' axis of the body through an angle β, and finally around the Z' axis of the body through an angle α. After performing the rotations, the entire body is translated. The body rotation of the spheroid is depicted in figure 4.10.

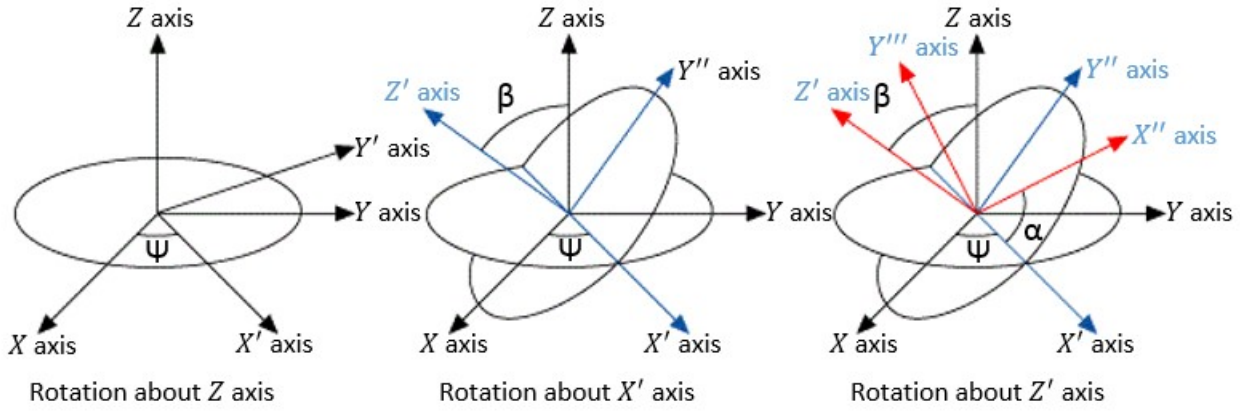

Figure 4.10: Orientation of drop after the ZXZ rotation

If (x', y', z') are the coordinates of a particular point prior to rotation and translation, and (x, y, z) are the coordinates of the point after rotation and translation, then the following relations hold:

$$\begin{pmatrix} x' \\ y' \\ z' \end{pmatrix} = \mathbf{R}_z(-\alpha)\mathbf{R}_x(-\beta)\mathbf{R}_z(-\psi) \begin{pmatrix} x - x_0 \\ y - y_0 \\ z - z_0 \end{pmatrix} \tag{4.23}$$

where:

$$\mathbf{R}_z(\psi) = \begin{pmatrix} \cos\psi & -\sin\psi & 0 \\ \sin\psi & \cos\psi & 0 \\ 0 & 0 & 1 \end{pmatrix} \tag{4.24}$$

$$\mathbf{R}_x(\beta) = \begin{pmatrix} 1 & 0 & 0 \\ 0 & \cos\beta & -\sin\beta \\ 0 & \sin\beta & \cos\beta \end{pmatrix} \tag{4.25}$$

$$\mathbf{R}_z(\alpha) = \begin{pmatrix} \cos\alpha & -\sin\alpha & 0 \\ \sin\alpha & \cos\alpha & 0 \\ 0 & 0 & 1 \end{pmatrix} \tag{4.26}$$

Substituting Eq. (4.24) into Eq. (4.22), then the spheroid in space is given by:

$$\frac{[(\cos\alpha\cos\psi - \sin\alpha\cos\beta\sin\psi)(x - x_0) + (-\cos\alpha\sin\psi - \sin\alpha\cos\beta\cos\psi)(y - y_0) + \sin\alpha\sin\beta(z - z_0)]^2}{a^2} +$$
$$\frac{[(\sin\alpha\sin\psi + \cos\alpha\cos\beta\sin\psi)(x - x_0) + (-\sin\alpha\sin\psi + \cos\alpha\cos\beta\cos\psi)(y - y_0) - \cos\alpha\sin\beta(z - z_0)]^2}{b^2} +$$
$$\frac{[(\sin\beta\sin\psi(x - x_0) + \sin\beta\cos\psi(y - y_0) + \cos\beta(z - z_0)]^2}{c^2} = 1 \tag{4.27}$$

To compute the signal arising from the passage of a drop through the focused beam of a time-shift instrument, first a drop position is specified and the light scattered onto a defined detector (position and size) is computed. With a given velocity in the Z direction (v_z), the drop is then displaced

by a step time of Δt and the computation is repeated. The intensity collected on the detector for each drop position is converted into a time signal using the prescribed drop velocity. To obtain the time-shift signal, the light scattering of all drop positions in which incident rays intersect with the drop need to be computed. The time-shift signal, exemplary illustrated in figure 4.1 for detectors placed on either side of the illuminated laser sheet, comprises three main peaks; one arising from reflected light ($p = 0$) and one each from the two modes of second-order refraction ($p = 2.1$, $p = 2.2$).

To understand the signal generation from an ellipsoidal drop, the incident and exit angle ranges through which a ray passes to fall onto a prescribed detector is analyzed for reflected and second-order refracted light. These angle ranges will be used to interpret the loss or overlap of signal peaks in the following section. For reflection, the incident and glare points on the surface of the drop are coincident. The glare region which a finite size detector sees on the drop is computed by traversing a point detector over the real detector area. The point detector has the coordinates $(0,\ y_d,\ z_d)$. Figure 4.11a illustrates the ray path when a reflected ray is incident on the point detector.

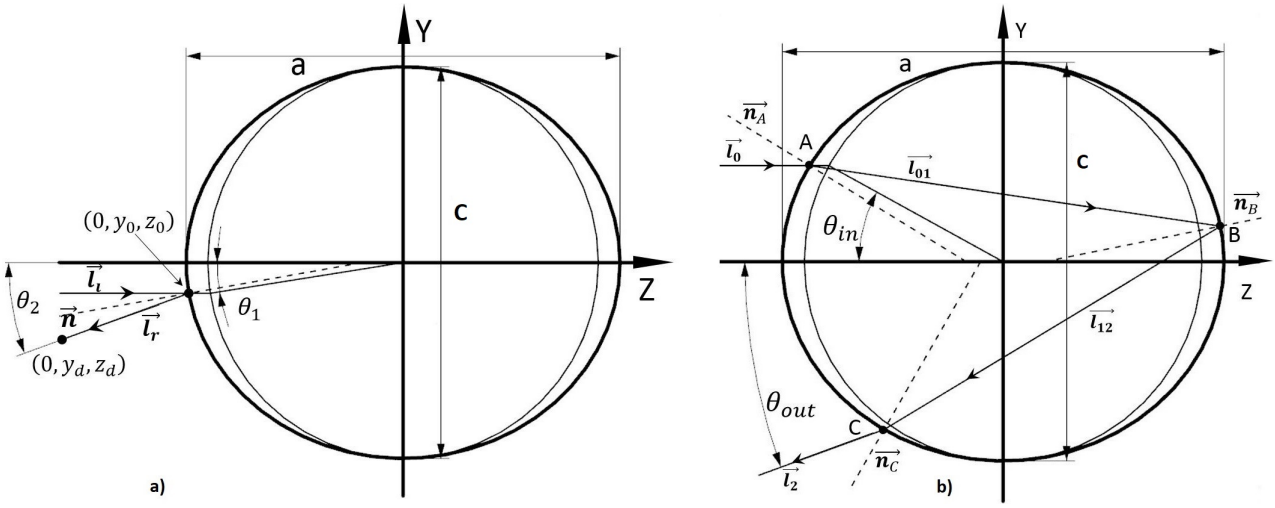

Figure 4.11: Ray paths for a point detector: a) reflection; b) second-order refraction

To reach the point detector Eq. (4.28) should be satisfied, where $\mathbf{l}_i$ and $\mathbf{l}_r$ represent the incident and the reflected ray vectors, and $\vec{\mathbf{n}}$ is the normal vector at the incident/glare point $(0,\ y_0,\ z_0)$ and can be calculated as $\nabla f(0\ \ y_0\ \ z_0)/|f|$; where f is surface of the ellipsoid.

$$\frac{|\vec{\mathbf{l}_i} \cdot \vec{\mathbf{n}}|}{\|\vec{\mathbf{l}_i}\| * \|\vec{\mathbf{n}}\|} = \frac{|\vec{\mathbf{l}_r} \cdot \vec{\mathbf{n}}|}{\|\vec{\mathbf{l}_r}\| * \|\vec{\mathbf{n}}\|} \tag{4.28}$$

Substituting expressions for each of the variables into Eq. (4.28) yields the following relation:

$$|-\kappa * \cos\theta_1| = \left| \frac{-\sin\theta_1 * (y_d + \kappa * b * \sin\theta_1) - \kappa * \cos\theta_1 * (z_d + a * \cos\theta_1)}{\sqrt{(y_d + \kappa * b * \sin\theta_1)^2 + (z_d + a * \cos\theta_1)^2}} \right| \tag{4.29}$$

where κ is the inverse of the aspect ratio written as $\kappa = c/a$. This equation can be solved for the eccentric anomaly angle θ_1, the angle corresponding to the incident/glare point. To compute the glare point region for scattering by second-order refraction, the relationship between the incident angle θ_{in} and exit angle θ_{out}, illustrated in figure 4.11b, has been computed by using the Eqs. (4.30) - (4.35) in [68]:

$$\mathbf{L}_{01} = \frac{1}{m}[\mathbf{L}_0 - (\mathbf{L}_0 \cdot \mathbf{n}_A)\mathbf{n}_A] - \sqrt{1 - \frac{1}{m^2} + \frac{1}{m^2}(\mathbf{L}_0 \cdot \mathbf{n}_A)^2} \cdot \mathbf{n}_A \tag{4.30}$$

$$M_2 = \frac{\frac{y_0}{b^2} + \frac{p_0}{n_0}\frac{z_0}{c^2}}{\frac{1}{b^2} + \frac{{p_0}^2}{{n_0}^2}\frac{1}{c^2}} \tag{4.31}$$

$$\begin{cases} x_2 = x_0 \\ y_2 = y_0 - 2 * M_2 \\ z_2 = z_0 - 2 * M_2 * \frac{p_0}{n_0} \end{cases} \tag{4.32}$$

$$\mathbf{L}_{12} = \mathbf{L}_{01} - 2 * (\mathbf{L}_{01} \cdot \mathbf{n}_B)\mathbf{n}_B \tag{4.33}$$

$$\mathbf{L}_2 = m[\mathbf{L}_{12} - (\mathbf{L}_{12} \cdot \mathbf{n}_C)\mathbf{n}_C] + \sqrt{1 - m^2 + m^2(\mathbf{L}_{12} \cdot \mathbf{n}_C)^2 \cdot \mathbf{n}_C} \tag{4.34}$$

$$\theta_{out} = \arccos(\mathbf{L}_2 \cdot [0 \;\; 0 \;\; -1]) \tag{4.35}$$

Where p_0 and n_0 are the elements of the direction vector in y and z-axis in the Cartesian coordinate system.

Simulation results

In the following simulations of the time-shift signal for an ellipsoidal drop, the volume of the drop has been kept constant at the volume of a drop with diameter 100 μm; the aspect ratio has been varied among the values η= 0.9, 1.0 and 1.1 and the relative refractive index has taken the values m = 1.33, 1.36 and 1.40.

In Fig. 4.12, the left diagram presents the simulated time-shift signal for different relative refractive indices and the right diagram shows the relationship between the exit angle of second-order refraction scattering and the corresponding incident angle, when the aspect ratio is 0.9. The red dashed line and the green dashed line represent the upper and lower exit angle range for which reflective light will fall onto the detector. Only when the exit angle of the second-order refraction scattering is in the angle range between the green dashed line and red dashed line, will the exit ray be incident on the detector. When the refractive index is 1.33, the incident angle range for second-order refraction scattering results in two, well separated regions for the incident angle, yielding also two well separated peaks in the time-shift signal. These two peaks correspond to the p = 2.1 and 2.2 modes respectively. For the relative refractive index of 1.36 and 1.40 the incident angle for the p = 2.1 and 2.2 modes does exhibit distinct ranges and the peaks in the time-shift signal for these modes overlap with each other, as seen in the left diagram of Fig. 4.12.

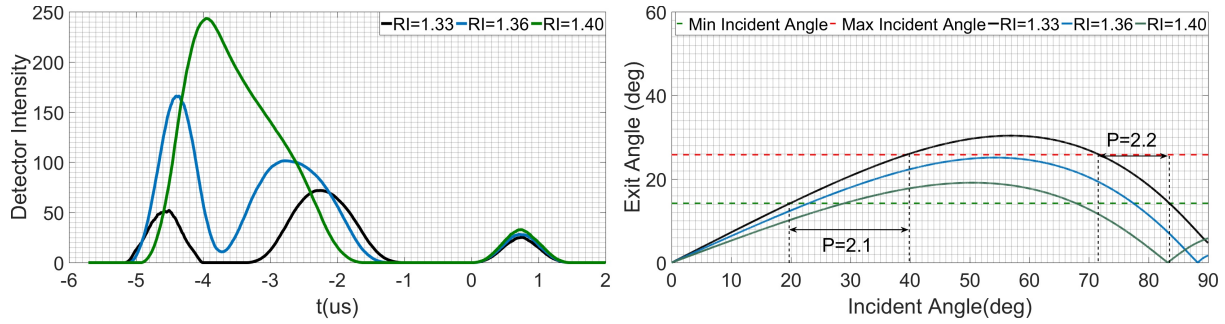

Figure 4.12: Left - simulated time-shift signal for different relative refractive indexes; Right - relationship between incident angle and exit angle of second-order refractive scattering, for an aspect ratio of 0.9. (RI stands for refractive index)

From Fig. 4.13, computed for an aspect ratio of 1.0, the two signal peaks corresponding to second-order refractive scattering are distinct for all relative refractive indexes.

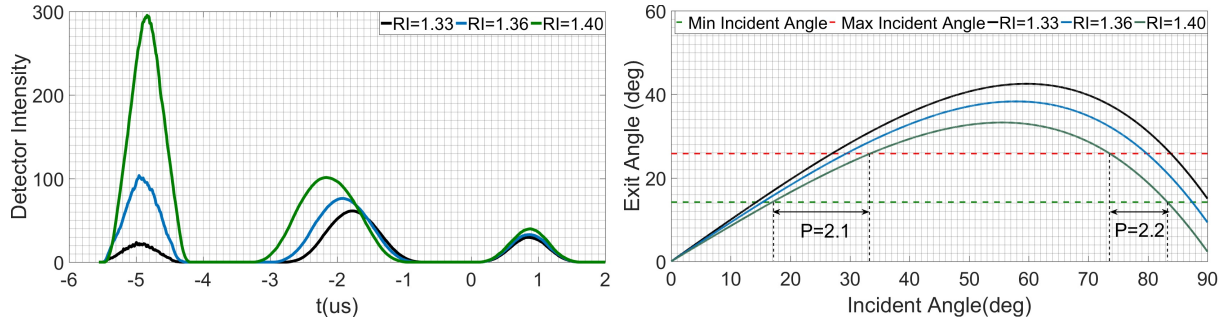

Figure 4.13: Left - simulated time-shift signal for different relative refractive indexes; Right - relationship between incident angle and exit angle of second-order refractive scattering, for an aspect ratio of 1.0. (RI stands for refractive index)

For the aspect ratio 1.1, shown in Fig. 4.14, the incident angle range for the mode $p = 2.2$ and for the relative refractive index 1.40 is larger than the angle range for $m = 1.36$. For the relative refractive index 1.33, no angle range for mode $p = 2.2$ exists, which means the time-shift signal for the mode p =2.2 does not exist and no respective peak appears in the signal (left diagram in Fig. 4.14.)

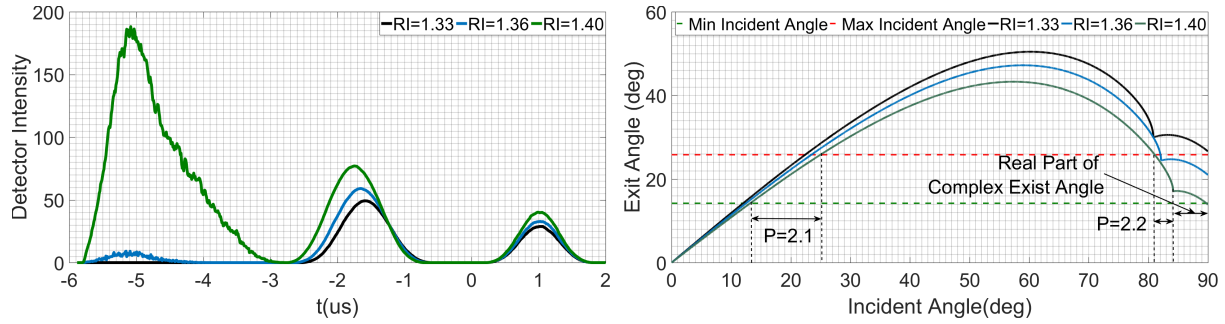

Figure 4.14: Left - simulated time-shift signal for different relative refractive indexes; Right - relationship between incident angle and exit angle of second-order refractive scattering, for an aspect ratio of 1.1. (RI stands for refractive index)

For a typical time-shift signal, there are several ways to evaluate the particle size, as Fig. 4.1 illustrates. The particle size has been calculated with various time differences by using Eqns. (4.36) - (4.37) derived in [51] and the evaluation results are tabulated in Tab. 4.1, as well as an average of the results from both evaluation methods.

$$d = \Delta t_{00} * \frac{V_z}{\cos(\frac{\theta_s}{2})} \tag{4.36}$$

$$d = \Delta t_{2121} * \frac{V_z}{\sin(\theta_i^{(p=2.1)})} \tag{4.37}$$

AR \ RRI	1.33	1.36	1.40
$b/a = 0.9$ $a = 51.787\mu m$ $b = 46.609\mu m$ $c = 51.787\mu m$	$d_{\Delta t_{00}} = 43.65\mu m$ $d_{\Delta t_{2121}} = 64.52\mu m$ $\frac{d_{\Delta t_{00}}+d_{\Delta t_{2121}}}{2} = 54.085\mu m$	$d_{\Delta t_{00}} = 40.77\mu m$ $d_{\Delta t_{2121}} = 74.09\mu m$ $\frac{d_{\Delta t_{00}}+d_{\Delta t_{2121}}}{2} = 57.43\mu m$	$d_{\Delta t_{00}} = 42.50\mu m$ Signal for second order refraction scattering $p = 2.2$ with $p = 2.1$ overlap
$b/a = 1$ $a = 50\mu m$ $b = 50\mu m$ $c = 50\mu m$	$d_{\Delta t_{00}} = 49.81\mu m$ $d_{\Delta t_{2121}} = 50.57\mu m$ $\frac{d_{\Delta t_{00}}+d_{\Delta t_{2121}}}{2} = 50.19\mu m$	$d_{\Delta t_{00}} = 49.81\mu m$ $d_{\Delta t_{2121}} = 50.73\mu m$ $\frac{d_{\Delta t_{00}}+d_{\Delta t_{2121}}}{2} = 50.27\mu m$	$d_{\Delta t_{00}} = 49.81\mu m$ $d_{\Delta t_{2121}} = 50.74\mu m$ $\frac{d_{\Delta t_{00}}+d_{\Delta t_{2121}}}{2} = 50.275\mu m$
$b/a = 1.1$ $a = 48.463\mu m$ $b = 53.28\mu m$ $c = 51.787\mu m$	$d_{\Delta t_{00}} = 60.83\mu m$ $d_{\Delta t_{2121}} = 45.66\mu m$ $\frac{d_{\Delta t_{00}}+d_{\Delta t_{2121}}}{2} = 53.245\mu m$	$d_{\Delta t_{00}} = 59.10\mu m$ $d_{\Delta t_{2121}} = 44.31\mu m$ $\frac{d_{\Delta t_{00}}+d_{\Delta t_{2121}}}{2} = 51.705\mu m$	$d_{\Delta t_{00}} = 56.80\mu m$ $d_{\Delta t_{2121}} = 41.87\mu m$ $\frac{d_{\Delta t_{00}}+d_{\Delta t_{2121}}}{2} = 49.335\mu m$

Table 4.1: Evaluation of the size of an ellipsoidal particle by using the simulated time-shift signal. (AR: Aspect Ratio; RRI: Relative Refractive Index)

The results from Tab. 4.1 indicate that for spherical drops the time-shift technique yields good estimates of drop diameter independent of which time shift is used for computation. This fact can be exploited in two ways. First, size can be computed using the time difference from both reflection and second-order refraction and only if the two estimates agree within bounds, will the value be accepted; hence this is a validation check. If the two values do not agree, this is an indication of non-sphericity. Second, if the drop is non-transparent or semi-transparent, such that signal peaks from second-order refraction are very weak, the size estimate from reflective scattering should be sufficient.

However, the simulations indicate also that the time-shift signal is significantly affected by changing either the relative refractive index or the aspect ratio of the ellipsoidal drop. Quite generally, the deviation of the drop size calculated by using the time difference from the reflection scattering order (Δt_{00}) exhibits a different sign compared with the deviation of the drop size calculated by using the time difference from second-order refractive scattering (Δt_{2121}). This holds for all values of relative refractive index and aspect ratio investigated. Which of the two methods results in a positive or negative deviation depends on the aspect ratio. For oblate drops ($b/a < 1.0$) the reflective estimate (Δt_{00}) lies below the true value and for prolate drops ($b/a > 1.0$) the estimate exceeds the true size. However, using a combination of both calculation methods, i.e. the average drop size, the simulation indicates that the size measurement is more robust against a change of the aspect ratio and the relative refractive index. For the present ranges of aspect ratio and relative refractive index investigated, the average diameter fell within 14% of the true volume equivalent diameter.

Notable is the fact that for high values of relative refractive index and prolate drops a size estimate cannot be made using second-order refraction, since the signal peak for $p = 2.2$ is missing. The computational procedure introduced in this study is capable of also treating ellipsoidal drops with arbitrary orientation with respect to the incident beam. However, the present results have focused only on cases in which the drop z-axis was aligned with the incident beam propagation direction.

4.3.2 Drop with an embedded particle

As mentioned in the Chapter 1, there exists a need to characterize drops with an embedded flake or sphere. In this section, time-shift signals for a drop with an embedded particle were simulated, in order to obtain the signal features which might characterize such kinds of drops.

Simulation for detecting the existence of an embedded spherical particle

Subsequent simulations of time-shift signals for a drop with an embedded particle are simulated for a scattering angle $\theta_s = 160°$ and p polarization. Note also that the convection time of the particle through the laser beam has been scaled such that the particle is centered in the beam at $t = 0$. Time is made dimensionless using $t^* = t \cdot v_z / D_{Drop}$. Consequently, the $p = 0$ peak occurs at times with opposite sign than the $p = 2.1$ or $p = 2.2$ peaks. The dashed line signal appearing in the subsequent diagrams represents the undisturbed signal generation.

In Fig. 4.15, the dashed line resembles closely the expected signal structure from a time-shift device; however, the $p = 2.2$ peak exhibits some oscillations in intensity. This arises simply because the incident point/surface through which rays pass to reach the detector by second-order refraction is very small compared to the incident surfaces for $p = 0$ or $p = 2.1$; hence, many fewer rays are used to construct the signal. If the number of rays is increased significantly above the standard value, then these oscillations vanish.

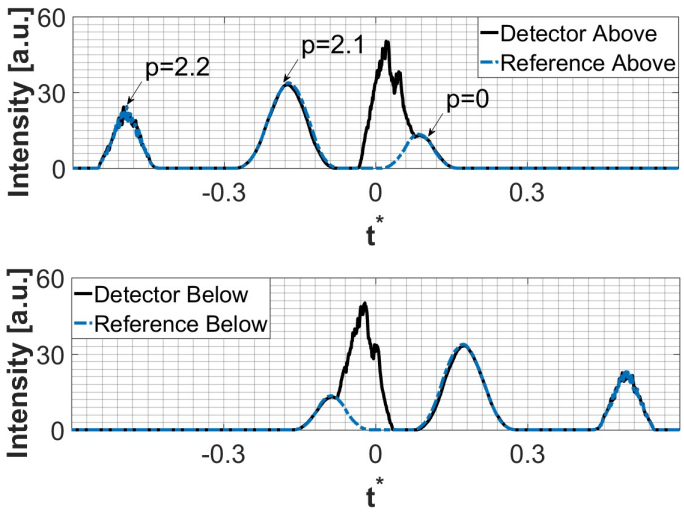

Figure 4.15: Simulated time-shift signal for a drop with embedded spherical particle: $D_P^* = 0.2, \psi = [0, 0, 0], n_t = 1.33, \theta_s = 160°$, p polarization. Reproduced from [28].

Strictly speaking another dimensionless length scale arises when considering the signal generated by a time-shift device, namely the ratio of drop diameter to beam waist. The peak width will scale proportional to this ratio. In the following computations this ratio has not been varied, but a value typical of time-shift devices has been chosen. No fundamental differences are expected for other values, only the peak width would vary.

Fig. 4.15 shows the time-shift signal for a drop with an embedded spherical particle residing in the center of the drop. Comparing with the standard time-shift signal and dashed line in Fig. 4.15, the signal width from the reflection peak ($p = 0$) becomes significantly wider, due to the scattered light from the embedded spherical particle. Also in this case the signal intensity exhibits strong amplitude oscillations, due to the same reason discussed above. To illustrate this in more detail the relationship between the incident angle θ_i and the exit angle θ_{out} of the scattered ray $\mathbf{l}_2$ has been calculated. The geometry of this ray reflecting off an embedded particle is illustrated in Fig. 4.16.

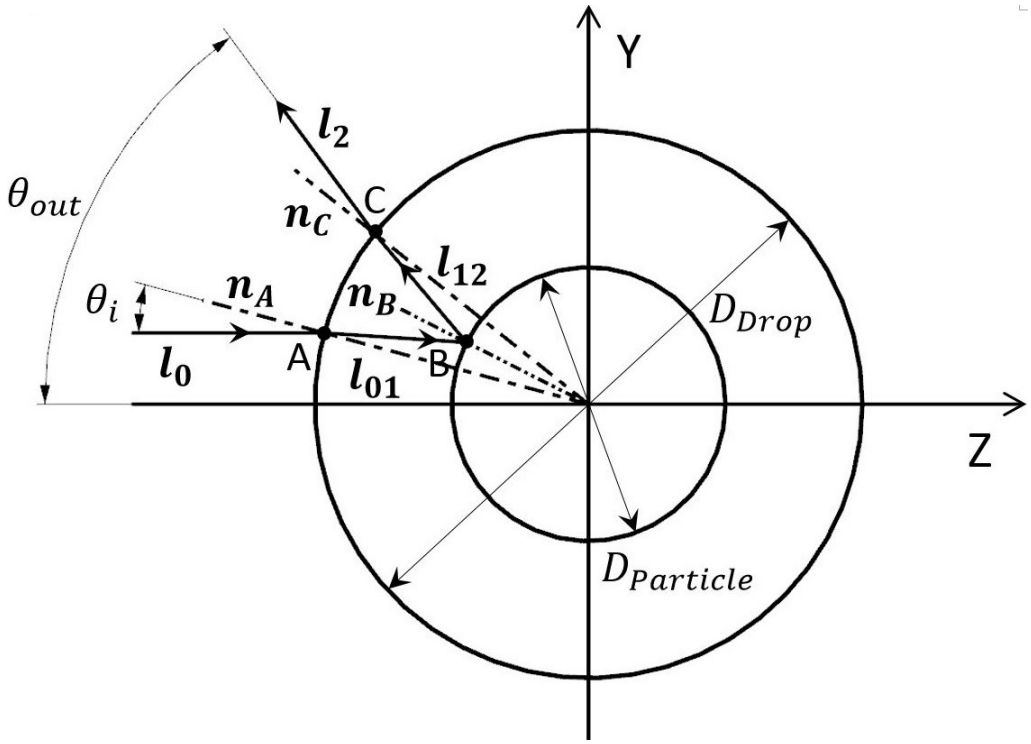

Figure 4.16: Demonstration of scattering by embedded particle. Reproduced from [28].

In the scattering plane, the exit angle θ_{out} can be computed by using Eqs. (4.30) - (4.35). The relationship between the incident angle θ_i and the exit angle θ_{out} of the scattered ray from the embedded particle is plotted in Fig. 4.17 for the different scattering orders. This figure shows the drop surface ranges (expressed as incident angle) over which the incident beam will reach the upper and lower limit of the detector aperture (in this case 14.198 deg to 25.01 deg, corresponding to typical device specifications). As can be seen, the drop surface contributing to the signal arising from reflection from the embedded particle is very small compared to all other scattering orders ($p = 0, 2.1, 2.2$), i.e. relatively few incident rays are used in computing the detector signal; hence, the increased fluctuations in the signal is observed in Fig. 4.15.

When the embedded spherical particle becomes larger, the simulated time-shift signal changes significantly, as Fig. 4.18 shows. The amplitude of the signal peak from the reflection scattering becomes much stronger in amplitude; additionally, one signal peak from the second-order refraction ($p = 2.1$) scattering is lost. This is because when the particle reaches a certain size, it will block the ray path for part of second-order refraction scattering.

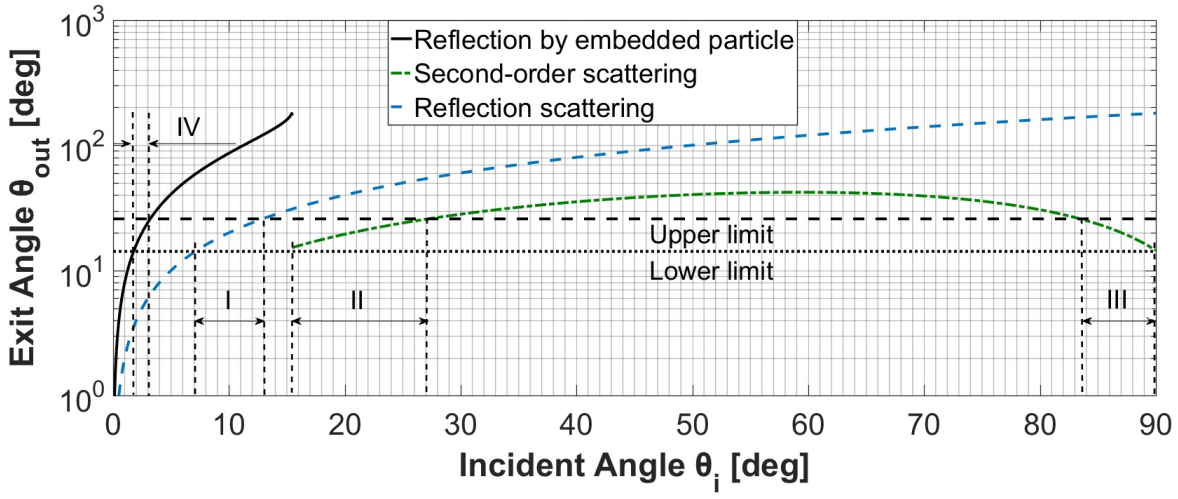

Figure 4.17: The relationship between incident angle and exit angle for different scattering orders. I: incident angle range for reflection scattering ($p = 0$); II: incident angle range for the second-order refraction, first mode ($p = 2.1$); III: incident angle range for the second-order refraction, second mode ($p = 2.2$); IV: incident angle range for the reflection scattering from embedded particle ($D_P^* = 0.2, n_t = 1.33$). Reproduced from [28].

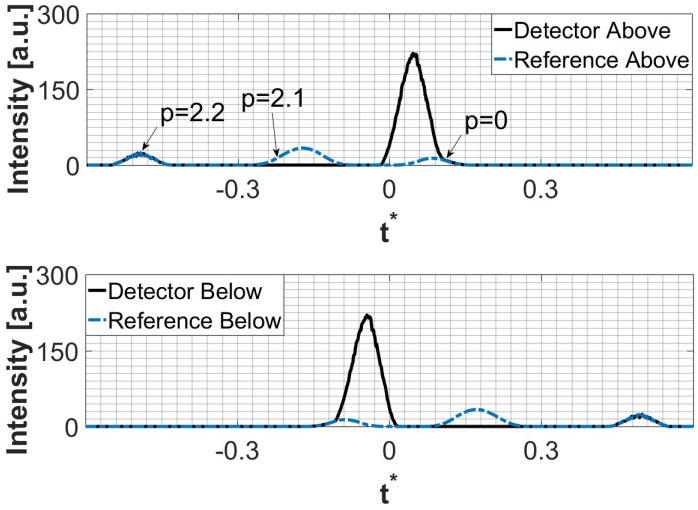

Figure 4.18: Simulated time-shift signal for a drop with embedded spherical particle: $D_P^* = 0.45, \psi = [0, 0, 0], n_t = 1.33, \theta_s = 160°$, p polarization. Reproduced from [28].

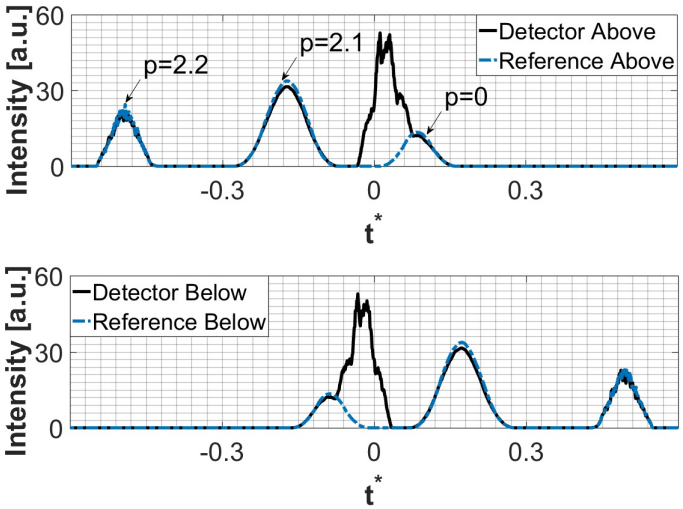

Figure 4.19: Simulated time-shift signal for a drop with embedded spherical particle: $D_P^* = 0.2, \psi = [0.05, 0, 0], n_t = 1.33, \theta_s = 160°$, p polarization. Reproduced from [28].

In Fig. 4.19, the embedded spherical particle is no longer in the centre of the drop; an offset exists in the X axis. A signal behaviour similar to that obtained using a centered particle is obtained; the scattered light from the embedded particle overlaps with the reflected light from the drop surface and leads to a widening of the signal peak from the reflection scattering. It is apparent from the signal amplitude oscillations that this occurs over a rather small incident surface on the drop.

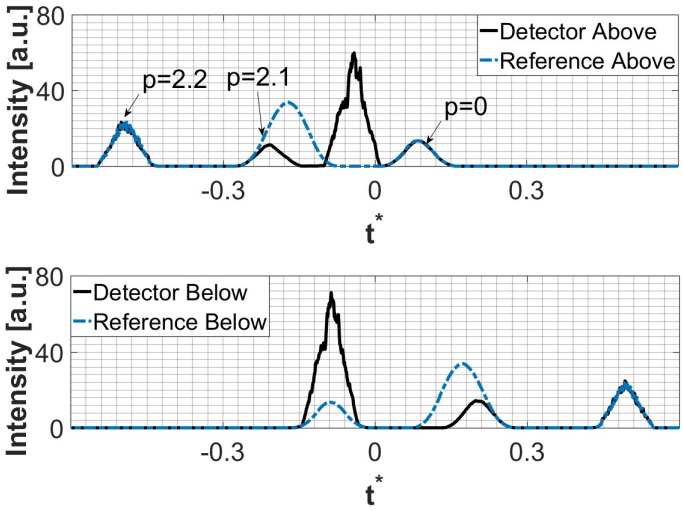

Figure 4.20: Simulated time-shift signal for a drop with embedded spherical particle: $D_P^* = 0.2, \psi = [0, 0.05, 0], n_t = 1.33, \theta_s = 160°$, p polarization. Reproduced from [28].

When the offset of the particle is in the direction of the Y axis, the simulated time-shift signal from the detectors above and below lose symmetry, and the signal amplitude of the second-order refraction signal peak is reduced significantly, as Fig. 4.20 shows. When the offset is in the direction of the Z axis, the simulated time-shift signal exhibits features similar to the time-shift signals shown in Fig. 4.15 and Fig. 4.19.

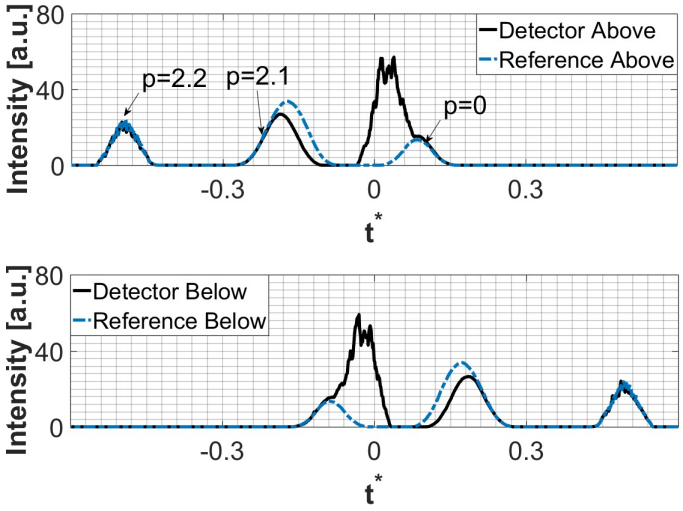

Figure 4.21: Simulated time-shift signal for a drop with embedded spherical particle: $D_P^* = 0.2, \psi = [0, 0, 0.05], n_t = 1.33, \theta_s = 160°$, p polarization. Reproduced from [28].

Simulation for detecting the existence of an embedded flake

The time-shift signal has also been simulated for the drop with an embedded flake. Fig. 4.22 shows the simulated time-shift signal for the drop with an embedded flake, located in the center of the drop. This figure uses a logarithmic scale, because a signal peak for $p = 2.1$ with extremely high amplitude is obtained, arising due to reflection from the embedded flake. The other signal peaks remain virtually unchanged in amplitude, as evident from the complete congruence of the reference and detector signals

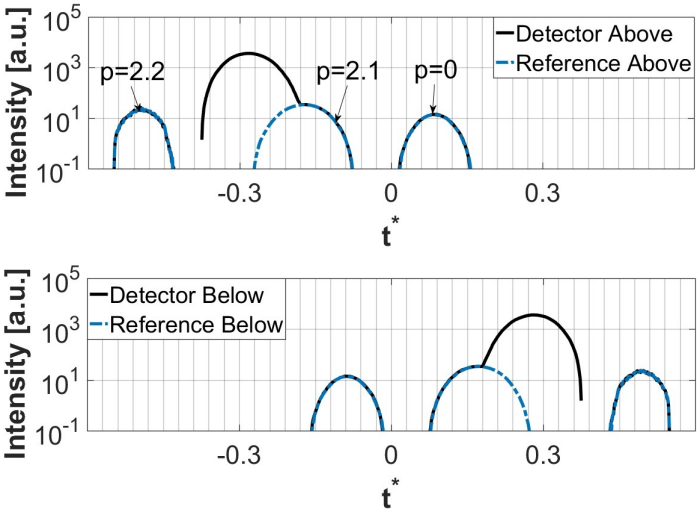

Figure 4.22: Simulated time-shift signal for a drop with embedded spherical particle: $D_F^* = 0.5, \psi = [0, 0, 0], \alpha = 0°, \beta = 0°, n_t = 1.33, \theta_s = 160°$, p polarization. Reproduced from [28].

For a different orientation of the flake, the time-shift signal also exhibits a strong signal peak; at the same time, the signals from the detectors above and below lose symmetry, as Fig. 4.23 shows for the case of a zenith angle $\alpha = 20$ deg and azimuthal angle $\beta = 50$ deg.

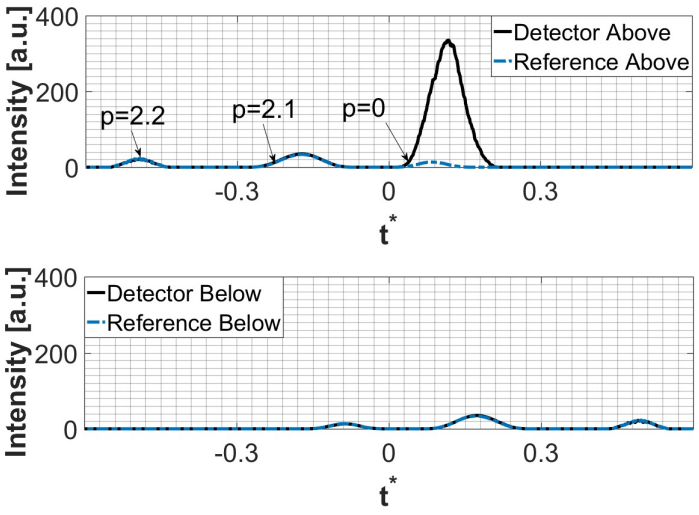

Figure 4.23: Simulated time-shift signal for a drop with embedded spherical particle: $D_F^* = 0.5, \psi = [0, 0, 0], \alpha = 20°, \beta = 50°, n_t = 1.33, \theta_s = 160°$, p polarization. Reproduced from [28].

However, for some orientations, comparing with the time-shift signal from the pure drop, the time-shift signal from the drop with embedded flake does not exhibit a strong difference, as Fig. 4.24 shows. For this situation the existence of the embedded flake would not be detected with the time-shift technique.

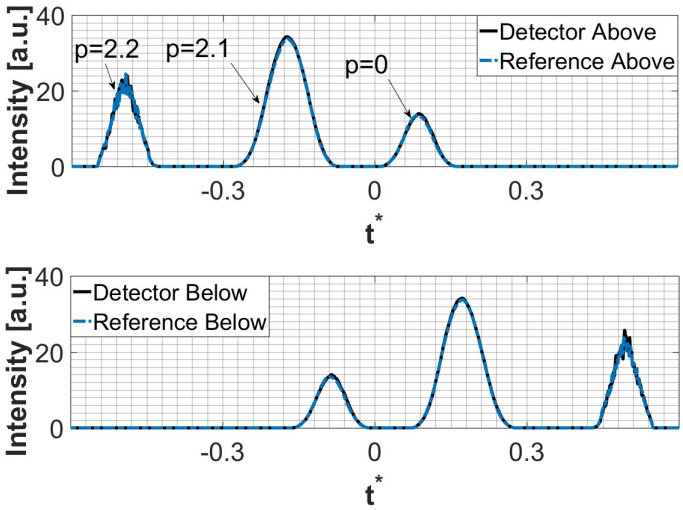

Figure 4.24: Simulated time-shift signal for a drop with embedded spherical particle: $D_F^* = 0.5, \psi = [0, 0, 0], \alpha = 20°, \beta = 10°, n_t = 1.33, \theta_s = 160°$, p polarization. Reproduced from [28].

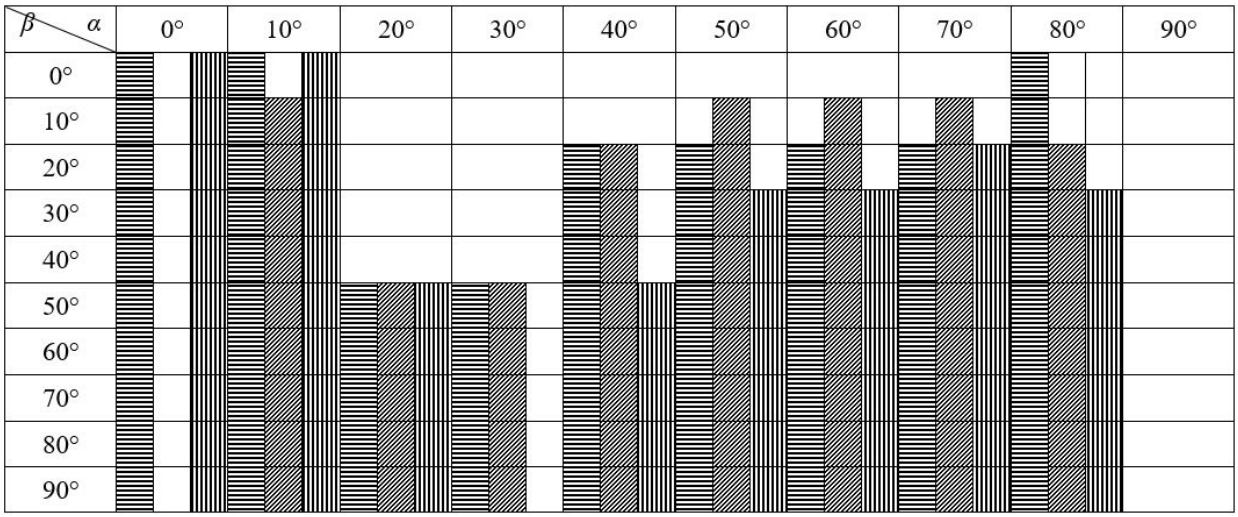

Figure 4.25: Simulations concerning the detection of an embedded flake by varying the zenith and azimuthal angles in the range 0° to 90° with an interval of 10°. ($D_P^* = 0.5, \psi = [0, 0, 0], \sigma = 0$. Horizontal shading means significant change of signal amplitude; diagonal shading means the loss of symmetry and vertical shading means significant change of signal width.) Reproduced from [28].

To explore over what ranges of zenith and azimuthal angles of flake orientation the embedded flake could be detected, the time-shift signal has been simulated for varying zenith and azimuthal angles. Then the simulated time shift signals have been compared with the reference signal to see if one of the following features could be observed: significant change of signal amplitude (more than 40%), the loss of symmetry and/or significant change of peak width. When any one of these features could be observed, the assumption is made that the flake could be unequivocally recognized. Fig. 4.25 shows the results of these simulations by indicating which combinations of zenith and azimuthal angles are likely to result in a signal from which the flake could be recognized. These

features have been marked with different kinds of shading in Fig. 4.25. For this set of simulations, a signal difference could be observed in about 70% of all simulations. Noticeable is that, when the zenith angle is 90°, all of the detections fail; this is because of the geometric symmetry, which leads to the individual scattering orders unchanged, as shown in Fig. 3.15

In practice, the embedded flake could exhibit a rough surface. The light scattering of particles with rough surfaces has been studied by Stegmann [57], Germer [11], Nousiainen [40], and Yang and Liou [67]. The model from Yang and Liu [67] has been implemented in the current code, in which the surface is constructed with facets, whose random tilts are specified as

$$\cos\theta = \frac{1}{(1-\sigma^2 \times \ln(\eta_1))^{\frac{1}{2}}} \tag{4.38}$$

$$\phi = 2 \times \pi \times \eta_2 \tag{4.39}$$

Here θ and ϕ are polar and azimuthal angles in the local spherical coordinate system based on the embedded flake; η_1 and η_2 are random numbers and are distributed uniformly over zero to unity. σ defines the magnitude of roughness. $\sigma = 0 - 0.005, 0.005 - 0.05, 0.05 - 0.2$ correspond to slight, moderate and deep roughness. The time-shift signals are simulated under the same orientation as in Fig. 4.24 by varying σ. One exemplary result is shown in Fig. 4.26. In this particular case the $p = 2.1$ peak (second-order refraction, mode 1) is strongly broadened. This is understandable, since only rays contributing to this peak interacted with the flake surface. The reflected rays and $p = 2.2$ rays scatter unhindered from the drop. This is fortuitous, since the drop size measurement could then still be performed using time shifts between for instance the $p = 2.2$ peaks of the two detectors. The distorted $p = 2.1$ peak would indicate the presence of a flake.

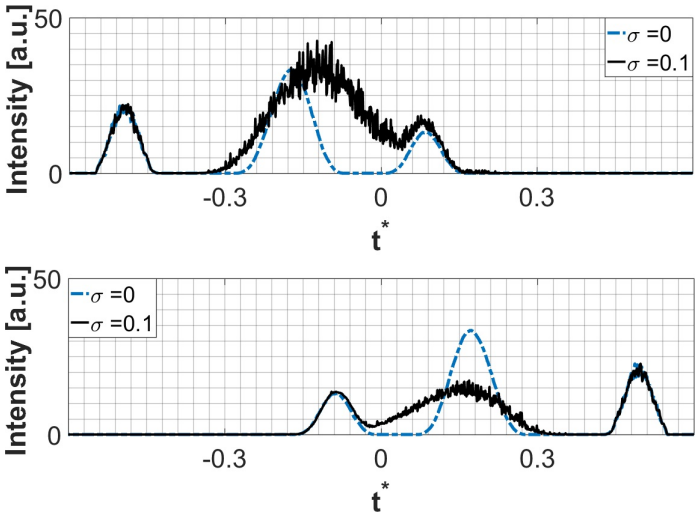

Figure 4.26: Simulated time-shift signal with a rough embedded flake: $D_F^* = 0.5, \psi = [0, 0, 0], \alpha = 20°, \beta = 10°, n_t = 1.33, \theta_s = 160°$, p polarization. Reproduced from [28].

Similar to Fig. 4.25, the signal generation of the drop with an embedded, rough surfaced flake has been computed over the same zenith and azimuthal angles as in Fig. 4.25. The results are shown in Fig. 4.27.

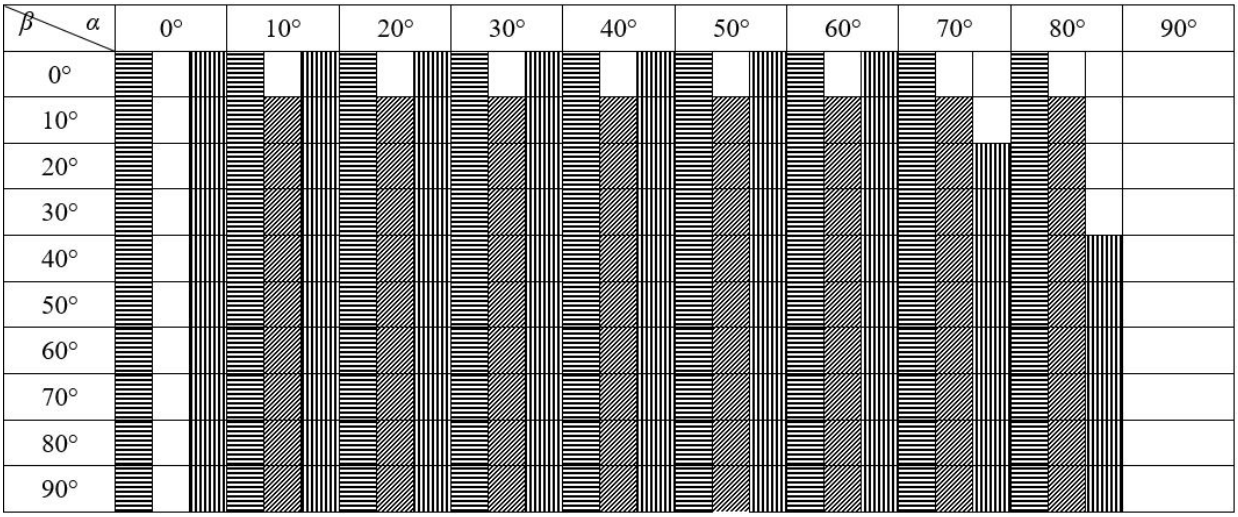

Figure 4.27: Simulations concerning the detection of an embedded flake by varying the zenith and azimuthal angles in the range 0° to 90° with an interval of 10°. ($D_P^* = 0.5, \psi = [0, 0, 0], \sigma = 0.1$. Horizontal shading means significant change of signal amplitude; diagonal shading means the loss of symmetry and vertical shading means significant change of signal width.) Reproduced from [28].

The underlying question of this study is whether the time-shift technique can be used to not only determine the size and velocity of drops, but also whether the drop contains an embedded spherical particle or a flake. To answer this question first the light scattering from such drops has been studied and validated and then typical instrument specifications for a time-shift device have been used to generate simulated signals from the device.

Consider first the case of a drop with an embedded spherical particle. Such situations arise when a solid particle is surrounded by a liquid, which is typical of encapsulation processes such as spraying into a fluidized bed. In such cases the surface tension is likely to establish a uniform coating of the particle, i.e. the assumption that the particle is centered in the drop is quite realistic and most results have been generated for this case. The scattering diagrams presented in section 3.1.1 indicate additional backscatter contributions arising from the reflection of light from the embedded particle and these contributions increase the amplitude and duration of the reflection peak in the time-shift signals for virtually all geometrical situations studied. Therefore, one can conclude that, with suitable signal detection and modifications to the signal processing, the time-shift technique should be able to unequivocally detect whether a drop contains a spherical particle or not. To what extent this statement can also apply to non-spherical embedded particles or not fully reflective particles cannot be answered at this time, but the ray-tracing algorithm introduced in this study could principally be used to investigate such cases with little modification.

Considering the case of a drop with an embedded flake, a situation of particular interest when measuring metallic paints, the answer is less conclusive. The flake can have several effects on the signal received by a time-shift device, ranging from suppression of certain peaks to enhancement of others, in some cases by several orders of magnitude. The main determining factor becomes the orientation of the flake in the drop with respect to the incident beam and detectors. There is no physical reason to assume that flakes will favour a particular orientation for drops in a flow field and therefore the actual orientation is likely to be randomly distributed. Given a uniform orientation probability the results presented in Fig. 4.25 suggest that the probability of flake detection is somewhere around 70%, although if a flake is detected, the correctness of the measurement is likely very high. The uncertainty of flake detection could be reduced by adding further detectors at different scattering angles, e.g. in forward scatter; however, this would complicate greatly the device design and alignment, one of the advantages presently exploited by working solely in backscatter.

In either case, embedded particle or flake, the assumption of a perfectly reflecting smooth surface was made. However, in reality the inclusion may exhibit a rough surface, in which case the reflection will be more diffuse. This situation has been investigated for the case of an embedded flake and sample simulated signals confirm that signal peaks arising from rays which interact with the flake, in this case $p = 2.1$, exhibit a strong broadening. Thus, the very sharp boundaries of light scattering in backscatter for the embedded particle or the blocking angle for the embedded flake become much less sharp and changes in scattering amplitude are smoothed out over larger scattering angle ranges. This improves the chances of inclusion detection, although any specific signal peak amplitude may be less. In the case examined in Fig. 4.27, the probability of flake detection raises from 70% to about 85%.

5 Application of time-shift technique to colloidal drops

This chapter addresses the characterization of a colloidal drop using the time-shift technique to not only determine the drop size but also the volume concentration of the suspended colloidal particles inside, and possible even the size of the colloidal particles. This chapter begins with a description about how the volume concentration of the colloidal particles can be characterized. To validate this approach, corresponding experiments have been conducted.

5.1 Theory for the measurement of the volume concentration

Measurement of the volume concentration can be achieved using two approaches. The first approach is to evaluate the relative strength of the internal scattering from the colloidal particles compared to the reflection scattering from the drop. The second method is to evaluate the attenuation ratio of the signal from second-order refraction scattering based on the Lambert-Beer relation, similar as the method used in [42] [26] [27].

Evaluation of the relative strength of the internal scattering

For the first approach, the assumption is that, when the size of the host drop is constant, by changing the volume concentration of the colloidal particle the amplitude of the reflection from the time-shift signal remains constant. As the volume concentration of the colloidal particles increases, the scattering from the colloidal particles becomes stronger, which has also been mentioned in the study from Rosenkranz et al. [49].

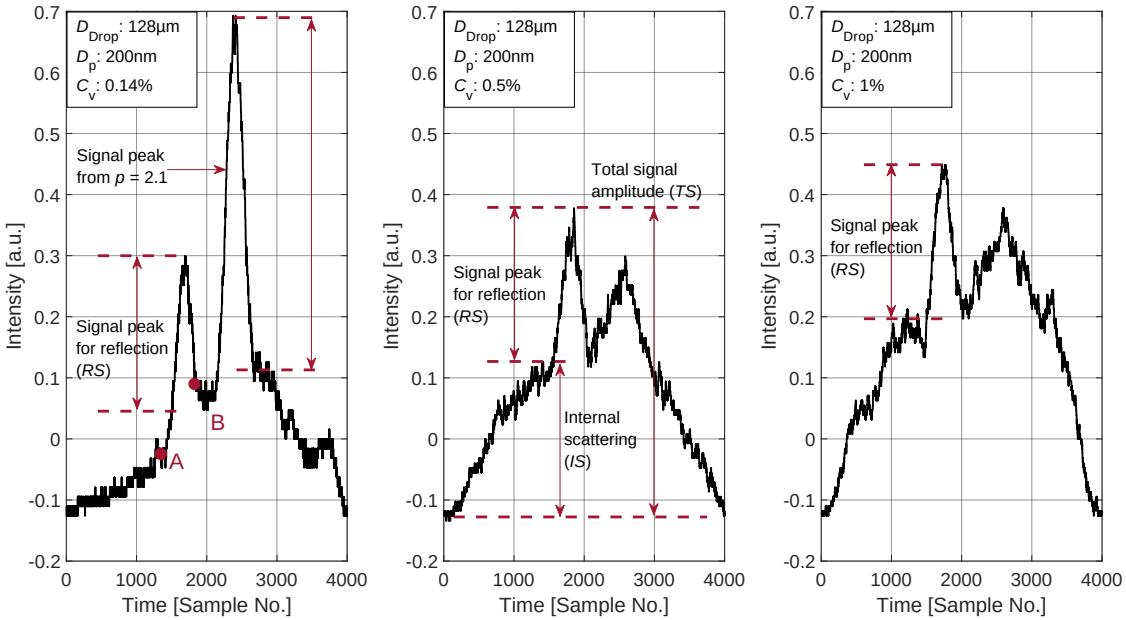

Figure 5.1: Comparison of measured and computed time-shift signals for different volume concentrations

Fig. 5.1 shows that as the volume concentration of the embedded nanoparticles increases from 0.14% to 1% , the scattering from the nanoparticle becomes stronger. It also indicates that for a colloidal drop with same size, by varying the volume concentration of the colloidal particles, the change of the amplitude of the signal peak for reflection scattering is very limited. Therefore, the amplitude of the signal peak for reflection scattering can be used as a reference to characterize changes in the strength of the internal scattering arising from the colloidal particles. Here the parameter η is defined to evaluate the relative to reflective scattering strength from the internal scattering as

$$\eta = \frac{TS - RS}{RS} = \frac{IS}{RS} \tag{5.1}$$

in which TS is the signal amplitude at the position for the reflection peak; IS is the amplitude from internal scattering by colloidal particles at the position of the reflection peak and RS is the reflection scattering amplitude from the drop surface, also at the position of the reflection peak. From the measured time-shift signal, TS can be directly measured; however, IS and RS cannot be directly measured. The amplitude for internal scattering is obtained by linear interpolation of the two values for points A and B by signal processing, as Fig. 5.2 depicts.

$$IS = \frac{I_A + I_B}{2} \tag{5.2}$$

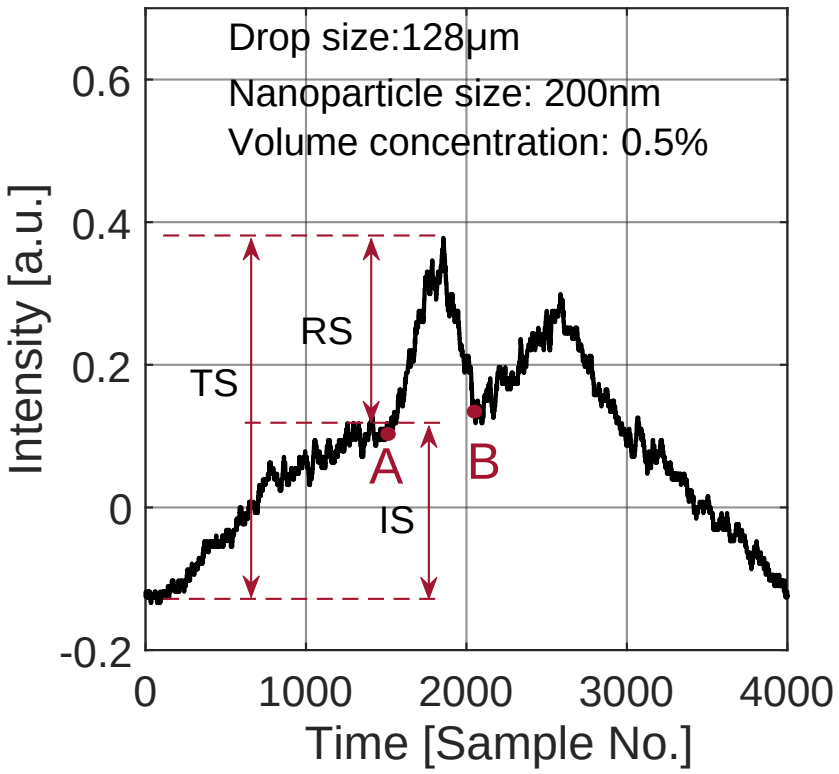

Figure 5.2: Scheme to obtain the intensity of the internal scattering from the measured signal by interpolation of the signal value between A and B.(TS: total signal strength; RS: signal strength from reflection; IS: signal strength from internal scattering)

By using the relative scattering strength of the inclusions to characterize the volume concentration, a lookup table for the theoretical value of η needs to be calculated before processing the signal. The measured η needs to be compared with the theoretical η to obtain the volume concentration

of the inclusions. However, the quantity η is related to the volume concentration of the inclusion as well as the size of the host drop. We assume that the inclusions within the colloidal drop will have very limited effect on the surface reflection, the calculation of the signal strength RS raised by surface reflection from a colloidal drop is replaced by calculation of the signal strength RS generated by surface reflection from a homogeneous spherical drop, having the same size as the colloidal drop. For the intersection with a homogeneous spherical particle, the amplitude of the signal peak from reflection scattering can be evaluated using the Debye series formulation of the Generalized Lorenz-Mie Theory (GLMT) [12]; it could also be calculated with geometric optics as written in section 4.2, but with less accuracy. The total signal strength TS could be obtained by using the formulation of the Discrete Dipole Approximation method in case of very small colloidal drops with high accuracy. When the size parameter of the colloidal drop is larger than 50, the computation effort will on longer be feasible. Both of the TS and RS could also be obtained by using the Monte Carlo ray-tracing method introduced in section 3.2, which needs much less time for computation. However, this method is less accurate compared to the discrete dipole approximation method.

Evaluation of the strength of the signal peak attenuation

Another method for estimating the colloidal concentration is by using the Lambert-Beer relation. Due to the inclusions, the signal modes $p = 2.1$ and $p = 2.2$ may be attenuated. Since the time-shift signal amplitude from the signal mode $p = 2.1$ is usually much stronger than the time-shift signal amplitude from the signal mode $p = 2.2$, only the signal mode $p = 2.1$ will be used to characterize the volume concentration of the inclusion. The attenuation of the signal amplitude from second-order refraction scattering satisfies the Lambert-Beer relation when the volume fraction of the inclusions is under 3% [29], according to Eq. (5.3).

$$I = I_0 \exp -\frac{OL}{E(L)} \tag{5.3}$$

in which I_0 is the time-shift signal amplitude of the signal mode $p = 2.1$ from a pure drop; I is the time-shift signal amplitude of the signal mode $p = 2.1$ from a colloidal drop, which has the same size as the pure drop; OL refers to the optical path length within the drop for second-order refraction scattering, as illustrated in Fig. 3.17 and $E(L)$ refers to the optical mean free path within the colloidal drop, which has been defined with the Eq. (3.37). The optical path length in a spherical drop for the time-shift signal mode $p = 2.1$ can be written as

$$OL = 4R \cdot \cos\left(\arcsin\left(\frac{\sin\theta_i^{p=2.1}}{m}\right)\right) \tag{5.4}$$

in which R is the radius of the drop; $\theta_i^{p=2.1}$ is the incident angle for second-order refraction scattering ($p = 2.1$) and can be obtained from

$$\sin\theta_i^{p=2.1} = m \cdot \sin\left(\frac{pi}{4} - \frac{\theta_S}{4} + \frac{\theta_i^{p=2.1}}{2}\right) \tag{5.5}$$

where θ_S is the polar angle for the detector. From Eqs. (3.30), (3.37), (5.3) and (5.4), the relationship between the volume concentration of the inclusions and the attenuation ratio of the signal from the second-order refraction scattering can be expressed as

$$C_v = -\frac{r \cdot \ln\frac{I}{I_0}}{3R \cdot Q_{ext} \cdot \cos\left(\arcsin\frac{\sin\theta_{p=2.1}}{m}\right)} \tag{5.6}$$

where r is the radius of the inclusions. By using the Lambert-Beer relation to estimate the volume concentration of the inclusions, the time-shift signal amplitude I of the signal mode $p = 2.1$ from colloidal drops needs to be evaluated from the measured time-shift signal; I_0 could be measured by using a pure liquid drop. It is unnecessary to measure the I_0 for different sizes of the pure drop. For other sizes of the drop, I_0 can be obtained by using the Generalized Lorenz-Mie theory.

The application range of this method is quite dependent on the optical properties and size of the colloidal particles. When the optical mean free path is small, as Eq. (5.3), the signal amplitude decays very quickly. To obtain I from the measured time-shift signal, the signal part contributed by the time-shift signal mode $p = 2.1$ needs to be extracted from the signal peak I_t, as shown in the right part of Fig. 5.3. As the volume concentration of the colloidal particles increases, then it will be impossible to distinguish between the signal amplitude arising from the internal scattering and second-order refraction scattering. As Eq. (3.37) [35] indicates, the optical mean free path is dependent on the volume concentration of the colloidal particles, the extinction efficiency factor, as well as on the size of the colloidal particle. The extinction efficiency factor is a function of incident wavelength and the size of the colloidal particles. For a particle with a small extinction efficiency factor, the optical mean free path could become very large. Therefore, even when the volume concentration of the colloidal particle is high, distinguishing the signal from the internal scattering and the second-order refraction scattering is still possible.

In Fig. 5.3 two time-shift signals from colloidal drops containing different sizes of nanoparticles are shown; the volume concentration is 10%; the inclusions are polystyrene latex nanoparticles. For the time-shift signal in the left part of the figure, the signal from second-order refraction scattering cannot be distinguished; however, the time-shift signal on the right part of the figure allows this. The reason is that the extinction efficiency factor of the nanoparticles with diameter 200 nm is 0.302, which is much larger than the extinction efficiency factor of the nanoparticles with the diameter 30 nm. Therefore, the optical mean free path is much smaller, which leads to a stronger attenuation of the signal from second-order refraction scattering.

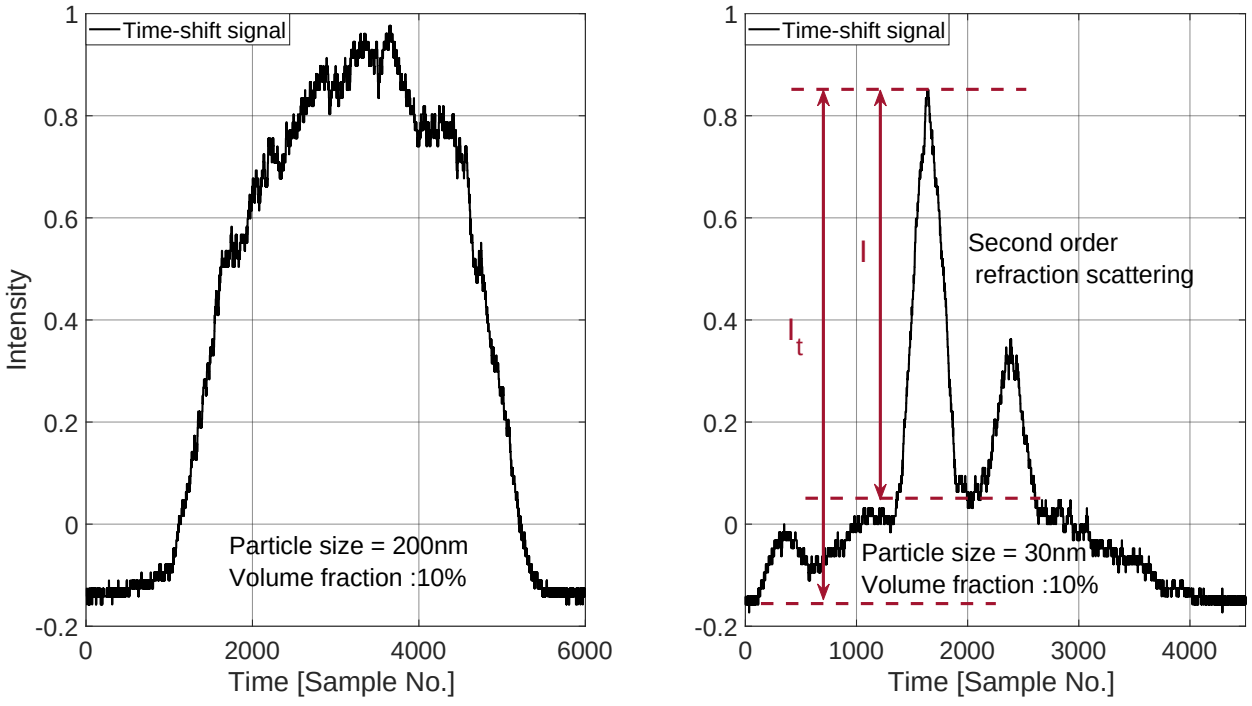

Figure 5.3: Comparison of time-shift signals from drops with different sizes of nanoparticles.

The measurement range of the time-shift technique using this approach for the volume concentration is estimated to be when the attenuation lies between 5% to 80%. When the attenuation is over 80%, it is difficult to distinguish between the scattering from the internal scattering and second-order refraction scattering. On the other hand, when the attenuation is too low (approx.<5 %.) then the level of internal scattering cannot be reliably distinguished from signal noise.

It is therefore instructive to examine under what conditions this range of attenuation (5% to 80%) can be expected. This is illustrated graphically in Fig. 5.4. In the left diagram of this figure, the allowable mean free path $E(L)$ resulting in a given attenuation ratio is shown. The mean free path $E(L)$ can then be used to yield a volume concentration, dependent on the radius of the embedded (polystyrene latex) nanoparticles and their extinction coefficient factor Q_{ext} (which itself is a function of r), according to the Lambert-Beer relation and assuming a drop diameter of 100 μm. This is expressed by re-arranging Eq. 3.37 as

$$C_v = \frac{4}{3E(L)} \cdot \frac{r}{Q_{ext}} \tag{5.7}$$

For a given size of colloidal particle, the factor r/Q_{ext} is fixed [36]. The relationship between the size of the polystyrene latex nanoparticle and r/Q_{ext} is plotted in the right diagram of Fig. 5.4. Fig. 5.5 shows the measurement range for different sizes of the polystyrene latex nanoparticle. The solid black line illustrates the upper range of the colloidal concentration and the dashed line presents the lower range. As the size of the particle increases, the measurement range decreases, however, the sensitivity to changes in volume concentration becomes higher.

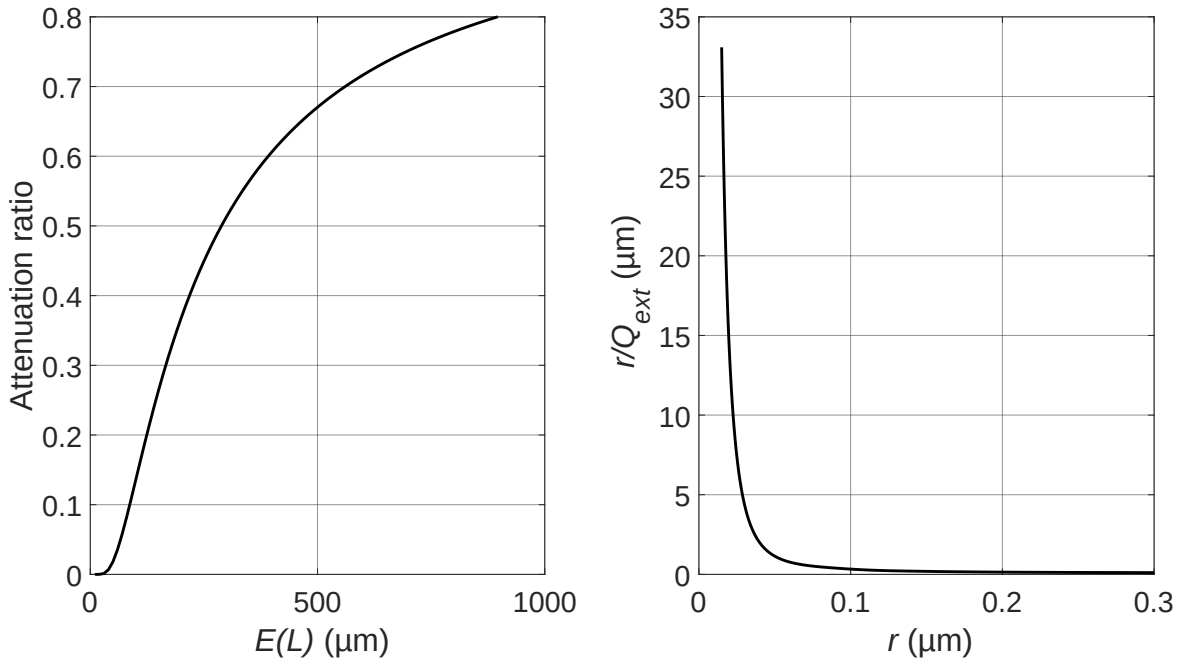

Figure 5.4: Parameters that affect the measurement range according to the Lambert-Beer relation and for a drop of 100 μm diameter.

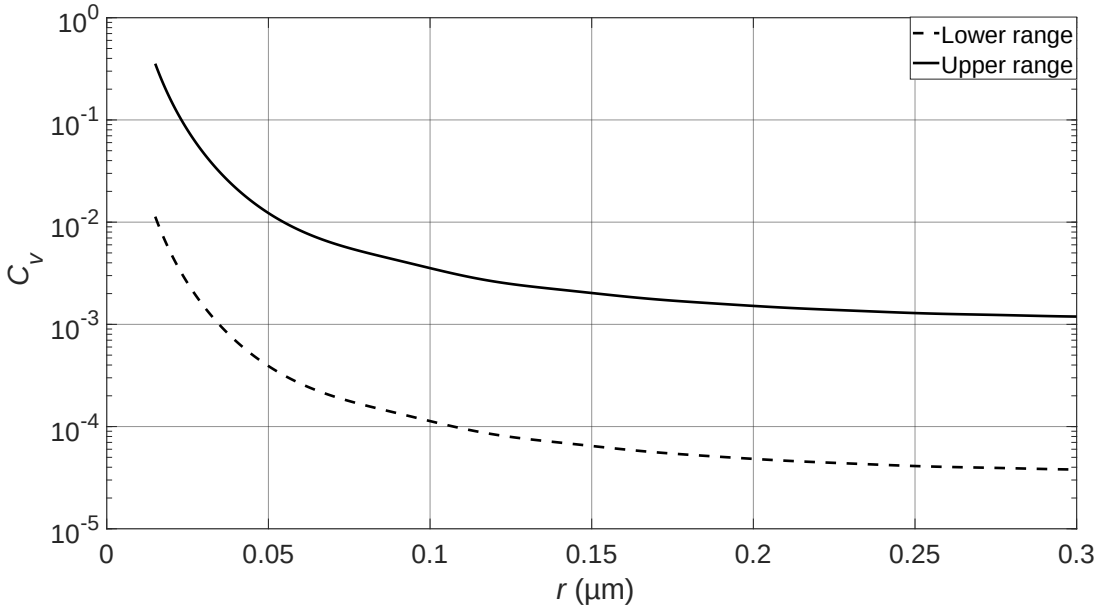

Figure 5.5: Measurement range for different sizes of polystyrene particles and for a drop of 100 μm diameter.

In Fig.5.5, the solid black line illustrates the upper range of the colloidal concentration and the dashed line presents the lower range. As the size of the particle increases, the measurement range decreases, however, the sensitivity to changes in volume concentration becomes higher. Given the above-mentioned pre-requisites to enable measurement of volume concentration, the optical mean free path can then be estimated. Knowing this value and the material of the colloidal particles, an estimate of the colloidal particle size can be made, assuming a monodispersed size distribution.

5.2 Experimental setup

Fig. 5.6 shows the experimental setup for acquiring time-shift signals from colloidal drops. Fig. 5.7 is a schematic illustration of the experimental setup. A drop generator (FMP GmbH) and syringe pump are used to generate a stable drop chain. A camera has been calibrated and used to capture the photographs of the drop chain; therefore, the drop size could be determined by counting the pixels of a single drop on the photograph. The size of the drop is controlled by changing the frequency of the function generator driving the drop generator, and the aperture of the drop generator. The raw time-shift signal is sampled with a Picoscope 6404D, 4 channel oscilloscope, which has a sampling rate of 500 MHz. For the time-shift instrument, the laser beam with an elliptical beam profile is used as the source; the detector is arranged in backscatter at the scattering angle 165°; the circular lens has the size of 25.4 mm, which covers a solid angle of 0.032 steradian; the distance between the measurement volume and the laser source is 125 mm, as well as the distance between the center of the lens and the measurement volume. The half-power beam width of the Gaussian beam is 1000 μm in the X axis; and the half-power beam width of the Gaussian beam is 8 μm in the Y axis.

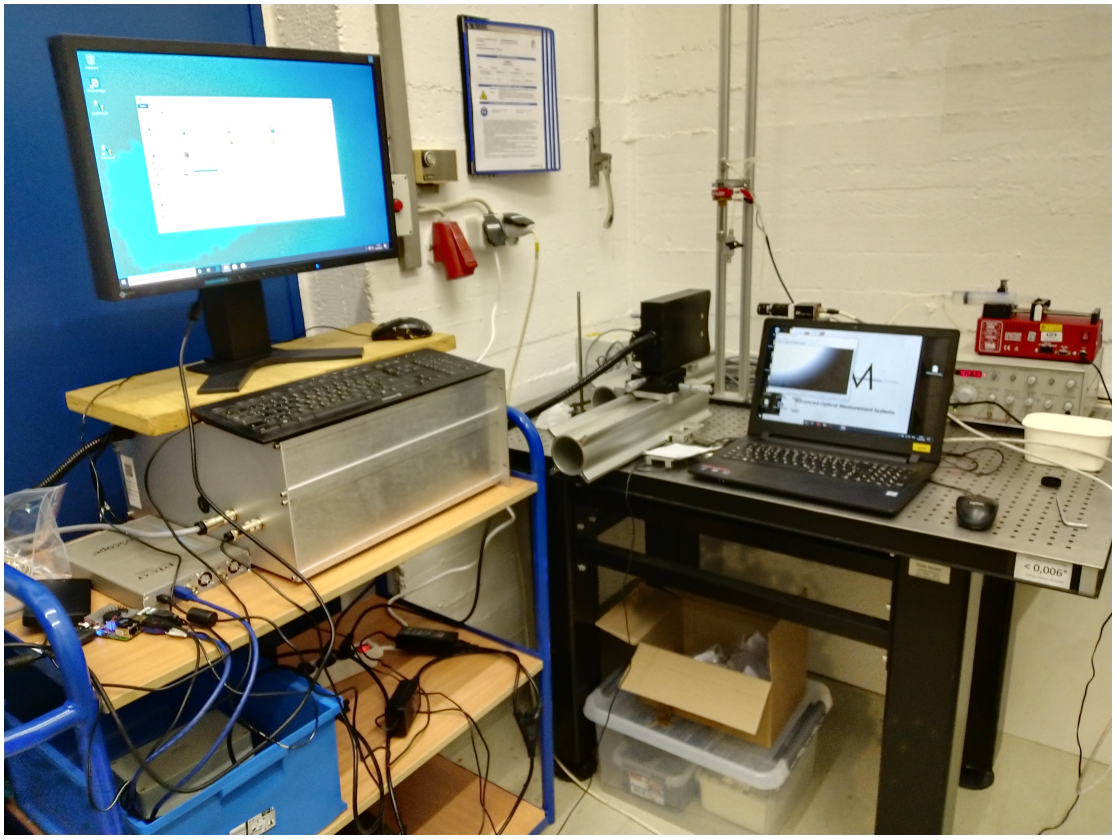

Figure 5.6: Experimental setup used to acquire time-shift signals from colloidal drops falling through a highly focused laser beam.

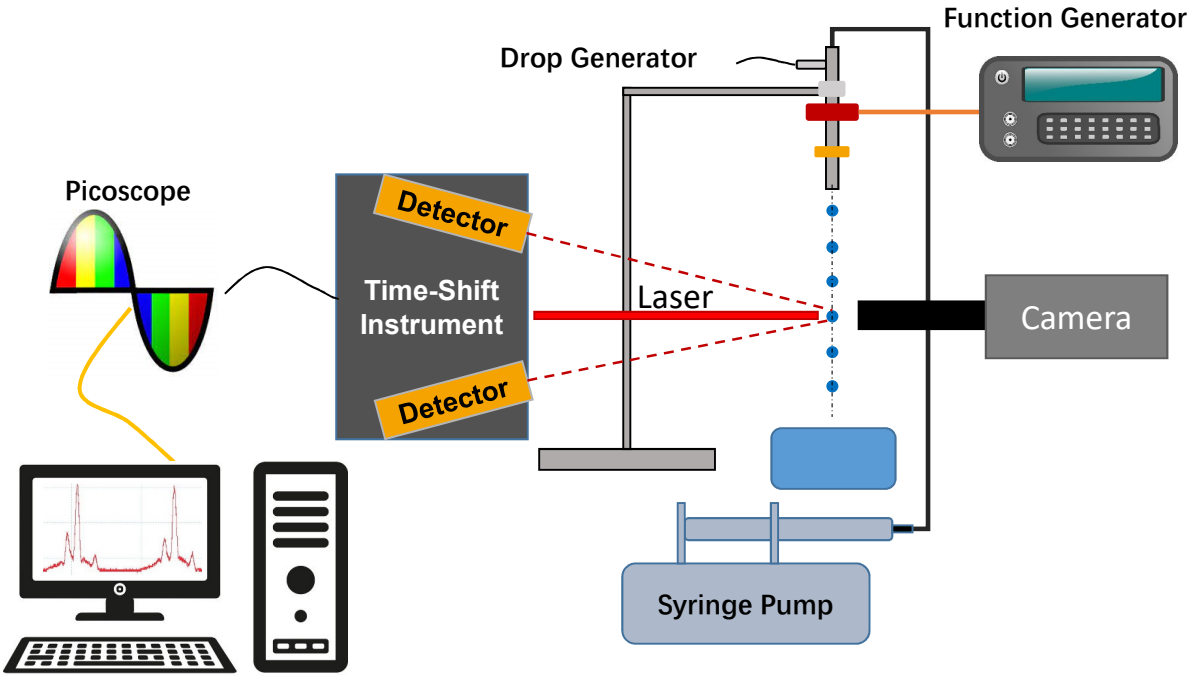

Figure 5.7: Schematic illustration of the experimental setup for measuring colloidal drops with the time-shift instrument

The particles in the colloidal drop are polystyrene latex nanoparticles, which are produced from the company Magsphere Inc. The polystyrene latex nanoparticles are diluted in water and have a volume fraction of 10%. The density of the polystyrene is very close to water, which avoids sedimentation. The polystyrene nanoparticles have a refractive index of 1.6268 for the laser wavelength of 405 nm; the relationship between the refractive index and the wavelength is given as

$$n^2 - 1 = \frac{1.4435\lambda^2}{\lambda^2 - 0.020216} \tag{5.8}$$

in which n refers to the refractive index and the λ is the wavelength. The nanoparticles available for experiments have the diameters 20 nm, 200 nm and 600 nm, as shown in the Fig. 5.8. The standard deviation of the particle size within one batch is 10%. Fig. 5.9 is an image of the 200 nm polystyrene latex nanoparticles acquired using transmission electron microscopy. The particle within the image are not strictly spherical; however, for subsequent simulations they are treated as spherical particles.

Figure 5.8: Nanoparticles from Magsphere with different sizes

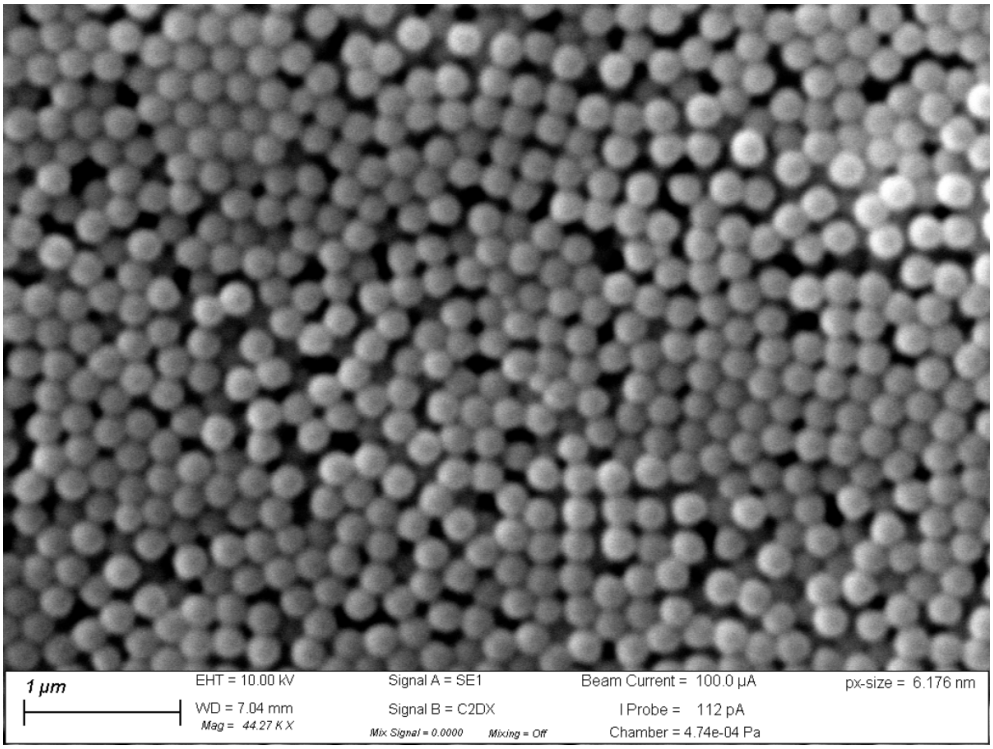

Figure 5.9: TEM image of 200 nm polystyrene latex nanoparticles

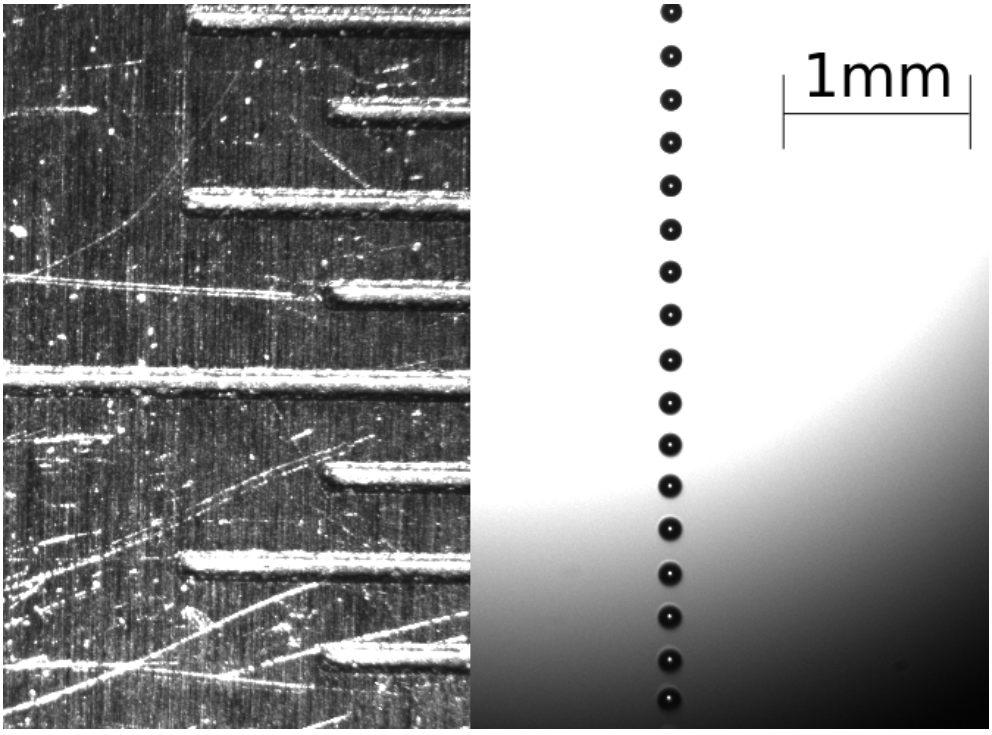

Figure 5.10: the left image is a ruler scale for calibration of the camera; the right part of the image shows the drop chain. Drop chain generated by the drop generator. The flow rate is 1.2 ml/min and the excitation frequency of the function generator is 20.31 kHz.

In Fig. 5.10, the left image is a ruler scale for calibration of the camera; the right part of the image shows the drop chain. The diameter d of the drops generated by the drop generator can be calculated using

$$d = (\frac{6 \cdot \dot{V}}{\pi \cdot f_G})^{1/3} \tag{5.9}$$

in which $\dot{V}$ is the volume flow rate and f_G is the excitation frequency of the function generator. The result is verified by comparing this computed value with the value obtained from direct imaging. By using Eq. (5.9), the diameter of the drop shown in the Fig. 5.10 is measured to be 123.4 μm; by using the imaging method the diameter is 125 μm. Therefore, the diameter of the drop given by Eq. (5.9) is reliable.

5.3 Results of experiment and simulations

Effect of the inclusion size to the time-shift signal

The time-shift signals were acquired for drops with different sizes of nanoparticles. The size of the nanoparticles has an strong effect on the time-shift signals, as Fig. 5.11 indicates. In Fig. 5.11, the black line represents the time-shift signal captured from a colloidal drop with 30 nm inclusions; the grey line is the time-shift signal captured from a colloidal drop with 200 nm inclusions. The volume fraction of the inclusions for both time-shift signals are 2% and the size of the host drops are 128 μm. As the size of the host drop is the same, the signal amplitude from the reflection scattering ($p = 0$) is the same. Meanwhile, a stronger scattering from the inclusion is observed for the inclusions with the size 200 nm, as well as a stronger attenuation of the time-shift signal amplitude for the signal mode $p = 2.1$.

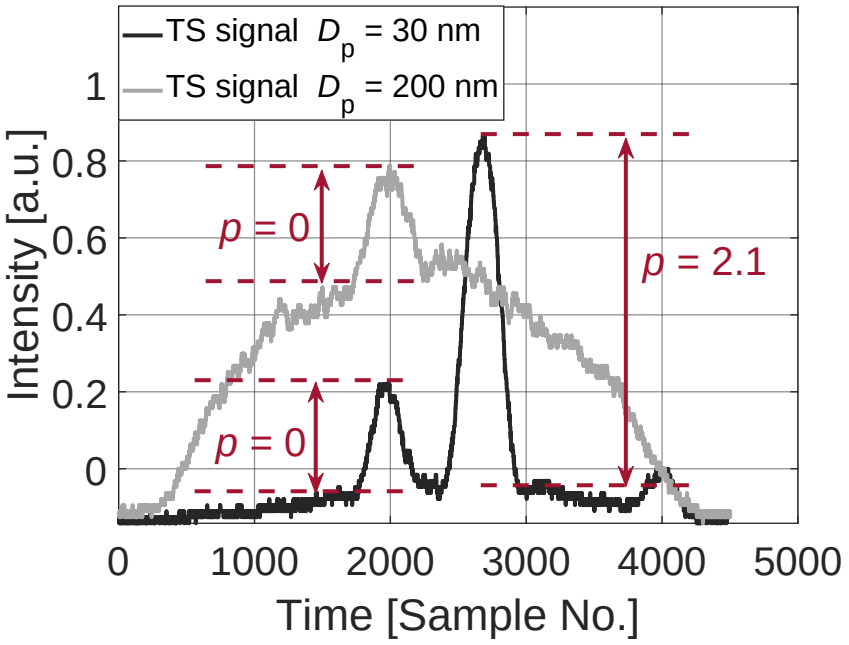

Figure 5.11: Comparison of the time-shift signal for different sizes of suspended colloidal particles. The diameter of the host drop (128 μm) and the concentration of the colloidal particles (2 %) is the same for both signals.

Measurement of the volume concentration of colloidal drops by signal attenuation

In Fig. 5.12 measured time-shift signals from colloidal drops with different volume concentration, varying from 0% to 10% are shown, when the size of the inclusions is 30 nm. The experimental conditions are listed in the Tab. 5.1. "Diameter of pinhole" refers to the size of the hole of the FMP drop generator; frequency refers to the frequency of the function generator.

Volume Fraction	Diameter of pinhole	Flow Rate	Frequency	Theoretical drop radius
0%	75 μm	1.3 ml/min	13.74 kHz	50.4 μm
2%	75 μm	1.3 ml/min	19.36 kHz	64.4 μm
5%	75 μm	1.3 ml/min	16.84 kHz	67.5 μm
10%	75 μm	1.3 ml/min	19.36 kHz	64.4 μm

Table 5.1: Experimental conditions from measuring the time-shift signals, when the size of the inclusions is 30 nm.

As Fig. 5.12 (b) and (d) present, when the volume fraction of the inclusions increases, the scattering from inclusions is stronger, and stronger attenuation of the time-shift signal amplitude from second-order refraction scattering can be observed. The time-shift signals in Fig. 5.12 (a) were acquired from pure water drops; however, the drop size is smaller compared with the drops in Fig. 5.12(b), (c) and (d), which can be recognized by comparing the peak distance of the individual time-shift signals.

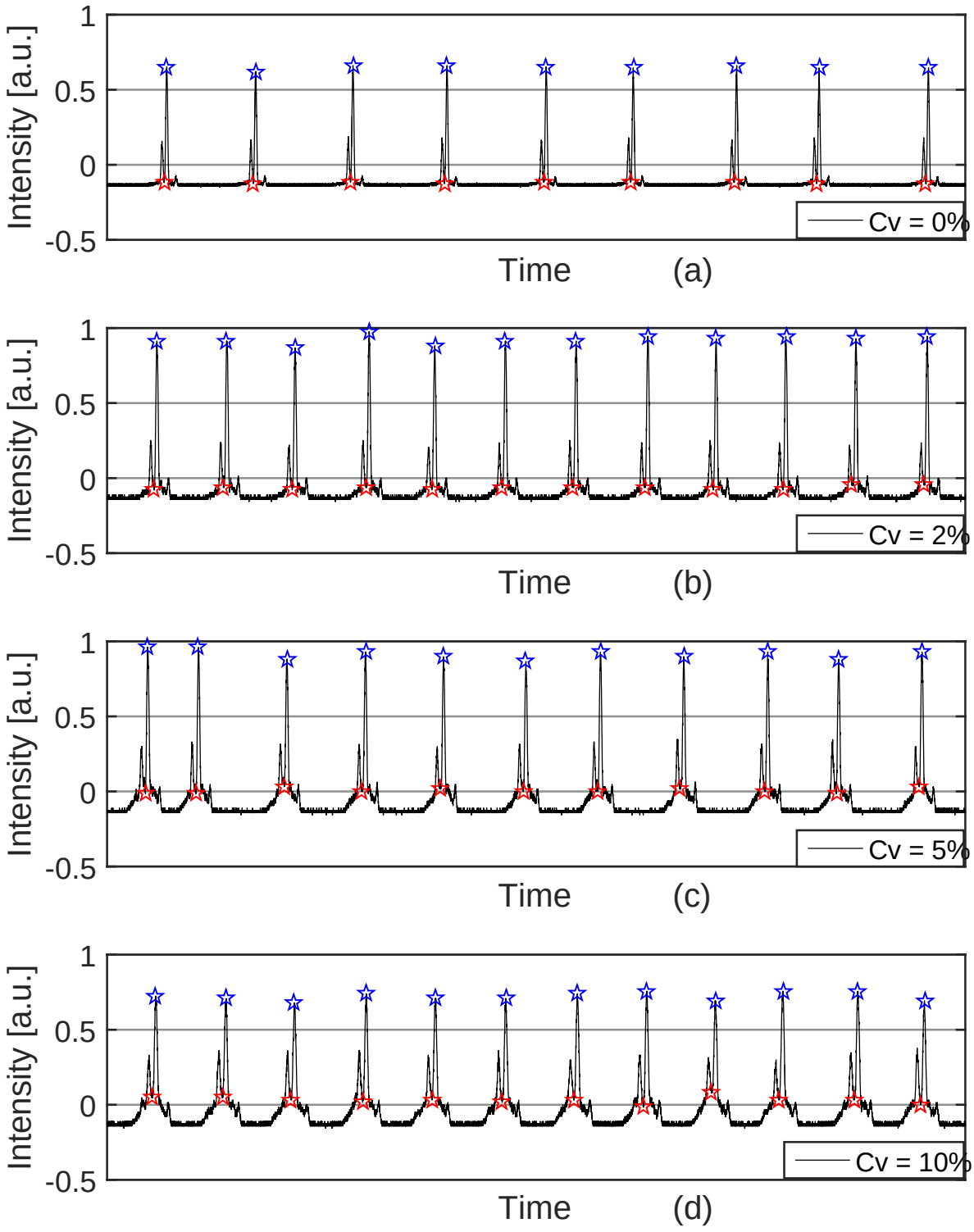

Figure 5.12: Comparison of the attenuation of second-order refraction scattering under conditions of different colloidal concentrations, ranging from 0 % to 10%. (diameter of colloidal particles = 30 nm; Cv: colloidal concentration)

For signal processing, the amplitude of the signal peak for the signal mode $p = 2.1$ needs to be evaluated from each of the measured time-shift signals. As Fig. 5.12 illustrates, the peak amplitudes of the time-shift signals fluctuate. Therefore, for the time-shift signals measured from colloidal drops with a certain volume concentration, after evaluation of the peak amplitude of the signal

mode $p = 2.1$ from each time-shift signal, a mean value is calculated to reduce the random error. For each time-shift signal, the peak amplitude for the signal mode $p = 2.1$ is obtained by the value at the point marked with blue star, subtracting the value at the point marked with red star, which represents the signal strength from the scattering of the inclusions.

After obtaining the peak amplitude for signal mode $p = 2.1$ for each volume concentration, the attenuation ratio can be calculated by comparing with the peak amplitude from that of a pure drop with the same size. As the measured time-shift signal in Fig. 5.12 (a) is measured for a pure liquid drop whose size is different from the drop size in Fig. 5.12 (b), (c) and (d), the peak amplitude $I(D_1)$ evaluated in Fig. 5.12 (a) needs to be converted to peak amplitude from the pure liquid drop whose size is the same as the colloidal drops. After that it can be used as a reference to calibrate the attenuation ratio of the peak amplitude from the colloidal drop. With the measured signal amplitude $I(D_1)$ from a pure liquid drop with diameter D_1, the signal amplitude $I(D_2)$ for a pure liquid drop with the diameter D_2 is obtained with Eq. (5.10).

$$I(D_2) = I(D_1) * \frac{P(D_2)}{P(D_1)} \tag{5.10}$$

where $P(D_1)$ and $P(D_2)$ can be calculated using the Eq. (4.21) in section 4.2.The average evaluated peak amplitude in Fig. 5.12 (a) is 0.7976. Using Eq. (5.10), the peak amplitudes for the pure water drops with the radii 64.4 μm and 67.5 μm are 1.1469 and 1.2168 respectively. The theoretical attenuation ratio for individual volume concentration is listed in Tab. 5.2.

C_v	$E(L)$	OL	Theoretical attenuation ratio	Measured at attenuation ratio
2%	2205 μm	252.7 μm	0.89	0.86
5%	882 μm	264.5 μm	0.74	0.74
10%	441 μm	252.7 μm	0.55	0.61

Table 5.2: Experimental results for evaluation of the attenuation ratio for different volume concentrations of the inclusions. (OL is the optical path length within the colloidal droplet for the signal mode $p = 2.1$, calculated with Eq. (5.4).)

The peak amplitude is evaluated for each measured time-shift signal from colloidal drops. The mean value is calculated with the individual evaluated peak amplitude for different volume concentrations of the inclusions. The results are illustrated in Fig. 5.13. The attenuation ratio can be evaluated by comparing this peak amplitude with the calculated peak amplitude from a pure liquid drop, as presented in Fig. 5.14. Substituting the measured value for the attenuation ratio in Eq. (5.6), the volume fraction of the inclusion can be estimated.

When the size of the inclusions are 200 nm and 600 nm, only for very low volume fractions of the inclusions could the signal mode $p = 2.1$ be evaluated. When the volume fraction is higher than 0.5%, the inclusions with diameter 200 nm and 600 nm have a much higher extinction efficiency factor Q_{ext} compared with Q_{ext} for 30 nm inclusions. The optical mean free path $E(L)$ is much smaller, which leads to strong attenuation of the peak amplitude for signal mode $p = 2.1$. The peak from signal mode $p = 2.1$ could not be distinguished from the signal arising from internal scattering, as the left part of the Fig. 5.3 illustrates. Therefore, the volume concentration cannot be estimated for these conditions.

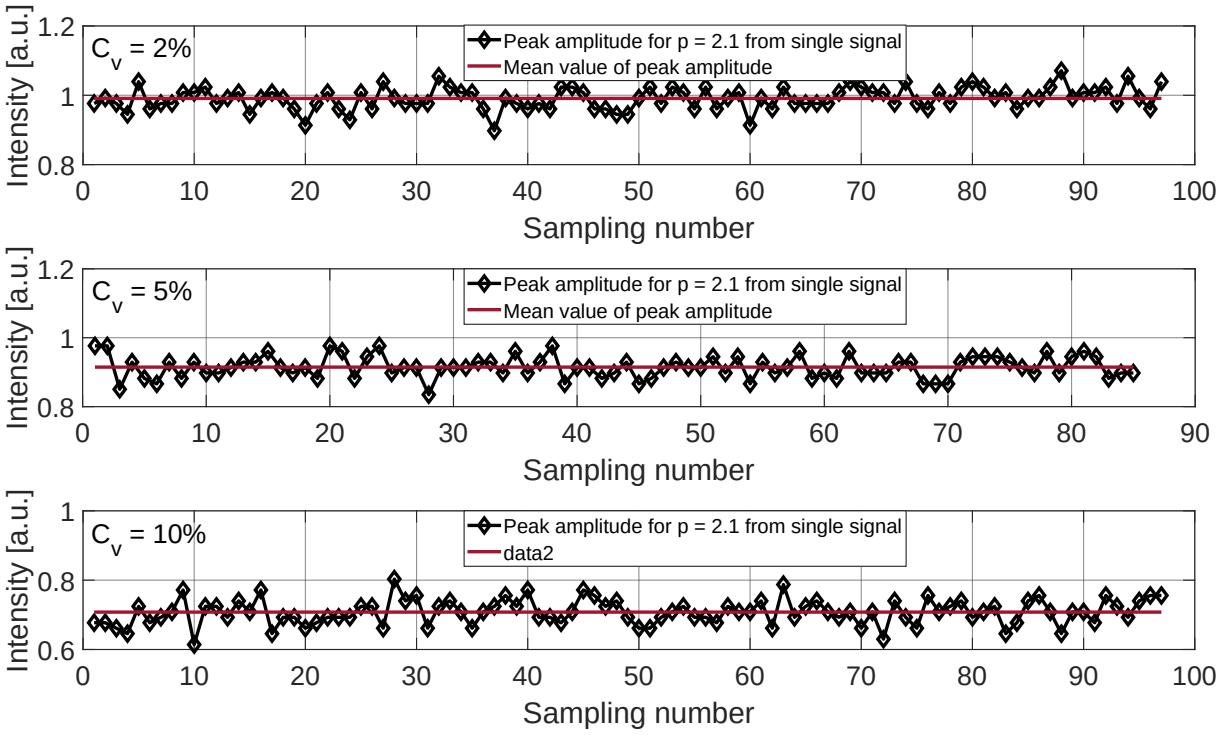

Figure 5.13: Evaluation of the peak amplitude for signal mode $p = 2.1$ of individual measured time-shift signal from the colloidal drops. The volume fraction C_v varies from 2% to 10%.

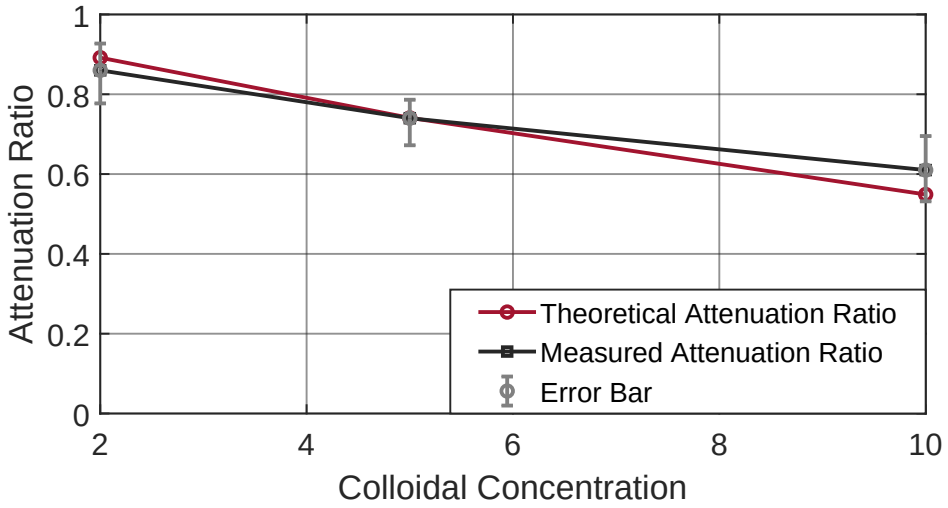

Figure 5.14: Comparison of the measured and theoretical attenuation ratio of the peak amplitude for sigal mode $p = 2.1$.

Measurement of volume concentration of inclusions with the strength of internal scattering

For the measured time-shift signals, the volume concentration of the inclusions can also be estimated using the strength of the internal scattering from the inclusions within the drop. The size of the colloidal drop can be determined by using the time-shift technique, as before. With the Monte Carlo ray-tracing method in section 3.2, the theoretical relative scattering strength η_t can be simulated

for different volume concentrations of the inclusions. The quantity η_m will be evaluated from the measured time-shift signals. The estimation of the volume concentration is achieved by comparing η_t with η_m.

The experimental conditions for measuring the colloidal drops with 200 nm inclusions are listed in Tab. 5.3. The flow rate of the syringe pump and the frequency of the function generator are kept constant, yielding colloidal drops with uniform size.

C_v	Diameter of pinhole	Flow Rate	Frequency	Theoretical drop size
0.14%	75 μm	1.3 ml/min	19.36 kHz	64.4 μm
1%	75 μm	1.3 ml/min	19.36 kHz	64.4 μm
2%	75 μm	1.3 ml/min	19.36 kHz	64.4 μm
5%	75 μm	1.3 ml/min	19.36 kHz	64.4 μm

Table 5.3: The experimental conditions for measuring the colloidal drops with 200 nm inclusions. The volume concentration of the colloidal drop varies from 0.14% to 5%.

To validate the Monte Carlo ray-tracing code, the simulated time-shift signals have been compared with the measured time-shift signals from a pure water drop and colloidal water drops with different volume fractions. Fig. 5.15 presents the comparison between the simulated and measured time-shift signal from a pure water drop. In Figs. 5.16 - 5.19 the comparisons between the simulated and measured time-shift signal from colloidal drops with different volume concentrations are shown, varying from 0.14% to 5%. The overall agreement between the simulated and the measured time-shift signals is satisfactory.

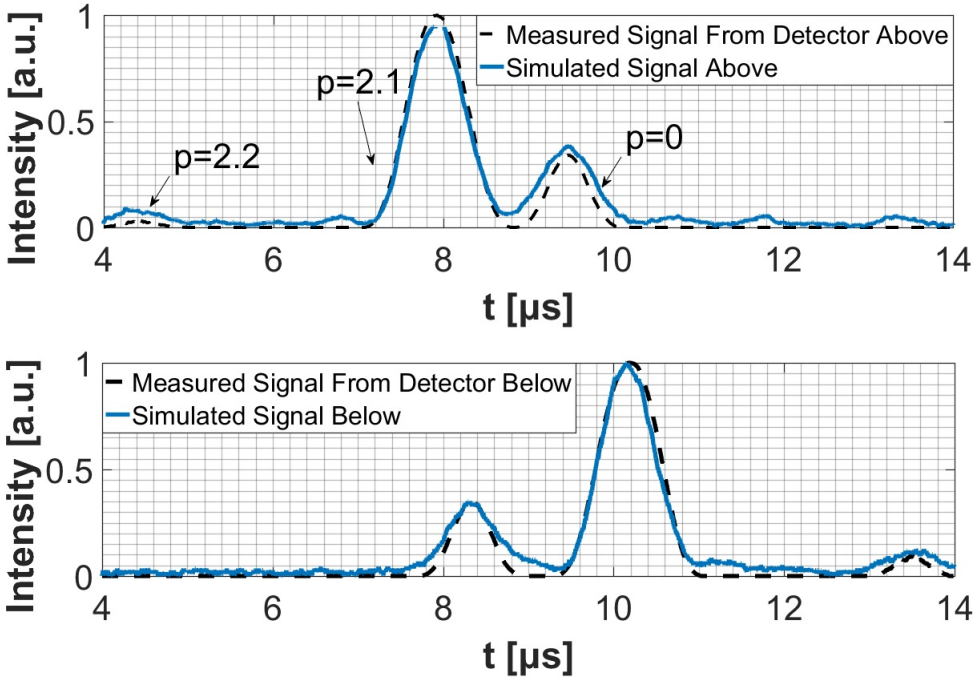

Figure 5.15: Comparison between a simulated time-shift signal and a measured time-shift signal for a pure water drop with the diameter 120 μm. (scattering angle θ_s=165°, wavelength of the laser beam is 405 nm, refractive index of drop is 1.3431, polarization state of the laser beam is parallel polarized.) Reproduced from [28].

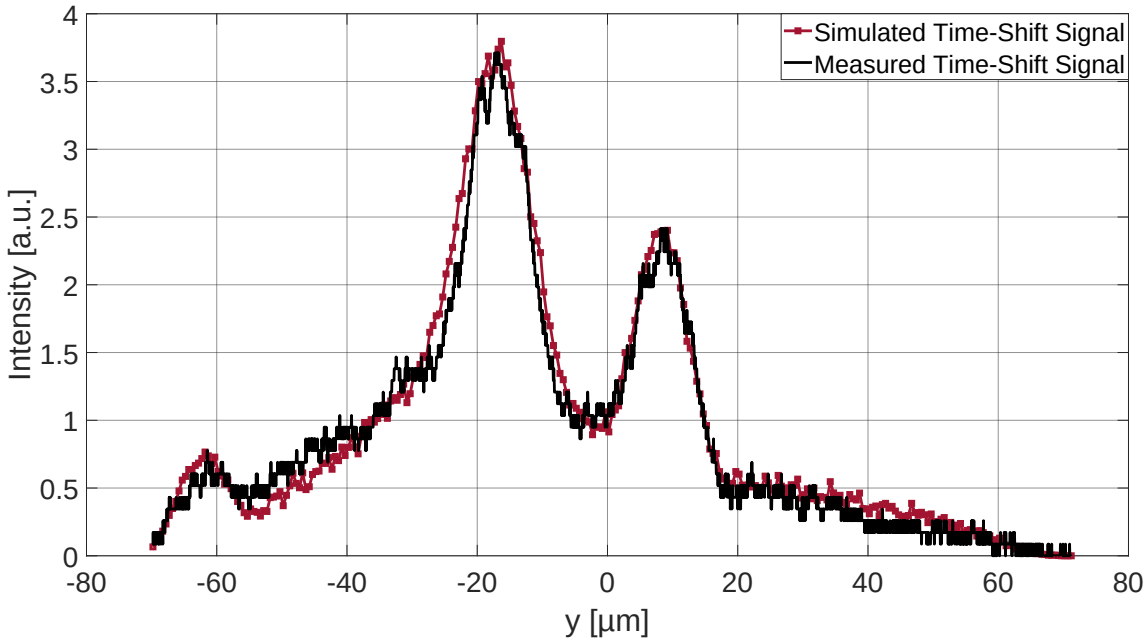

Figure 5.16: Comparison between the measured and simulated time-shift signals. (drop size: 127 μm, refractive index drop:1.3431, refractive index of inclusion: 1.6268, inclusion size: 200 nm, wavelength of laser beam: 405 nm, volume concentration 0.14%

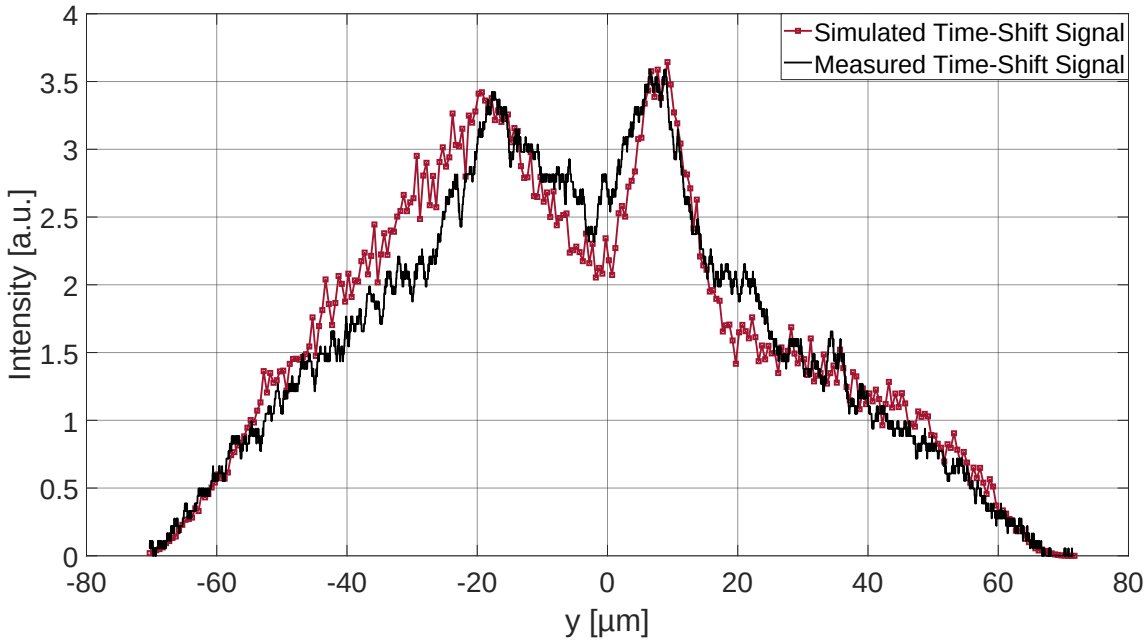

Figure 5.17: Comparison between the measured and simulated time-shift signals (drop size: 128 μm, refractive index drop:1.3431, refractive index of inclusion: 1.6268, inclusion size: 200 nm, wavelength of laser beam: 405 nm, volume concentration 0.50%

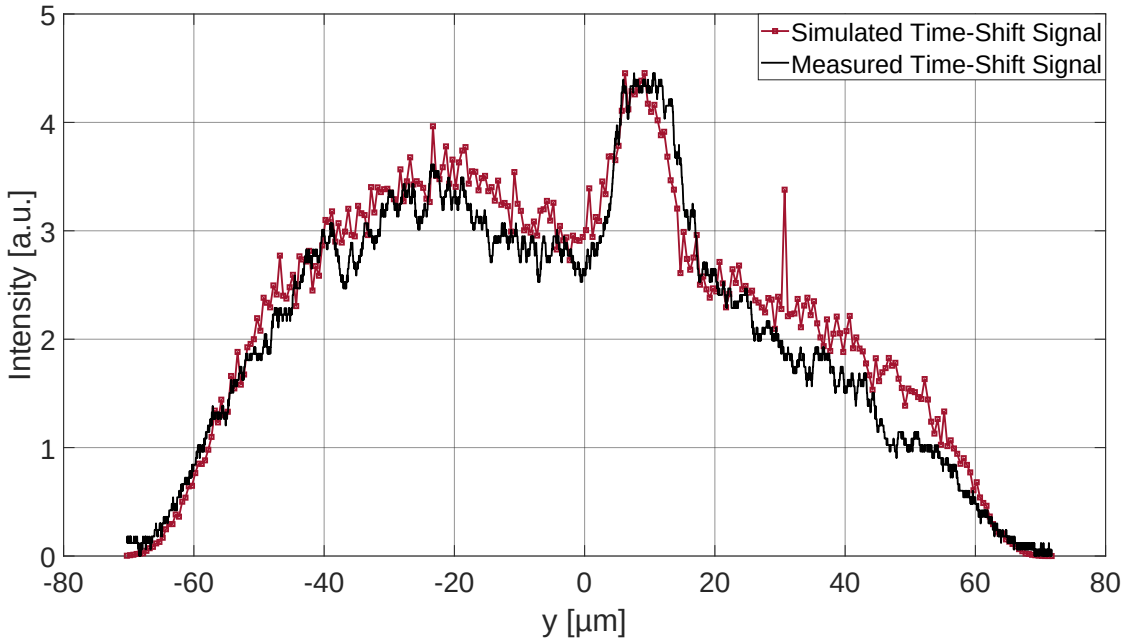

Figure 5.18: Comparison between the measured and simulated time-shift signals (drop size: 128 μm, refractive index drop:1.3431, refractive index of inclusion: 1.6268, inclusion size: 200 nm, wavelength of laser beam: 405 nm, volume concentration 1%

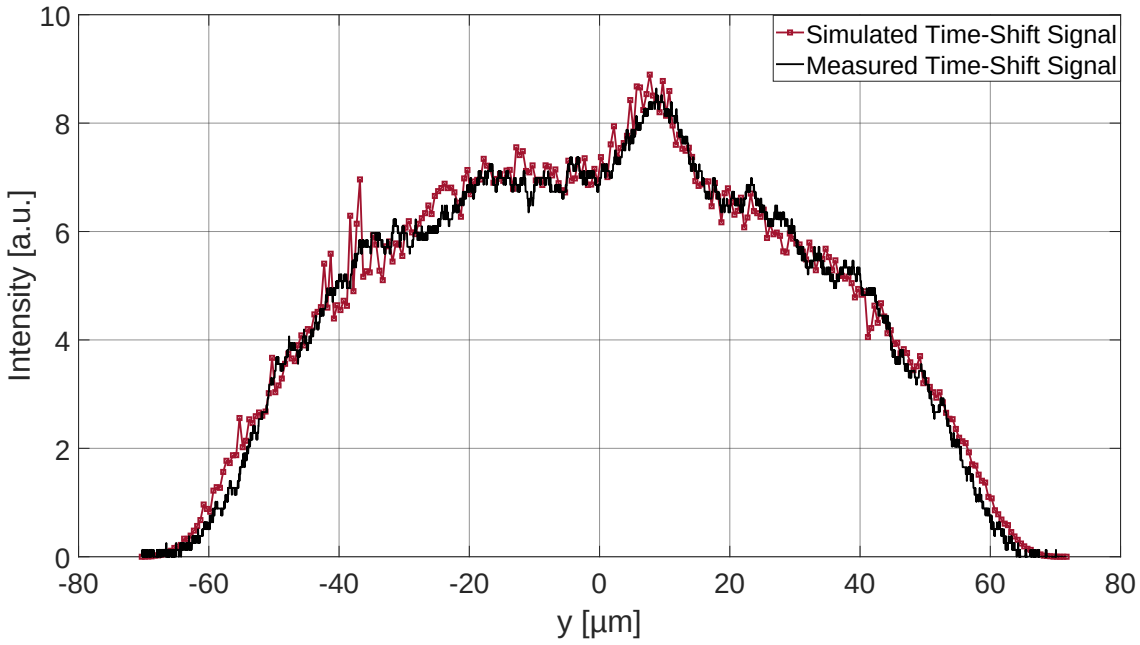

Figure 5.19: Comparison between the measured and simulated time-shift signals (drop size: 128 μm, refractive index drop:1.3431, refractive index of inclusion: 1.6268, inclusion size: 200 nm, wavelength of laser beam: 405 nm, volume concentration 5%

Figure 5.20 shows the measured time-shift signals. Similar to the measured time-shift signals in Fig. 5.12, the scattering strength from the inclusions is stable; however, the peak amplitude fluctuates. Possible reasons for this fluctuation can be slight fluctuations of the sphericity of the

host drop and small fluctuations of the drop trajectory through the measurement volume. The signal strength from the internal scattering becomes stronger as the volume concentration of the inclusions increases.

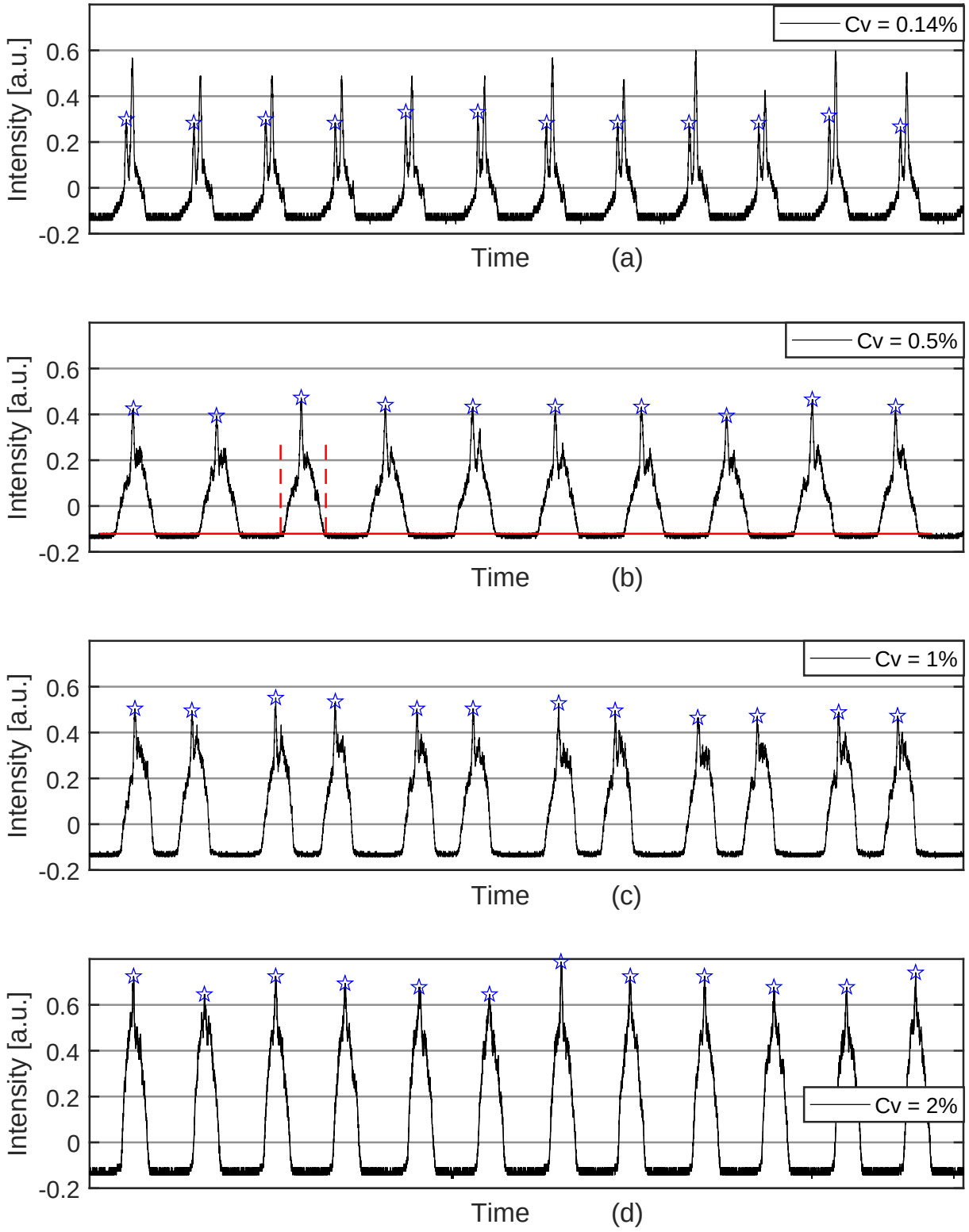

Figure 5.20: Measured time-shift signals from drops with different colloidal concentrations ranging from 0.14 % to 2%. (diameter of colloidal particles = 200nm; Cv: colloidal concentration)

In Fig. 5.20 the points marked with a blue star are the positions where the signal peak for reflection scattering occurs. The signal value at these points is the total signal strength, which combines the scattered signal from the host drop surface and the scattered signal from the inclusions. For signal processing, individual time-shift signals need to be extracted from the signal train, which can be realized by setting a threshold for the signal value, as illustrated in the second part of Fig. 5.20. The scattered signal from the reflection scattering and the signal from the inclusions need to be separated, in order to evaluate the relative scattering strength η of the inclusions, as illustrated in Fig. 5.2. Determining the position for the reflection peak is relatively straight-forward; extracting the starting and ending positions of the reflection peak, which are marked as A and B in Fig. 5.2, is more challenging.

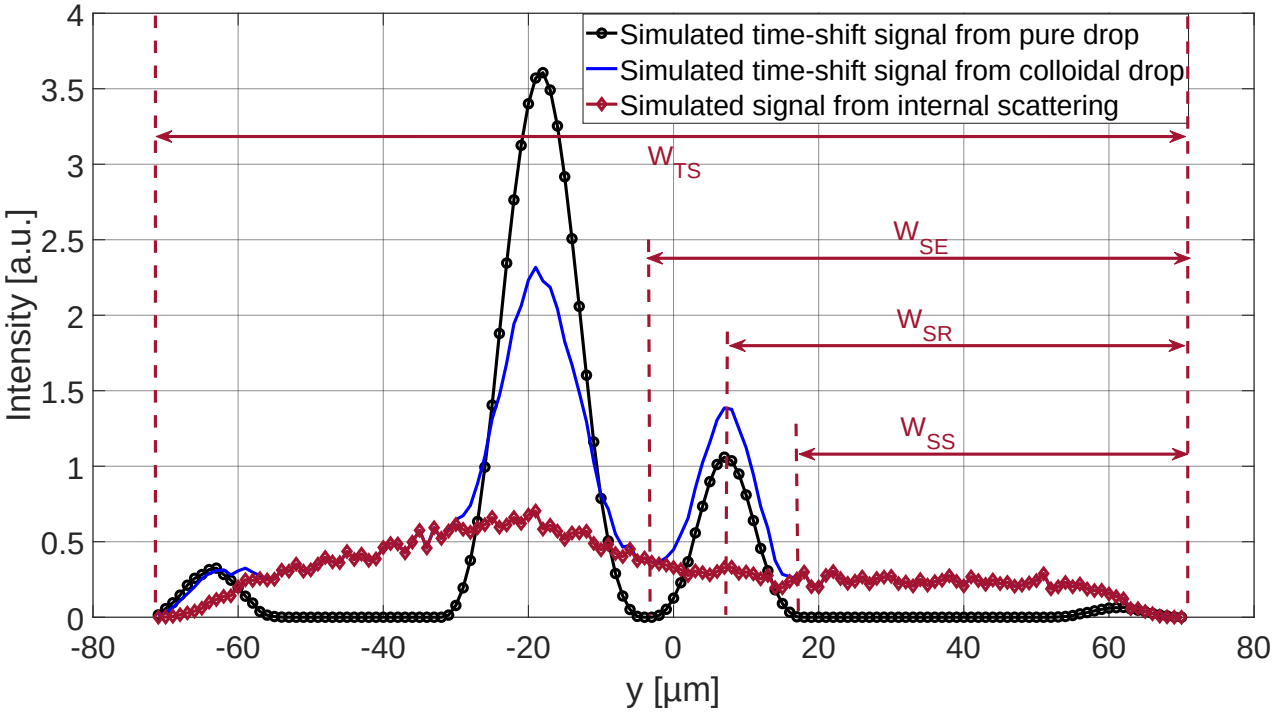

Figure 5.21: Determination of the positions for the reflection peak start, maximal value and end point.

The beam waist ω_y in the Y axis is given and the size of the drop can be measured with the time-shift instrument. In Fig. 5.21, W_{TS} is the moving distance of the drop within the duration of the time-shift signal; W_{SS} is the displacement from the instant when the time-shift signal starts to the instant at which the reflection peak begins; W_{SR} is the displacement from the instant when the time-shift signal starts to the instant at which the maximum value of the reflection peak occurs; W_{SE} is the displacement from instant when the time-shift signal starts to the instant at which the reflection peak ends. When the drop has a speed of v, the duration of the entire time-shift signal t_{TS} is expressed as

$$t_{TS} = \frac{W_{TS}}{v} = \frac{2R + 2 * \omega_y}{v} \tag{5.11}$$

The duration from the start of the time-shift signal to the start of the reflection peak is written as

$$t_{SS} = \frac{W_{SS}}{v} = \frac{R * (1 - \sin 10.4°)}{v} \tag{5.12}$$

The duration from the start of the time-shift signal to the end of the reflection peak is given as

$$t_{SE} = \frac{W_{SE}}{v} = \frac{R * (1 - \sin 4.6°) + 2 * \omega_y}{v} \tag{5.13}$$

The duration from the start of the time-shift signal to the maximum value of the reflection peak is formulated as

$$t_{SR} = \frac{W_{SR}}{v} = \frac{R * (1 - \sin 7.5^\circ) + \omega_y}{v} \tag{5.14}$$

The sampling rate of the signal is assumed to be constant throughout the entire signal. If within the time t_{TS} the number of data points sample is N_{TS}, then within the time t_{SS}, the number of the sampled data points N_{SS} can be obtained with

$$N_{SS} = N_{TS} * \frac{R * (1 - \sin 10.4^\circ)}{2R + 2 * \omega_y} \tag{5.15}$$

Then for the array built with the N_{TS} data points, the N_{SS}th value of the array should be the signal strength at the starting point of the reflection peak. The signal strength at the ending point of the reflection peak can be found in a similar manner, as well as the signal strength at the maximal value of the reflection peak. Then the relative scattering strength η for individual measured time-shift signal can be evaluated by using the Eq. (5.1). The value of η has been evaluated from the measured time-shift signals at different volume concentrations, the results is illustrated in Fig. 5.22, in which the black circles represent the value of η for individual measured time-shift signals. For certain volume concentrations of the inclusions, a mean value is calculated, which is plotted as the red line in Fig. 5.22. The η value has been simulated with the Monte-Carlo ray-tracing method for different volume concentration, and the simulated η has been compared with the mean value of η from the measurement. The comparison is presented in Fig. 5.23. From this comparison, it appears that this approach is a feasible method to characterize the volume concentration of the inclusions by evaluation of the relative scattering strength from the time-shift signal.

Nonetheless, the standard deviation shown in this figure is significant and increases with volume concentration of colloidal particles in the drop. From the definition of η (Eq. (5.1)), it is clear that even if the reflective scattering amplitude exhibits little variation, any variations or uncertainties in the determination of the internal scattering amplitude will immediately contribute to the standard deviation depicted in Fig. 5.23; For the same fluctuation level of reflective scattering, higher internal scattering will lead to a larger deviation of η; this is the main reason that for higher volume concentrations, a larger standard deviation is observed. Variations of the internal scattering amplitude can arise physically, for instance through colloidal aggregates, which not only alter the internal scattering, but may also influence the sphericity of the drop [22]. However, also the uncertainty in estimating the internal scattering amplitude increases, since the signal noise (shot noise) will be Poisson distributed; hence, increase with amplitude. Further remarks concerning the influence of colloidal particle size on the internal scattering will be made below.

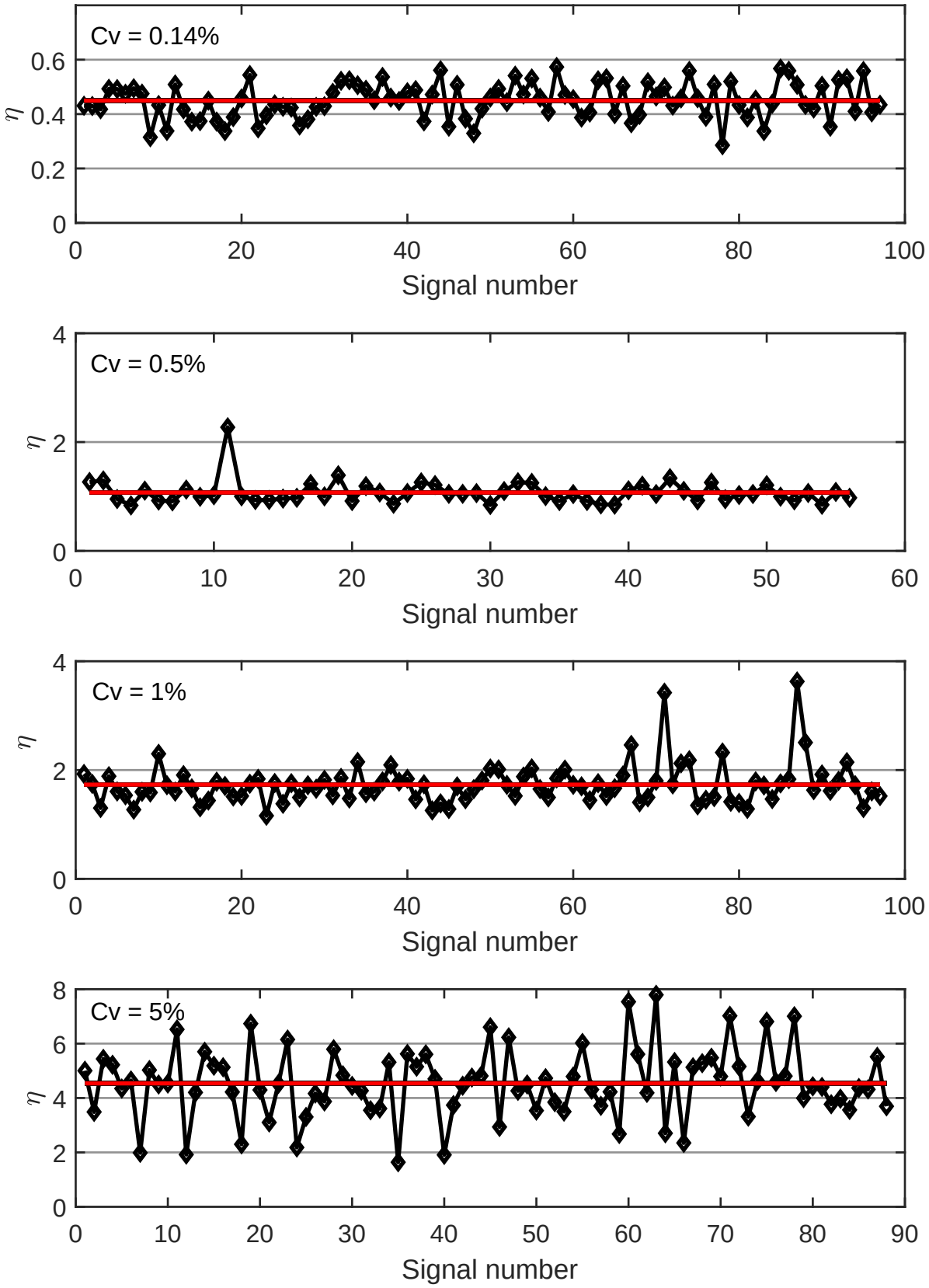

Figure 5.22: Evaluation of relative scattering strength η from individual measured time-shift signal for different colloidal concentration.

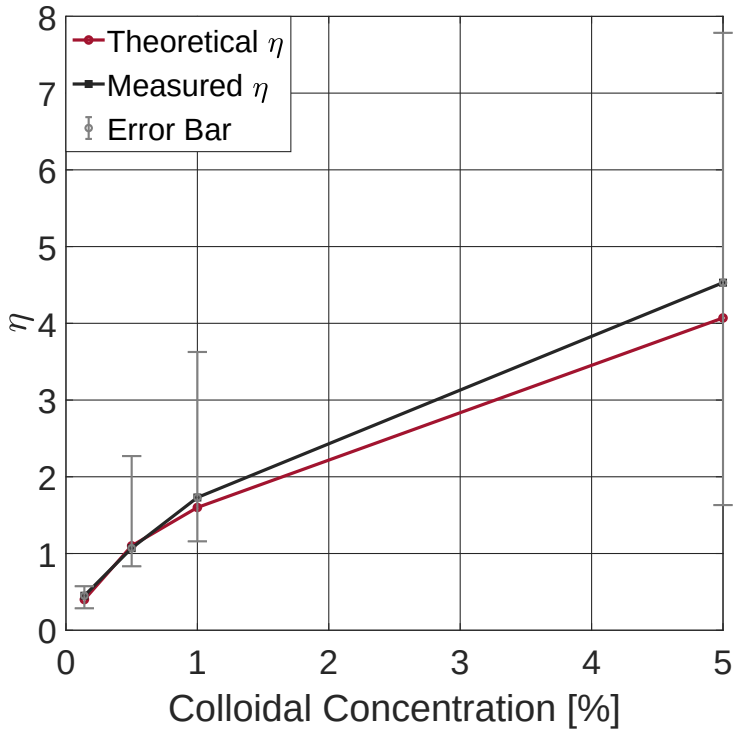

Figure 5.23: Comparison between the measured η and simulated η for different volume concentrations of the colloidal particles

For a drop with a given size, the volume concentration of colloidal particles is characterized by comparing the measured η value with the simulated η value. As the volume concentration of the particle increases, the optical mean free path $E(L)$ will decrease, which leads to more interactions between the inclusions and the light rays. However, the simulation time using the Monte-Carlo ray-tracing method will also increase. Therefore, when $\eta_{C_{v1}}$ is simulated for a host drop size D_1 , but for higher volume concentrations C_{v2}, it is advantageous to use the Generalized Lorenz-Mie theory and the effective medium theory to estimate the η_2 to reduce the computational effort. For a volume concentration C_{v1}, the $\eta_{C_{v1}}$ for the host drop size D_1 is formulated as

$$\eta_{C_{v1}} = \frac{TS_{C_{v1}} - RS_{C_{v1}}}{RS_{C_{v1}}} = \frac{IS_{C_{v1}}}{RS_{C_{v1}}} \tag{5.16}$$

in which $TS_{C_{v1}}$ is the total signal strength and $RS_{C_{v1}}$ is the signal strength from the reflection scattering. Both of these values are obtained with the Monte-Carlo ray-tracing method. Using the effective medium theory for colloidal drop, the effective dielectric constant ϵ_{eff_1} and ϵ_{eff_2} are calculated for the volume concentrations C_{v1} and C_{v2} respectively with the Eq. (5.17).

$$\frac{\epsilon_{eff} - \epsilon_m}{\epsilon_{eff} + 2\epsilon_m} = \delta_{inc} \frac{\epsilon_{inc} - \epsilon_m}{\epsilon_{inc} + 2\epsilon_m} \tag{5.17}$$

$$n_{eff} = \sqrt{\epsilon_{eff} \cdot \mu} \tag{5.18}$$

in which ϵ_{eff} is the effective dielectric constant of the medium; ϵ_{inc} is the dielectric constant of the inclusions; ϵ_m is the dielectric constant of the medium; δ_{inc} is the volume fraction of the inclusions. Using the GLMT method to calculate the total signal strength TS_{eff_1} and TS_{eff_2} for a homogeneous spherical particle for the refractive index n_{eff_1} and n_{eff_2} respectively. Then the relative scattering

strength $\eta_{C_{v2}}$ is estimated with Eq. (5.19).

$$\eta_{C_{v2}} = \frac{TS_{C_{v1}} * \frac{TS_{eff_1}}{TS_{eff_2}} - RS_{C_{v1}}}{RS_{C_{v1}}} \tag{5.19}$$

5.3.1 Calculation of the size of the colloidal particles

When the volume concentration C_v of the colloidal drop is given, the size of inclusions can also be measured indirectly by evaluating the attenuation ratio of the time-shift signal. Eq. (3.37) can be rewritten as

$$\frac{Q_{ext}(r)}{r} = \frac{4}{3E(L) \cdot C_v} \tag{5.20}$$

The optical mean free path $E(L)$ can then be obtained using Eq. (5.21), by evaluating the attenuation ratio of the signal from second-order refraction scattering.

$$E(L) = \frac{-4R \cdot \cos\left(\arcsin\frac{\sin\theta_{p=2.1}}{m}\right)}{\ln\frac{I}{I_0}} \tag{5.21}$$

in which R is the radius of the colloidal drop and can be measured with the time-shift instrument, $\theta_{p=2.1}$ is the incident angle for the time-shift signal mode $p = 2.1$, computed using Eq. (5.5). Substituting the Eq. (5.21) into Eq. (5.20), Eq. (5.22) can be obtained.

$$\frac{Q_{ext}(r)}{r} = \frac{-\ln\frac{I}{I_0}}{3R \cdot \cos\left(\arcsin\frac{\sin\theta_{p=2.1}}{m}\right) \cdot C_v} \tag{5.22}$$

From the measured time-shift signal from a colloidal drop, the right part of the Eq. (5.22) can be evaluated. The relationship between the $\frac{Q_{ext}(r)}{r}$ and the radius of the particle is obtained by using the Lorenz-Mie theory. The extinction cross-section is given as Eq. (5.23) [5].

$$C_{ext} = \frac{2\pi}{k^2}\sum_{n=1}^{\infty}(2n+1)Re(a_n + b_n) \tag{5.23}$$

in which k refers to the wave number; a_n and b_n are the scattering coefficients, which can be calculated using Eqs. (2.17) and (2.18). The relationship between the extinction cross-section C_{ext} and the extinction coefficient factor $Q_{ext}(r)$ is expressed as

$$C_{ext} = Q_{ext}(r) * \pi * r^2. \tag{5.24}$$

Then the $\frac{Q_{ext}(r)}{r}$ can be formulated as

$$\frac{Q_{ext}(r)}{r} = \frac{2}{k^2 \cdot r^2}\sum_{n=1}^{\infty}(2n+1)Re(a_n + b_n) \tag{5.25}$$

Figure 5.24 shows the relationship between $\frac{Q_{ext}(r)}{r}$ and the radius r of the polystyrene latex particle.

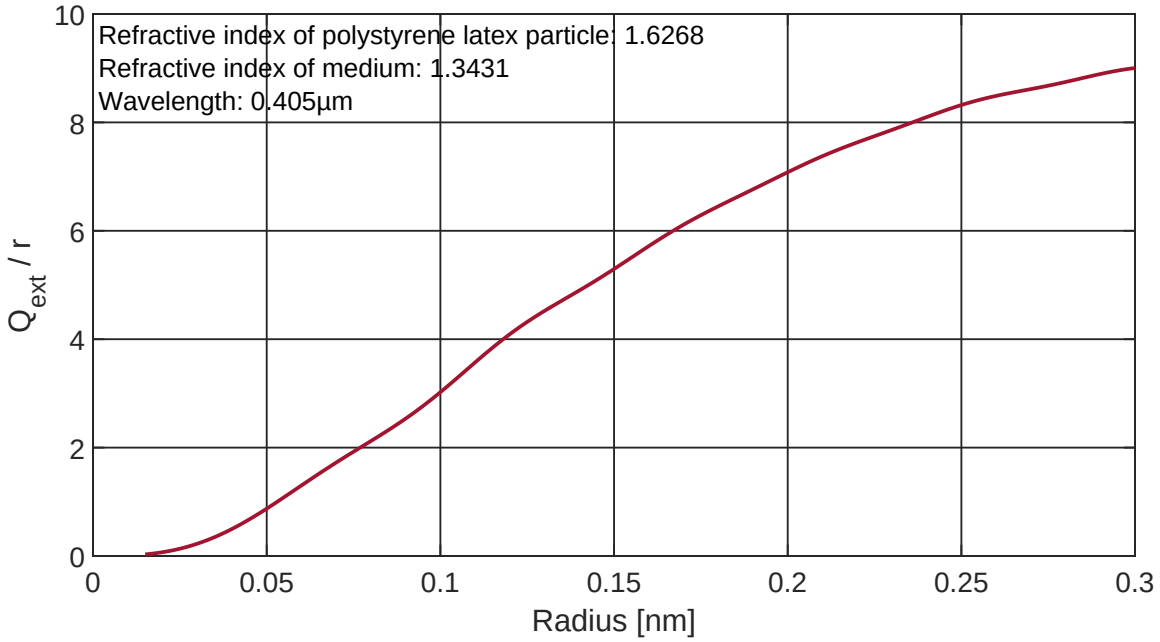

Figure 5.24: Relationship between radius of the polystyrene latex particles and the quotient of the extinction efficiency factor and the drop radius

In Fig. 5.25, two measured time-shift signals with known volume concentration of the inclusions are illustrated; the volume concentrations are 2% and 0.14% respectively. Comparing with the peak amplitude for the time-shift signal mode $p = 2.1$ from a pure drop, whose size is the same as the colloidal drop, the attenuation ratios are evaluated as 0.86 and 0.41, substituting these values in Eq. (5.22), the $\frac{Q_{ext}(r)}{r}$ value is obtained. The theoretical particle sizes are 30 nm and 200 nm respectively; the measured values are 33 nm and 214 nm.

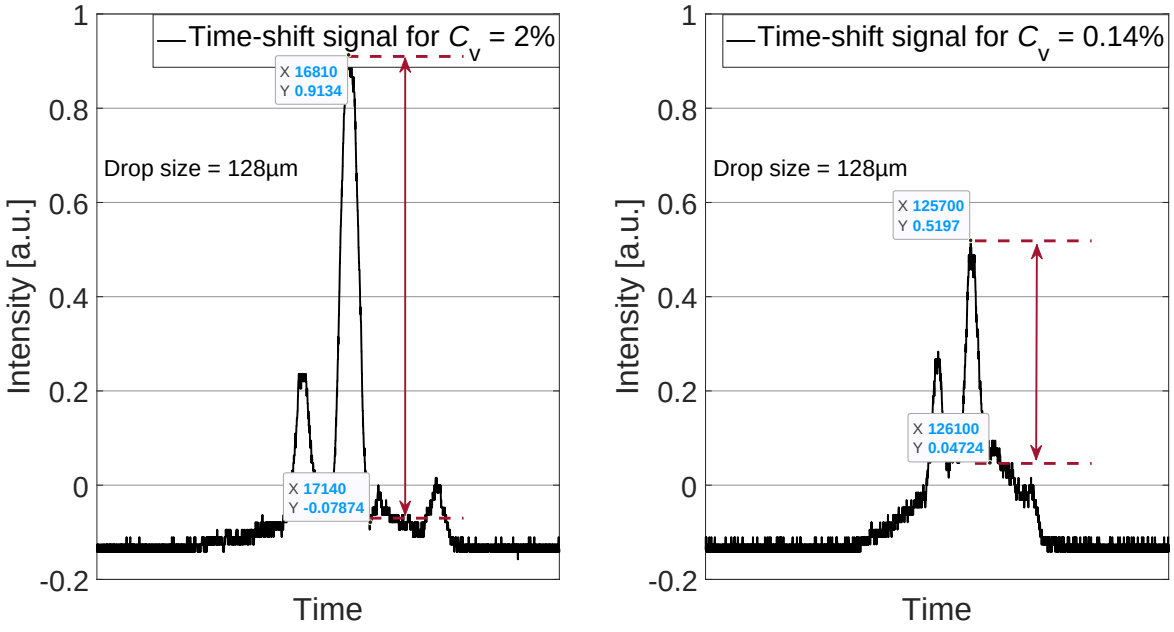

Figure 5.25: Estimation the size of the colloidal particles within the drop

Volume Fraction	Attenuation Ratio	Incident angle $\theta_{p=2.1}$	$\frac{Q_{ext}(r)}{r}$	Measured Size
0.14%	0.41	15.6°	3.41	33 nm
2%	0.86	15.6°	0.04	214 nm

Table 5.4: Estimation the size of the colloidal particle

For measurements using a light source with a single wavelength, the measurement range of the particle size is limited, because $\frac{Q_{ext}(r)}{r}$ is usually monotonic when the radius of the particle is under 400 nm; combined with other wavelengths, the measurement range could be extended. Fig. 5.26 illustrates the relationship between $\frac{Q_{ext}(r)}{r}$ and particle size for three different wavelengths.

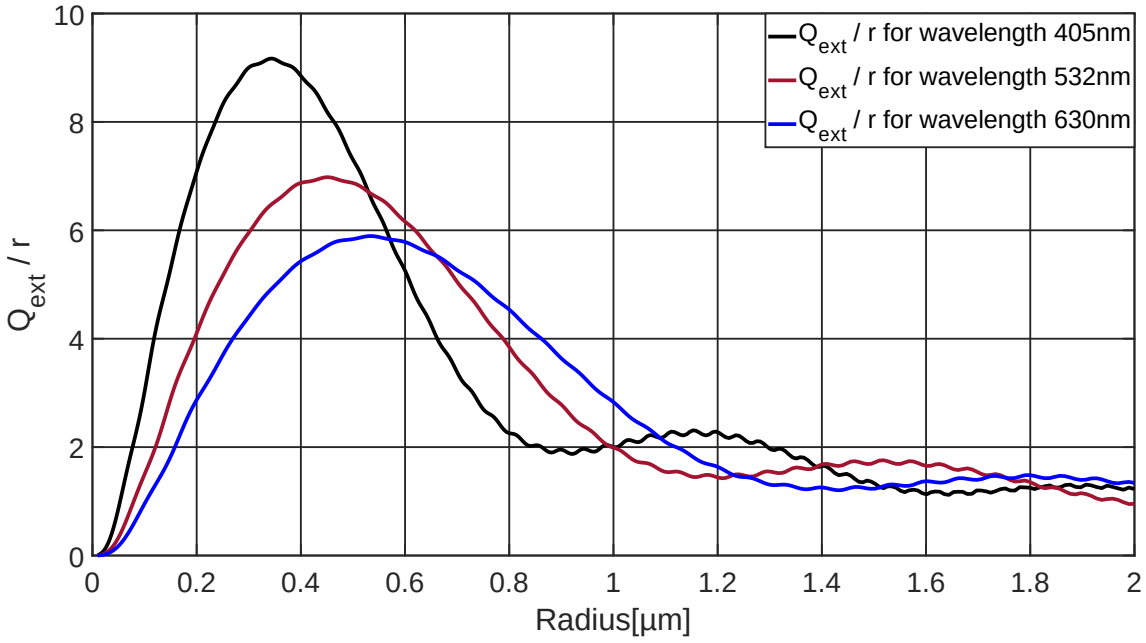

Figure 5.26: Relationship between radius of the polystyrene latex particles and the quotient of the extinction efficiency factor and the radius for different wavelengths

6 Summary and Outlook

Summary Within this study, the light scattering properties of complex particles and characterization of such particles with the time-shift technique have been investigated. In the framework of this study, the term *complex particles* refers to drops with single embedded spheres or flakes, spheroidal drops, and drops with multiple embedded inclusions. According to the shape, composition and the size parameter of the particle, corresponding simulation methods have been chosen to simulate the light scattering of these particles.

A ray-tracing code has been developed to investigate the light scattering properties of spheroidal drops by varying their aspect ratio, and drops with single embedded flakes or spheres by varying the position of the sphere and the orientation of the flake within the drop. The code has been validated through comparison with the computation results from Lorenz-Mie theory and other code for geometric optics. Subsequently, the code for the simulation of the time-shift signals from these drops has been written, which is used to simulate the time-shift signal from these drops in order to characterize them with the time-shift technique. For measuring the size of the spheroidal particle, whose aspect ratio is between 0.9 and 1.1, the systematic error achieved using the time-shift instrument should be within 15%. The simulated scattering diagrams indicate additional backscatter contributions arising from the reflection of light from the embedded particle and these contributions increase the amplitude and duration of the reflection peak in the time-shift signals for virtually all geometrical situations studied. Therefore, one can conclude that, with suitable signal detection and modifications to the signal processing, the time-shift technique should be able to unequivocally detect whether a drop contains a spherical particle or not. For detection of the embedded flake with time-shift technique, a situation of particular interest when measuring metallic paints, the answer is less conclusive.

For investigating the light scattering properties of colloidal drops, the polarized Monte Carlo ray-tracing code has been developed, which also allows the simulation of the time-shift signal acquired from a colloidal drop. The code has been validated through comparison of the simulated and measured time-shift signals from pure water drops as well as colloidal drops with embedded polystyrene latex nanoparticles. The results from simulation and experiment show that the the colloidal concentration could be estimated from the time-shift signals through evaluation of the relative scattering strength from the inclusions and through evaluation of the attenuation ratio for the signal mode $p = 2.1$, when the inclusions are spherical and their size and refractive index are known. The size of the nanoparticles could be measured with the time-shift technique as well for certain ranges of volume concentration.

Outlook For the characterization of the volume concentration of colloidal drops, the assumption is that the change of signal amplitude of the reflection peak is very limited as the volume concentration changes. However, for higher volume concentrations of colloidal particles, this assumption needs to be validated.

Using the Monte Carlo ray-tracing method the generation of a look-up table for η is still computationally intensive. For a certain size range of the inclusions and specific colloidal concentrations, an analytical or semi-analytical relationship between the parameter η for the relative scattering strength and the drop size would be desirable, thus accelerating the pre-processing effort immensely..

A more common situation in industry is that the colloidal particles within the host drop are polydisperse; therefore, it is necessary to extend the Monte Carlo ray-tracing code for a polydisperse system. For colloidal drops with high volume concentration, this will lead to a smaller optical mean free path $E(L)$. When $E(L)$ is smaller than the wavelength of the laser beam, the transport of the light within the drop can no longer be treated as independent [10]. Interference effects on the scattering phase function of the inclusions may become significant. In some cases, drops as well as the inclusions could be absorbing. Then the refractive indices for the drop and the inclusions are not real. The Monte Carlo ray-tracing code would have to be extended to accommodate imaginary refractive indices.

When a coherent laser is used as the light source for the time-shift instrument, the interference fringes should appear within the peaks of the time-shift signal, as the gray lines show in the Fig. 6.1, similar as the measured signal acquired from a colloidal drop by using the phase Doppler measurement technique [42]. These interference fringes can potentially provide more information for the signal processing to separate the signal from internal scattering of the inclusions and the scattering from the drop.

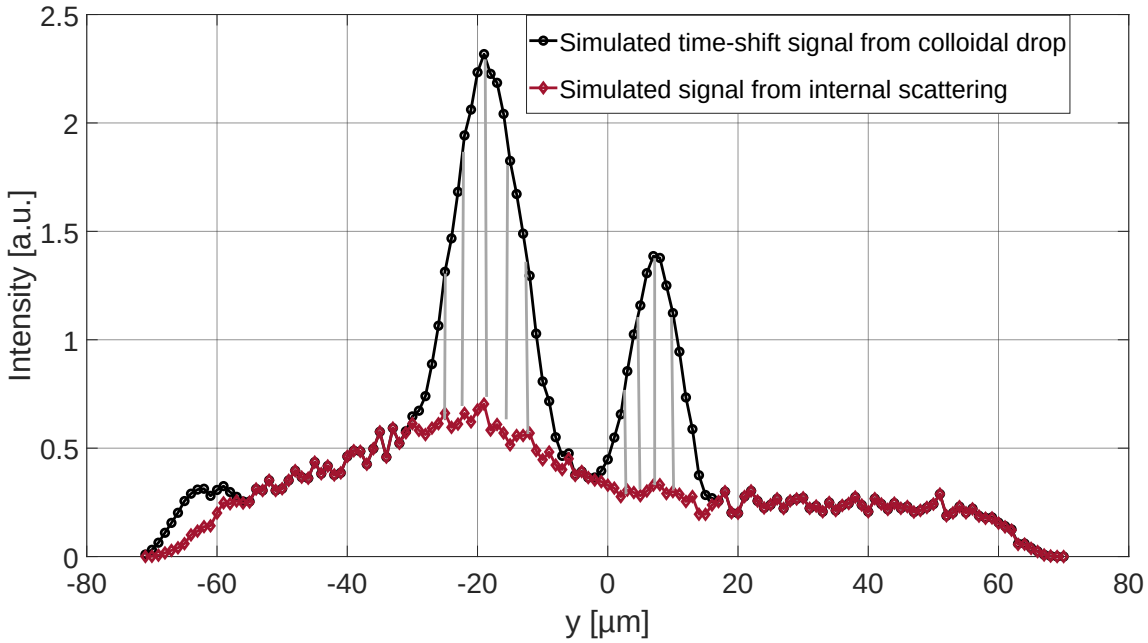

Figure 6.1: Assumption of the time-shift signal captured from a colloidal drop by using a coherent laser as light source.

The T-Matrix method provides a solution to the Maxwell's equations of scatterers and could compute the light scattering from colloidal drops. A notable advantage of the T-matrix method is that it is a complete dataset of scattering information which is only related to the size, the refractive index, and shape of the particle. For simulation of the entire time-shift signal, the Monte Carlo ray tracing method needs to be implemented multiple times. However, the T-matrix would only needs to be computed once. The scattered electric field for each time step could be obtained by only changing the incident electric field. Besides, the T-matrix method should be more accuracy than the Monte Carlo ray-tracing method. It is necessary to investigate the computation effort for computing the light scattering of colloidal drop with the T-Matrix method, when the size parameter of the drop beyond 300. If the computation effort is acceptable, the time for the pre-processing to estimate the colloidal concentration could be reduced and higher accuracy could be expected.

The Monte-Carlo ray-tracing code is currently programmed with Matlab. The parallel computation is realized by using the parallel computing tool box which requires multiple licences. To improve the computation efficiency, the code should be rewritten with another programming language for parallel computing, for instance Fortran, or C#.

Bibliography

[1] Hans-Ernst Albrecht, Nils Damaschke, Michael Borys, and Cameron Tropea. *Laser Doppler and Phase Doppler Measurement Techniques*. Springer Science & Business Media, Heidelberg, 2013.

[2] Simon L. Altmann. *Rotations, Quaternions, and double Groups*. Clarendon Press, Oxford, 1986.

[3] Shoji Asano and Giichi Yamamoto. Light scattering by a spheroidal particle. *Applied Optics*, 14(1):29–49, 1975.

[4] Rafig Azzam. Phase shifts that accompany total internal reflection at a dielectric–dielectric interface. *Journal of the Optical Society of America A*, 21(8):1559–1563, 2004.

[5] Craig F. Bohren and Donald R. Huffman. *Absorption and Scattering of Light by small Particles*. John Wiley & Sons, Weinheim, 2008.

[6] Jean-Philippe Briton, Bruno Maheu, Gérard Gréhan, and Gérard Gouesbet. Monte Carlo simulation of multiple scattering in arbitrary 3-d geometry. *Particle & Particle Systems Characterization*, 9(1-4):52–58, 1992.

[7] Nils Damaschke, Gerard Gouesbet, Gerard Gréhan, Hervé Mignon, and Cameron Tropea. Response of phase doppler anemometer systems to nonspherical droplets. *Applied Optics*, 37(10):1752–1761, 1998.

[8] Peter Josef William Debye. Der Lichtdruck auf Kugeln von beliebigem Material. *Annalen der Physik*, pages 57–136, 2014.

[9] Bruce T. Draine and Piotr J. Flatau. User guide for the discrete dipole approximation code ddscat 7.3. *arXiv preprint arXiv:1305.6497*, 2013.

[10] Hiroyuki Fujii, Leung Tsang, Jiyue Zhu, Koki Nomura, Kazumichi Kobayashi, and Masao Watanabe. Photon transport model for dense polydisperse colloidal suspensions using the radiative transfer equation combined with the dependent scattering theory. *Optics Express*, 28(15):22962–22977, 2020.

[11] Thomas A. Germer and Egon Marx. Ray model of light scattering by flake pigments or rough surfaces with smooth transparent coatings. *Applied Optics*, 43(6):1266–1274, 2004.

[12] Gérard Gouesbet. Debye series formulation for generalized Lorenz-Mie theory with the bromwich method. *Particle & Particle Systems Characterization*, 20(6):382–386, 2003.

[13] Gérard Gouesbet, Bruno Maheu, and Gérard Gréhan. Light scattering from a sphere arbitrarily located in a gaussian beam, using a bromwich formulation. *JOSA A*, 5(9):1427–1443, 1988.

[14] Eugene Hecht. *Optics*. Addison-Wesley, San Francisco, 2002.

[15] C. F. Hess and C. P. Wood. The pulse displacement technique - a single particle counter with a size range larger than 1000: 1. *Particle & Particle Systems Characterization*, 11(1):107–113, 1994.

[16] Edward A. Hovenac and James A. Lock. Assessing the contributions of surface waves and complex rays to far-field mie scattering by use of the debye series. *Journal of the Optical Society of America A*, 9(5):781–795, 1992.

[17] Yong-X. Hu, David Winker, Ping Yang, Bryan Baum, Lamont Poole, and Lelia Vann. Identification of cloud phase from PICASSO-CENA lidar depolarization: a multiple scattering sensitivity study. *Journal of Quantitative Spectroscopy and Radiative Transfer*, 70(4-6):569–579, 2001.

[18] Hendrik Christoffel Hulst and Hendrik C. van de Hulst. *Light Scattering by small Particles*. Courier Corporation, New York, 1981.

[19] Franck Jaillon and Hervé Saint-Jalmes. Description and time reduction of a Monte Carlo code to simulate propagation of polarized light through scattering media. *Applied Optics*, 42(16):3290–3296, 2003.

[20] Francis A Jenkins and Harvey E White. *Fundamentals of optics*. Tata McGraw-Hill Education, New York, 1937.

[21] B. R. Johnson. Light scattering by a multilayer sphere. *Applied Optics*, 35(18):3286–3296, 1996.

[22] Loren Jørgensen, Yoël Forterre, and Henri Lhuissier. Deformation upon impact of a concentrated suspension drop. *Journal of Fluid Mechanics*, 896:R2, 2020.

[23] F. Michael Kahnert. Numerical methods in electromagnetic scattering theory. *Journal of Quantitative Spectroscopy and Radiative Transfer*, 79:775–824, 2003.

[24] Bernard Kaplan, Guy Ledanois, and Bernard Drévillon. Mueller matrix of dense polystyrene latex sphere suspensions: measurements and Monte Carlo simulation. *Applied Optics*, 40(16):2769–2777, 2001.

[25] Philip Laven. Simulation of rainbows, coronas, and glories by use of mie theory. *Applied Optics*, 42(3):436–444, 2003.

[26] Can Li, Xue-cheng Wu, Jian-zheng Cao, Ling-hong Chen, Gerard Gréhan, and Ke-fa Cen. Application of rainbow refractometry for measurement of droplets with solid inclusions. *Optics & Laser Technology*, 98:354–362, 2018.

[27] Can Li, Yingchun Wu, Xuecheng Wu, and Cameron Tropea. Simultaneous measurement of refractive index, diameter and colloid concentration of a droplet using rainbow refractometry. *Journal of Quantitative Spectroscopy and Radiative Transfer*, 245:106834, 2020.

[28] Lingxi Li, Simon Rosenkranz, Walter Schäfer, and Cameron Tropea. Light scattering from a drop with an embedded particle and its exploitation in the time-shift technique. *Journal of Quantitative Spectroscopy and Radiative Transfer*, 227:20–31, 2019.

[29] Lingxi Li, Partrick G. Stegmann, Simon Rosenkranz, Walter Schäfer, and Cameron Tropea. Simulation of light scattering from a colloidal droplet using a polarized Monte Carlo method: application to the time-shift technique. *Optics Express*, 27(25):36388–36404, 2019.

[30] Renxian Li, Huifen Jiang, Kuan Fang Ren, et al. Debye series for light scattering by a multilayered sphere. *Applied Optics*, 45(6):1260–1270, 2006.

[31] André Liemert, Dominik Reitzle, and Alwin Kienle. Analytical solutions of the radiative transport equation for turbid and fluorescent layered media. *Scientific reports*, 7(1):1–9, 2017.

[32] S. M. Lin, D. R. Waterman, and A. H. Lettington. Measurement of droplet velocity, size and refractive index using the pulse displacement technique. *Measurement Science and Technology*, 11(6):L1–L4, 2000.

[33] James A Lock and Gérard Gouesbet. Generalized lorenz–mie theory and applications. *Journal of Quantitative Spectroscopy and Radiative Transfer*, 110(11):800–807, 2009.

[34] M. Ma, A. Chiu, G. Sahay, J. C. Doloff, N. Dholakia, R. Thakrar, J. Cohen, A. Vegas, D. Chen, K. M. Bratlie, and T. Dang. Core–shell hydrogel microcapsules for improved islets encapsulation. *Advanced Healthcare Materials*, 2(5):667–672, 2013.

[35] O. Mengual, G. Meunier, I. Cayré, K. Puech, and P. Snabre. Turbiscan ma 2000: multiple light scattering measurement for concentrated emulsion and suspension instability analysis. *Talanta*, 50(2):445–456, 1999.

[36] Gustav Mie. Beiträge zur Optik trüber Medien, speziell kolloidaler Meetallosungen. *Annalen der Physik*, 330(4):337–445, 1908.

[37] M. I. Mishchenko, L. D. Travis, and D. W. Mackowski. T-matrix method and its applications to electromagnetic scattering by particles: A current perspective. *Journal of Quantitative Spectroscopy and Radiative Transfer*, 111(11):1700–1703, 2010.

[38] Michael I. Mishchenko, Larry D. Travis, and Andrew A. Lacis. *Scattering, Absorption, and Emission of Light by Small Particles*. Cambridge University Press, Cambridge, 2006.

[39] Michael I. Mishchenko and Ping Yang. Far-field Lorenz-Mie scattering in an absorbing host medium: theoretical formalism and fortran program. *Journal of Quantitative Spectroscopy and Radiative Transfer*, 205:241–252, 2018.

[40] Timo Nousiainen, Evgenij Zubko, Jarkko V. Niemi, Kaarle Kupiainen, Martti Lehtinen, Karri Muinonen, and Gorden Videen. Single-scattering modeling of thin, birefringent mineral-dust flakes using the discrete-dipole approximation. *Journal of Geophysical Research: Atmospheres*, 114(D7), 2009.

[41] DM O'Brien. Accelerated quasi monte carlo integration of the radiative transfer equation. *Journal of Quantitative Spectroscopy and Radiative Transfer*, 48(1):41–59, 1992.

[42] Fabrice Onofri, Laurence Bergougnoux, Jean-Luc Firpo, and Jacqueline Misguich-Ripault. Size, velocity, and concentration in suspension measurements of spherical droplets and cylindrical jets. *Applied Optics*, 38(21):4681–4690, 1999.

[43] Sadegh Poozesh, Nelson Akafuah, and Kozo Saito. Effects of automotive paint spray technology on the paint transfer efficiency–a review. *Proceedings of the Institution of Mechanical Engineers, Part D: Journal of Automobile Engineering*, 232(2):282–301, 2018.

[44] Edward M. Purcell and Carlton R. Pennypacker. Scattering and absorption of light by nonspherical dielectric grains. *The Astrophysical Journal*, 186:705–714, 1973.

[45] Milun J. Raković, George W. Kattawar, Mehrűbe Mehrűbeoğlu, Brent D. Cameron, Lihong V. Wang, Sohi Rastegar, and Gerard L. Coté. Light backscattering polarization patterns from turbid media: theory and experiment. *Applied Optics*, 38(15):3399–3408, 1999.

[46] Jessica C. Ramella-Roman, Scott A. Prahl, and Steve L. Jacques. Three Monte Carlo programs of polarized light transport into scattering media: part i. *Optics Express*, 13(12):4420–4438, 2005.

[47] Load Rayleigh. The dispersal of light by a dielectric cylinder. *Philosophical Magazine*, 35:365–376, 1918.

[48] Kuan Fang Ren, Fabrice Onofri, Claude Rozé, and Thierry Girasole. Vectorial complex ray model and application to two-dimensional scattering of plane wave by a spheroidal particle. *Optics Letters*, 36(3):370–372, 2011.

[49] Simon Rosenkranz, Walter Schäfer, Cameron Tropea, and Abdelhak M. Zoubir. Modeling photon transport in turbid media for measuring colloidal concentration in drops using the time-shift technique. *Applied Optics*, 55(34):9703–9711, 2016.

[50] Walter Schäfer. Aom-systems. `https://www.aom-systems.com/de/`. Accessed: 2020-04-01.

[51] Walter Schäfer and Cameron Tropea. Time-shift technique for simultaneous measurement of size, velocity and relative refractive index of transparent droplets or particles in a flow. *Applied Optics*, 53(4):588–596, 2014.

[52] Matthias Sentis, Fabrice R. Onofri, Olivier Dhez, Jean-Yves Laurent, and Fabien Chauchard. Organic photo sensors for multi-angle light scattering characterization of particle systems. *Optics Express*, 23(21):27536–27541, 2015.

[53] Matthias Sentis, Fabrice R. Onofri, Loic Méès, and Stefan Radev. Scattering of light by large bubbles: Coupling of geometrical and physical optics approximations. *Journal of Quantitative Spectroscopy and Radiative Transfer*, 170:8–18, 2016.

[54] Jianqi Shen and Huarui Wang. Calculation of Debye series expansion of light scattering. *Applied Optics*, 49(13):2422–2428, 2010.

[55] Patrick G. Stegmann. *Laser beam interaction with spheroidal droplets: computation and measurement.* PhD thesis, tuprints, 2016.

[56] Patrick G. Stegmann, Bingqiang Sun, Jiachen Ding, Ping Yang, and Xiaodong Zhang. Study of the effects of phytoplankton morphology and vertical profile on lidar attenuated backscatter and depolarization ratio. *Journal of Quantitative Spectroscopy and Radiative Transfer*, 225:1–15, 2019.

[57] Patrick G. Stegmann, Cameron Tropea, Emma Järvinen, and Martin Schnaiter. Comparison of measured and computed phase functions of individual tropospheric ice crystals. *Journal of Quantitative Spectroscopy and Radiative Transfer*, 178:379–389, 2016.

[58] Cameron Tropea. Optical particle characterization in flows. *Annual Review of Fluid Mechanics*, 43:399–426, 2011.

[59] Manfred Wendisch and Ping Yang. *Theory of Atmospheric Radiative Transfer: A Comprehensive Introduction*, volume 1305.6497. John Wiley & Sons, Weinheim, 2013.

[60] Feng Xu, James A. Lock, and Cameron Tropea. Debye series for light scattering by a spheroid. *JOSA A*, 27(4):671–686, 2010.

[61] Feng Xu, Kuan Fang Ren, and Xiaoshu Cai. Extension of geometrical-optics approximation to on-axis gaussian beam scattering. i. by a spherical particle. *Applied optics*, 45(20):4990–4999, 2006.

[62] Feng Xu, Kuan Fang Ren, Xiaoshu Cai, and Jianqi Shen. Extension of geometrical-optics approximation to on-axis gaussian beam scattering. ii. by a spheroidal particle with end-on incidence. *Applied optics*, 45(20):5000–5009, 2006.

[63] Feng Xu, Kuanfang Ren, Gérard Gouesbet, Gérard Gréhan, and Xiaoshu Cai. Generalized Lorenz-Mie theory for an arbitrarily oriented, located, and shaped beam scattered by a homogeneous spheroid. *JOSA A*, 24(1):119–131, 2007.

[64] Min Xu. Electric field monte carlo simulation of polarized light propagation in turbid media. *Optics Express*, 12(26):6530–6539, 2004.

[65] Qingxing Xu, Qin Hao, Yin Zhenyuan, Hua Jinsong, Daniel W. Pack, and Chi-Hwa Wang. Coaxial electrohydrodynamic atomization process for production of polymeric composite microspheres. *Chemical Engineering Science*, 104:330–346, 2011.

[66] Ping Yang and K. N. Liou. Geometric-optics–integral-equation method for light scattering by nonspherical ice crystals. *Applied Optics*, 12(1):162–176, 1995.

[67] Ping Yang and K. N. Liou. Single-scattering properties of complex ice crystals in terrestrial atmosphere. *Beitrage zur Physik der Atmosphare-Contributions to Atmospheric Physics*, 71(2):223–248, 1998.

[68] Haitao Yu. *Laser beam interaction with spheroidal droplets: computation and measurement.* PhD thesis, tuprints, 2013.

[69] Haitao Yu, Jianqi Shen, and Yuehuan Wei. Geometrical optics approximation of light scattering by large air bubbles. *Particuology*, 6(5):340–346, 2008.

[70] Haitao Yu, Feng Xu, and Cameron Tropea. Simulation of optical caustics associated with the secondary rainbow of oblate droplets. *Optics Letters*, 38(21):4469–4472, 2013.

[71] Shangqin Yuan, Fei Shen, Chee Kai Chua, and Kun Zhou. Polymeric composites for powder-based additive manufacturing: Materials and applications. *Progress in Polymer Science*, 91:141–168, 2019.

[72] Maxim A. Yurkin and Alfons G. Hoekstra. The discrete dipole approximation: an overview and recent developments. *Journal of Quantitative Spectroscopy and Radiative Transfer*, 106(1-3):558–589, 2007.

[73] Maxim A. Yurkin and Alfons G. Hoekstra. The discrete-dipole-approximation code adda: Capabilities and known limitations. *Journal of Quantitative Spectroscopy and Radiative Transfer*, 112(13):2234–2247, 2011.

[74] Maxim A. Yurkin and Michael I. Mishchenko. Volume integral equation for electromagnetic scattering: Rigorous derivation and analysis for a set of multilayered particles with piecewise-smooth boundaries in a passive host medium. *Physical Review A*, 97(4):043824, 2018.

[75] Peng-Wang Zhai, George W Kattawar, and Ping Yang. Impulse response solution to the three-dimensional vector radiative transfer equation in atmosphere-ocean systems. i. monte carlo method. *Applied optics*, 47(8):1037–1047, 2008.

Nomenclature

Capital roman letters

$\mathbf{B}$	V s m^{-2}	magnetic induction vector
C_{ext}	m^2	extinction cross-section
C_v		volume concentration
$\mathbf{D}$	A s m^{-2}	dielectric displacement field
$\mathbf{D}_{RA}$		unit vector for rotation axis
D_{Drop}	m	drop diameter
D	m	host drop diameter
$\mathbf{E}$	V/m	electric field strength
$E(L)$	m	optical mean free path
$\mathbf{E}_{oi}$	V/m	incident electric field strength orthogonal to plane of incidence
$\mathbf{E}_{pi}$	V/m	incident electric field strength parallel to plane of incidence
$\mathbf{E}_{or}$	V/m	reflected electric field strength orthogonal to plane of incidence
$\mathbf{E}_{pr}$	V/m	reflected electric field strength parallel to plane of incidence
$\mathbf{E}_{ot}$	V/m	transmitted electric field strength orthogonal to plane of incidence
$\mathbf{E}_{pt}$	V/m	transmitted electric field strength parallel to plane of incidence
$\mathbf{E}_r$	V/m	reflected electric field strength
$\mathbf{E}_t$	V/m	transmitted electric field strength
$\mathbf{G}_(\mathbf{r}, \mathbf{r}')$		Green' function
$\mathbf{H}$	A/m	magnetic field vector
$\mathbf{I}$		identity dyadic
I_i	W m^{-2}	identity for incident ray
I_k	W m^{-2}	identity for individual ray
I_{sca}	W m^{-2}	identity for scattered ray
$\mathbf{J}$	A m^{-3}	Volume current density
$\mathbf{M}(\theta)$		Mueller matrix
$\mathbf{M}$		vector Function
N	m^{-3}	number density of the colloidal particles
$P_{HG}(\theta)$	m^{-3}	Henyey-Greenstein phase function
P_R	W	signal generated from reflection
P_T	W	signal generated from second order refraction
Q_{ext}		extinction coefficient
$\mathbf{R}(\phi)$	A/m	rotation matrix
R_n^{121}		coefficient for reflection of partial wave
R_n^{212}		coefficient for reflection of partial wave
$\mathbf{S}$		Stokes vector
$\mathbf{S}_i$		Stokes vector for incident ray
$\mathbf{S}_{sca}$		Stokes vector for scattered ray
T_n^{21}		coefficient for transmission of partial wave

T_n^{12}		coefficient for transmission of partial wave
$\dot{V}$	ml/min	flow rate
$\mathbf{V}$		vector to be rotated
V_D	m^3	volume of the host drop
V_P	m^3	volume of the single embedded particle
$Y(\theta, \phi)$		spherical harmonics

Lowercase roman letters

a_n		scattering coefficient
b_n		scattering coefficient
c_l		speed of light
d	m	particle size
f_G	Hz	excitation frequency of the function generator
g		asymmetry factor
m		relative refractive index
i		imaginary unit
k	1/m	wavenumber
k_0	1/m	free space wavenumber
$\mathbf{k}_i$		propagation direction
$\mathbf{n}$		normal vector at the boundary
$\mathbf{n}_D$		normal vector of detector
$\mathbf{n}_R$		vector for the propagation direction of reflected ray
$\mathbf{n}_T$		vector for the propagation direction of outgoing ray after once internal reflection
n_{eff}		effective refractive index
n_i		refractive index of incident medium
n_t		refractive index of transmitted medium
r	m	radius
$r_\parallel$		Fresnel coefficient for reflection by parallel polarization
$r_\perp$		Fresnel coefficient for reflection by perpendicular polarization
$\langle s \rangle$	m	average value of the optical mean free path
$t_\parallel$		Fresnel coefficient for transmission by parallel polarization
$t_\perp$		Fresnel coefficient for transmission by perpendicular polarization
v	m/s	velocity of the drop
x, y, z	m	model coordinates

Capital greek letters

Θ		Particular solution for angle θ
Φ		Particular solution for angle ϕ
Ψ		scalar wave function

Lowercase greek letters

α	$^\circ$	zenith angle of the orientation of the flake within drop
β	$^\circ$	azimuthal angle of the orientation of the flake within drop
$\boldsymbol{\alpha}_{ij}$		polarization tensor
θ	$^\circ$	polar deflection angle
θ_b	$^\circ$	block angle
θ_i	$^\circ$	incident angle
θ_r	$^\circ$	reflected angle

θ_t	$^\circ$	transmitted angle
θ_{rot_r}	$^\circ$	rotation angle of the reflected ray
θ_{rot_t}	$^\circ$	rotation angle of the transmitted ray
ϕ	$^\circ$	azimuthal angle
ξ		random number between 0 - 1
$\xi_n^{(1)}$		Riccati-Bessel function
$\xi_n^{(2)}$		Riccati-Bessel function
ϵ_0		vacuum permittivity
ω	Hz	angular frequency
ω_x	m	beam waist of elliptical laser beam in X axis
ω_y	m	beam waist of elliptical laser beam in Y axis
ϵ_{eff}	F/m	effective dielectric constant
ϵ_{inc}	F/m	dielectric constant of inclusion
ϵ_m	F/m	dielectric constant of medium
$\epsilon_r(\mathbf{r})$		relative permittivity
δ		Derac delta function
δ_{inc}		volume fraction of the inclusions
μ_{abs}		absorption coefficient
μ_{ext}		extinction coefficient
μ_{sca}		scattering coefficient
η		relative scattering strength
κ		inverse of the aspect ratio
λ	m	wavelength

Indices

abs	absorption
eff	effective
ext	extinction
inc	inclusion
sca	scattering

Dimensionless numbers

D_P^*	$\frac{D_{Particle}}{D_{Drop}}$	relative size of the embedded spherical particle
D_F^*	$\frac{D_{Flake}}{D_{Drop}}$	relative size of the embedded flake
ψ	$\frac{(x_0,y_0,z_0)}{D_{Drop}}$	relative position of the sphere within the drop

Abbreviations

DDA	Discrete Dipole Approximation
FDTD	Finite-Difference Time-Domain
GLMT	Generalized Lorenz–Mie Theory
GO	Geometric Optics
SLA	Institute for Fluid Mechanics and Aerodynamics at TU Darmstadt
TUD	Technische Universität Darmstadt

List of Figures

List of Tables

Publications

L. Li, S. Rosenkranz, W. Schäfer, C. Tropea, **Light scattering from a drop with an embedded particle and its exploitation in the time-shifttechnique**, *Journal of Quantitative Spectroscopy and Radiative Transfer* 227 (2019) 20–31.

L. Li, P. G. Stegmann, S. Rosenkranz, W. Schäfer, C. Tropea, **Simulation of light scattering from a colloidal droplet using a polarized MonteCarlo method: application to the time-shift technique**, *Optics Express* 27 (25) (2019) 36388–36404.

L. Li, C. Tropea, **Measurement of the colloidal particle concentration and size withina drop using the time-shift technique**, *Journal of Quantitative Spectroscopy and Radiative Transfer* ***Under review***.

L. Li, S. Rosenkranz, W. Schäfer, C. Tropea, **Sensitivity of the time-shift technique in characterizing non-spherical drops**, *19th Int Symp Appl of Laser and Imaging Techn to Fluid Mech*, Lisbon 16 - 19 July (2018).

Appendix